Silicon nanocrystals embedded in silicon alloys

van Sebille, Martijn

DOI
10.4233/uuid:2a9c61cb-897b-40f4-aa2b-fbb0173e6559

Publication date
2017

Document Version
Final published version

Citation (APA)
van Sebille, M. (2017). *Silicon nanocrystals embedded in silicon alloys*. [Dissertation (TU Delft), Delft University of Technology]. https://doi.org/10.4233/uuid:2a9c61cb-897b-40f4-aa2b-fbb0173e6559

Silicon nanocrystals embedded in silicon alloys

Proefschrift

ter verkrijging van de graad van doctor
aan de Technische Universiteit Delft,
op gezag van de Rector Magnificus prof. ir. K. C. A. M. Luyben,
voorzitter van het College voor Promoties,
in het openbaar te verdedigen op
vrijdag 3 maart 2017 om 10:00 uur

Door

Martijn van SEBILLE
Natuurkundig ingenieur
geboren te Ridderkerk, Nederland

This dissertation has been approved by the

promotors:

prof. dr. M. Zeman
dr. R. A. C. M. M. van Swaaij

Composition of the doctoral committee:

Rector Magnificus
prof. dr. M. Zeman, promotor
dr. R. A. C. M. M. van Swaaij, copromotor

Independent members:

prof. dr. L. D. A. Siebbeles, TU Delft
prof. dr. A. W. Weeber, TU Delft
dr. E. L. von Hauff, VU Amsterdam
prof. dr. J. Gómez Rivas, TU Eindhoven
prof. dr. K. Leifer, Uppsala University

We acknowledge financial support for this research from ADEM, A green Deal in Energy Materials of the Ministry of Economic Affairs of The Netherlands (www.adem-innovationlab.nl)

Published and distributed by Ipskamp Printing, the Netherlands.

ISBN: 978-94-6328-132-4

Contents

1 Introduction

1.1 General introduction

Direct conversion of light into electricity is one of the most promising approaches to provide renewable energy on a large scale. Solar-cells are devices that use the photovoltaic effect to convert sunlight into electricity.

1.2 Motivation for silicon nanocrystals

Single-junction solar-cells all suffer from spectral mismatch, reducing their cell's efficiency. Photons with lower energy than the absorber material's band gap will be transmitted and photons with higher energy than the band gap will lose the excess energy through thermalization processes as heat. The result is that only a fraction of the incident light can be converted into usable energy. This fraction is shown for a typical crystalline silicon (having a band gap of 1.12 eV) solar cell in figure 1.1. For such a solar cell this fraction is 49 % of the incident energy. Shockley and Queisser called the efficiency obtained by taking into account the spectral mismatch the *ultimate efficiency* (η_{ult}) [1]. This is valid for the assumption that each photon with energy greater than the band gap energy E_{G} generates one electronic charge at voltage of $V_{\mathrm{G}} = E_{\mathrm{G}}/q$, where q is the elementary charge. The ultimate efficiency can be expressed by

$$\eta_{\mathrm{ult}} = \frac{E_{\mathrm{G}} \int_0^{\lambda_{\mathrm{G}}} \Phi \, \mathrm{d}\lambda}{\int_0^{\infty} \frac{hc}{\lambda} \Phi \, \mathrm{d}\lambda}, \tag{1.1}$$

where λ is the wavelength, Φ is the spectral photon flux of the incident light and λ_{G} is the wavelength corresponding to the material's band gap. The ultimate efficiency is shown for varying band gaps in figure 1.2. Aside from thermalization and non-absorption, there are other loss mechanisms in solar cells, which reduce the efficiency limit calculated above. The solar cell's temperature is not absolute zero, which means that it will absorb and emit thermal radiation, exchanging radiative energy with its surroundings. Therefore recombination will occur, which reduces the open circuit voltage V_{oc} and the solar cell's efficiency. The efficiency

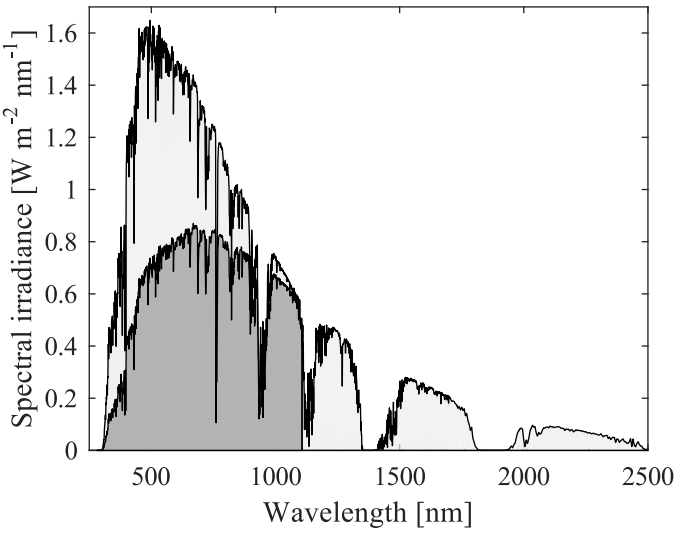

Figure 1.1: The AM1.5 spectrum and its fraction (dark shade) that can be converted into usable energy by a single-junction solar cell with a band gap of 1.12 eV.

η of a solar cell is given by

$$\eta = \frac{J_{\mathrm{ph}} V_{\mathrm{oc}} FF}{P_{\mathrm{in}}}, \tag{1.2}$$

where J_{ph} is the photocurrent density, FF is the fill factor and P_{in} is the incident power. When we again assume that each photon with energy greater than the band gap energy generates one electronic charge at voltage of $V_{\mathrm{G}} = E_{\mathrm{G}}/q$ and that the photocurrent density J_{ph} is equal to the short circuit current density, we can obtain the short circuit current density

$$J_{\mathrm{sc}} = -q \int_0^{\lambda_{\mathrm{G}}} \Phi \, \mathrm{d}\lambda. \tag{1.3}$$

Combining equations (1.1) and (1.3), we obtain

$$J_{\mathrm{sc}} = -\frac{P_{\mathrm{in}} \eta_{\mathrm{ult}}}{V_{\mathrm{G}}}. \tag{1.4}$$

The band gap utilization v is given by [1]

$$v = \frac{V_{\mathrm{oc}}}{V_{\mathrm{G}}}, \tag{1.5}$$

which is an expression for the fraction of the band gap voltage that can be used for the open circuit voltage. Combining equations (1.2), (1.4) and (1.5) results in

$$\eta = \eta_{\mathrm{ult}} v FF. \tag{1.6}$$

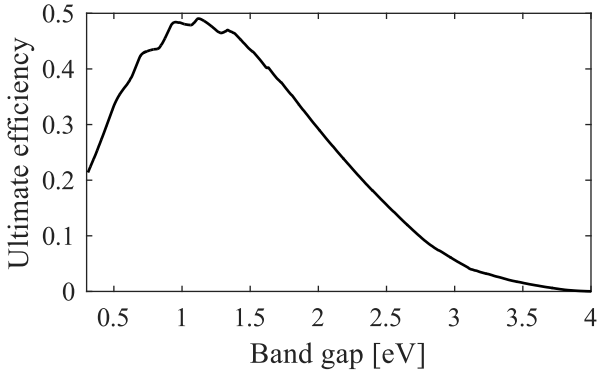

Figure 1.2: Ultimate efficiency of single-junction solar cells with varying band gap energy when illuminated with the AM1.5 spectrum.

The open circuit voltage is given by

$$V_{\mathrm{oc}} = \frac{k_{\mathrm{B}}T}{q} \ln\left[\frac{J_{\mathrm{ph}}}{J_0} + 1\right], \tag{1.7}$$

where k_{B} is the Boltzmann constant, T is the temperature and J_0 is the saturation current density. When assuming that the solar cell is in thermal equilibrium with its surroundings at $T = 300\,\mathrm{K}$ and that the solar cell absorbs and emits as a blackbody for wavelengths shorter than the band gap wavelength of its absorber material. For longer wavelengths the solar cell is assumed to be completely transparent. The blackbody radiance L^{BB} is given by [2]

$$L^{\mathrm{BB}} = \frac{2hc^2}{\lambda^5} \frac{1}{\exp\left(\frac{hc}{\lambda k_{\mathrm{B}}T}\right) - 1}, \tag{1.8}$$

which can be used to find an expression for the radiative recombination current density

$$J_0 = -2q\pi \int_0^{\lambda_{\mathrm{G}}} \frac{2hc^2}{\lambda^5} \left[\exp\left(\frac{hc}{\lambda k_{\mathrm{B}}T}\right) - 1\right]^{-1} \mathrm{d}\lambda. \tag{1.9}$$

Combining equations (1.5) and (1.7) we find

$$v = \frac{k_{\mathrm{B}}T}{E_{\mathrm{G}}} \ln\left[\frac{J_{\mathrm{ph}}}{J_0} + 1\right]. \tag{1.10}$$

The fill factor can be approximated using [3]

$$FF = \frac{v_{\mathrm{oc}} - \ln\left(v_{\mathrm{oc}} + 0.72\right)}{v_{\mathrm{oc}} + 1}, \tag{1.11}$$

where v_{oc} is the normalized open circuit voltage, which is given by

$$v_{oc} = \frac{qV_{oc}}{k_B T}. \tag{1.12}$$

Using this set of equations, first derived by Shockey and Queisser, the maximum efficiency for single-junction solar cells can be estimated [1], known as the Shockley–Queisser limit. This limit is shown in figure 1.3 for varying band gap energies, along with the losses caused by thermalization and non-absorption. The

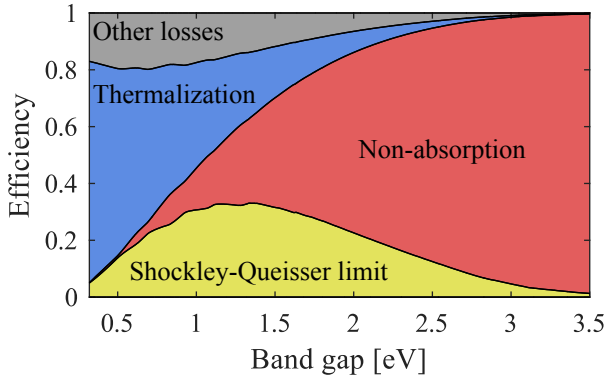

Figure 1.3: Shockley–Queisser limit and the major loss mechanisms in single-junction solar cells, calculated using the AM1.5 spectrum.

other losses include voltage loss due to thermal radiation and the fill factor being different from 100 %. Note that the Shockley–Queisser limit is only a simplified approximation of the efficiency limit. In practice more losses occur, which further reduce the maximum efficiency. These include series resistance and Auger recombination. Still, the Shockley–Queisser limit and its equations are useful as an approximation of the maximum efficieny and to estimate the effects of the losses involved. From these calculations the maximum efficiency is 33 % for an absorber material with band gap of 1.34 eV. At this band gap energy the losses caused by thermalization and non-absorption account for 23 and 30 %, respectively.

In this thesis we focus on the problem of thermalization. One solution to prevent excessive thermalization is to use multiple absorber materials with varying band gaps. Such multi-junction devices can exceed the Shockley–Queisser limit and have record efficiencies, up to 38.8 % for non-concentrator, quintuple-junction solar-cells at the time of writing [4, 5]. However, materials used to achieve the different band gaps in these devices typically include indium, gallium and arsenic, which are either scarce or toxic [6, 7].

In 2005 Green *et al.* proposed the concept of a multijunction device based entirely on silicon nanocrystals embedded in a dielectric matrix made of silicon and its compounds with oxygen, nitrogen and carbon [8]. The different band gaps

needed for efficient spectral matching would be accomplished by utilizing the size-dependent quantum confinement in nanometer-sized crystals. The quantum mechanical concepts related to these systems and their possible applications in photovoltaic solar-cells will be discussed in more detail in the section below.

1.3 Concepts for silicon nanocrystal solar-cells

Heisenberg's uncertainty principle states that it is impossible to accurately describe both a particle's position x and momentum p simultaneously. Kennard formulated this relationship as [9]

$$\sigma_x \sigma_p \geq \frac{\hbar}{2}, \tag{1.13}$$

where σ_x and σ_p are the standard deviations of position and momentum, respectively, and $\hbar$ is the reduced Planck's constant, defined as $\hbar = h/2\pi$. Since the reduced Planck's constant is very small, this relationship is only relevant for very small, sub-atomic particles, like electrons. The consequence of the uncertainty principle is that the position of small particles can only be described in terms of probability, using the non-relativistic Schrödinger's equation

$$i\hbar \frac{\partial}{\partial t} \Psi(x,t) = \left[\frac{-\hbar^2}{2\mu} \nabla^2 + V(x,t) \right] \Psi(x,t), \tag{1.14}$$

where i is the imaginary unit, Ψ is the wave function of the quantum system, dependent on position x and time t, μ is the particle's reduced mass, V is its potential energy and ∇^2 is the Laplacian. Solving this partial differential equation for different boundary conditions and potential energy provides insight into the behavior of very small particles. For the purpose of this thesis the most interesting cases are the potential well and the process of tunneling, described in more detail in the following sections.

1.3.1 Quantum confinement

Consider a one-dimensional box with width a, a potential equal to zero and infinite potential outside the box, shown in figure 1.4. Solving the Schrödinger equation for this system leads to

$$\psi(x,t) = [A \sin(kx) + B \cos(kx)] \exp(-i\omega t), \tag{1.15}$$

where A and B are arbitrary complex numbers, k is the wavenumber and ω is the angular frequency, describing the frequency of oscillations through space and time, respectively. The total energy of the particle in quantum state $n = 1, 2, 3, \ldots$ is given by

$$E_n = \frac{\hbar^2 \pi^2}{2ma^2} n^2, \tag{1.16}$$

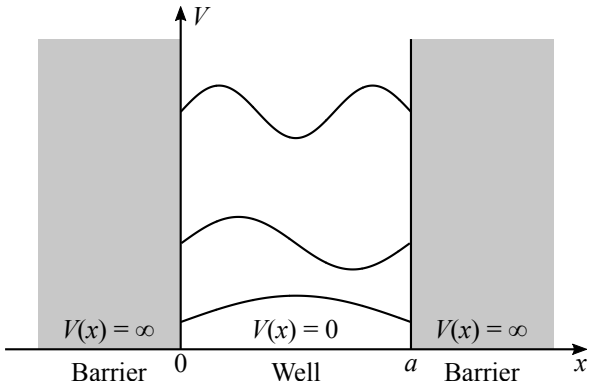

Figure 1.4: A one-dimensional box with potential equal to zero and infinite potential outside the box.

where m is the effective mass of the particle. Equation (1.16) can be modified for a three-dimensional box to accommodate the x, y and z dimensions in n and a

$$E_n = \frac{\hbar^2 \pi^2}{2m} \left[\frac{n_x^2}{a_x^2} + \frac{n_y^2}{a_y^2} + \frac{n_z^2}{a_z^2} \right]. \tag{1.17}$$

The particle in a box model can be used to describe nanoparticles in a high-band gap dielectric matrix. This is only the case when the nanoparticle radius is smaller than the exciton Bohr radius. The exciton Bohr radius is 4.3 nm for crystalline silicon [10], so quantum confinement applies to silicon nanocrystals with diameters smaller than 8.6 nm.

For nanocrystals embedded in a dielectric matrix, as studied in this thesis, the potential barrier height is not infinite, but limited by the band gap of the matrix material. Including the potential of the barrier V_0 results in the following expression for the confined energy levels [11]

$$E_n = \frac{3\hbar^2 \pi^2}{2m^* a^2} n^2 \left[1 + \frac{2\hbar}{a\sqrt{2m^* V_0}} \right]^{-2} = \frac{3\hbar^2 \pi^2}{8m^* r^2} n^2 \left[1 + \frac{\hbar}{r\sqrt{2m^* V_0}} \right]^{-2}, \tag{1.18}$$

where r is the nanoparticle radius ($a = 2r$), and m^* includes the effective mass of the electron m_e^* and hole m_h^*

$$m^* = \left[\frac{1}{m_e^*} + \frac{1}{m_h^*} \right]^{-1}. \tag{1.19}$$

Equation (1.18) shows that the confinement energy increases strongly for decreased particle sizes. Also, a lower barrier height decreases the confinement energy.

Equations (1.17) and (1.18) are valid for cubic nanocrystals, but in reality nanocrystals are approximately spherically shaped when synthesized in a multilayer structure [12]. Therefore a correction factor of $\frac{4}{3}$ is introduced [13]

$$E_n = \frac{\hbar^2\pi^2}{2m^*r^2}n^2\left[1+\frac{\hbar}{r\sqrt{2m^*V_0}}\right]^{-2}. \tag{1.20}$$

For confined structures the band gap is the sum of the material's bulk band gap and the structure's confinement

$$E_{\text{confined}} = E_{\text{bulk}} + E_n, \tag{1.21}$$

where E_{confined} and E_{bulk} are the confined and bulk band gap, respectively, and E_n is the nth energy state. The electron-hole pair is modeled as a particle in a box at ground level, so $n = 1$ [14]. Combining equations (1.20) and (1.21) results in the band gap for spherical confined nanoparticles

$$E_{\text{confined}} = E_{\text{bulk}} + \frac{\hbar^2\pi^2}{2m^*r^2}\left[1+\frac{\hbar}{r\sqrt{2m^*V_0}}\right]^{-2}. \tag{1.22}$$

These equations include effects of the nanocrystal's size, its shape, and the band gap of its surrounding matrix. It does not include other effects that can influence the nanocrystal's band gap, like stress imposed by the embedding matrix [15], and the presence and nature of nanocrystal surface passivation [16, 17]. Therefore the band gap energy of embedded silicon nanocrystals can differ from values obtained from theory. Figure 1.5 shows the theoretical band gap values for varying nanocrystal diameters and experimental data obtained using photoluminescence measurements reported by Kůsová *et al.* [15].

Because the potential barrier height is not infinite for nanocrystals in a dielectric matrix, the probability for an electron to exist outside its nanocrystal is non-zero. If two nanocrystals are closely spaced, the wavefunctions of their electrons can overlap and electrons can tunnel from one nanocrystals to the next, through the potential barrier. The probability for tunneling to occur (expressed as the transmittance, T) depends on the energy barrier height of the embedding matrix ΔE, and the inter-particle distance d, given by [21]

$$T \propto \exp\left[-\sqrt{\frac{8m^*}{\hbar^2}}\Delta E^{\frac{1}{2}}d\right]. \tag{1.23}$$

1.3.2 Phase separation and crystallization

Embedded silicon nanocrystals can be made by annealing silicon-rich silicon alloy films and is typically performed using a tube furnace or rapid thermal annealing (RTA) furnace [12]. During annealing the material undergoes several changes

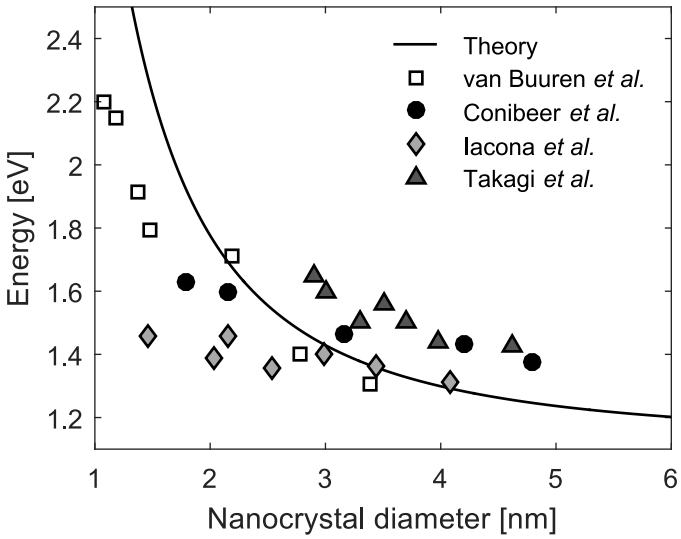

Figure 1.5: Nanocrystal band gap energy as a function of nanocrystal diameter. The markers show experimental data obtained by photoluminescence measurements from literature [11, 18–20]. The solid line shows the theoretical band gap according to equation (1.22).

at different temperatures, shown schematically in figure 1.6. Hydrogen effusion occurs between approximately 400 to 600 °C [22], creating optically active defects [23]. Between 600 to 900 °C phase separation of the excess silicon occurs, creating amorphous silicon nanoparticles, surrounded by an amorphous silicon oxide matrix. The phase separation is driven by a gain in the Gibbs free energy of the system [24]. Annealing at temperatures in excess of 900 °C leads to crystallization of these amorphous nanoparticles [25]. The crystallization kinetics typically follow a sigmoidal profile described by the Johnson-Mehl-Avrami-Kolmogorov equation [26, 27] and occurs in three stages: (i) Incubation, (ii) crystallization and grain growth, and (iii) and saturation.

1.4 Research questions

1.4.1 Inter-particle distances

Using films containing alternating layers of stoichiometric and silicon-rich silicon alloys allows for the control over the nanocrystal size, limited to the silicon-rich layer thickness [28, 29]. Various charge transport mechanisms for embedded silicon nanocrystal have been suggested, including direct tunneling [30], trap-assisted tunneling [31], and hopping [32]. No clear consensus exists concerning the exact mechanisms, especially concerning the role of defects in the matrix and

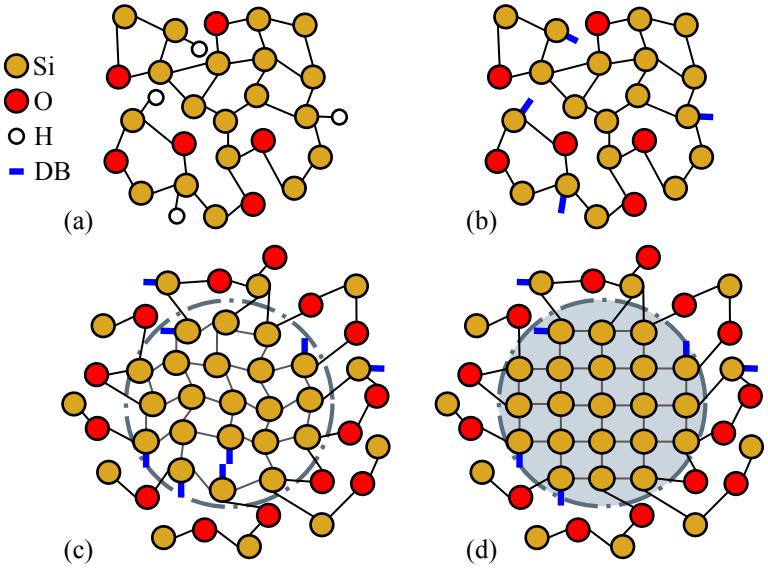

Figure 1.6: Microstructure of a a-SiO_x:H sample (a) as deposited, (b) annealed at 400 to 600 °C causing hydrogen effusion, (c) annealed at 600 to 900 °C causing phase separation of the excess silicon, (d) annealed at 900 °C and up causing crystallization of the amorphous silicon nanoparticles.

at the nanocrystal interface [31–35]. Nonetheless, the total charge transport is expected to be highly dependent on the nanocrystal spacing and the choice of dielectric material [36]. For SiO_2 films, an inter-particle spacing up to 2 nm is acceptable, which provides a minimum mobility of 10^{-1} cm^2 V^{-1} s [8].

The nanocrystal density in the silicon-rich layers can be controlled by tuning the stoichiometry of these layers during deposition. A low silicon content leads to relatively few, isolated nanocrystals and increasing the excess silicon content will eventually lead to clustering of nanocrystals, shown schematically in figure 1.7. When the nanocrystal density is too low, the probability of nearest-neighbor nanocrystal within 2 nm is too low. In contrast, when the excess silicon content is too high, nanocrystals are so closely spaced that they start clustering, which reduces the quantum confinement in these crystals. This means there is an optimal stoichiometry to achieve a limited nanocrystal spacing without clustering. What is the optimal stoichiometry and how does it depend on the crystallinity of the film and the thicknesses of the multilayer structure?

1.4.2 Size distribution

The mean and deviation of nanocrystal size are crucial parameters in determining the optical properties of the material [37, 38], and electronic transport properties

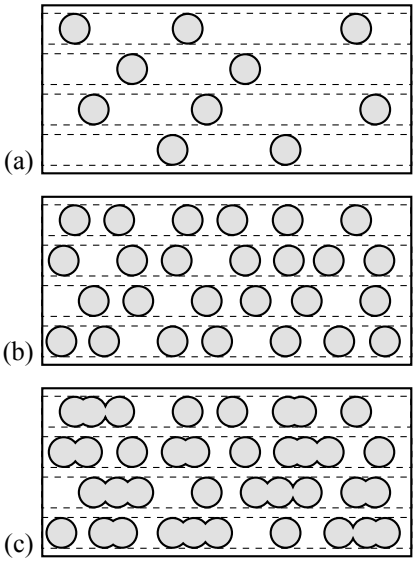

Figure 1.7: Nanocrystals formed in silicon-rich layers with relatively low (a), medium (b) and high (c) excess silicon, separated by stoichiometric buffer layers.

in photovoltaic devices [39]. Furthermore, for silicon nanocrystals with a sufficiently narrow size distribution and which are closely spaced, a miniband will form and result in an increase of the effective band gap of the superlattice material [29]. Therefore, controlling both the mean size and the size distribution of silicon nanocrystals is of great importance.

Limited by the nanometer-scale dimensions of nanocrystals, transmission electron microscopy (TEM) is the only direct measurement tool capable of capturing the size and shape of embedded nanocrystals. Although silicon nanocrystal size distributions obtained from TEM images have been reported (e.g. Ref [38, 40–42]), the method used to obtain these distributions is either unclear, performed using closed source software or without the possibility to verify which nanocrystals were measured.

When we consider nanocrystals of different materials, we find more and clearer methods are used, but all lack either in analysis speed, accuracy, or both. These analyses are typically carried out manually or by thresholding methods (e.g. Ref [43–45]). Manual measuring is very time-consuming and can be biased by subjective choices and expectations. Thresholding methods face difficulties when applied to images with background inhomogeneities. These methods typically need high quality TEM images with high signal-to-noise ratios and homogeneous backgrounds to function properly. Furthermore, poor choice of threshold settings might lead to biased results [46].

A different approach was reported by Mondini *et al.* They demonstrated a

method based on fitting each nanocrystal individually with an intensity profile [47]. This method, called PEBBLES, is not sensitive to inhomogeneous background or global contrast differences. However, with an analysis speed of 1 nanocrystal per second under favorable conditions and significantly slower speeds for sub-optimal conditions [47] analyzing several images with hundreds of nanocrystals is time-consuming. So, a quick method to measure nanocrystals in TEM images with minimal user input to minimize user bias has been lacking. How can the nanocrystal size distribution of embedded silicon nanocrystals be determined objectively and quickly?

1.4.3 Density of states

The relation between the size of nanocrystals and their optical properties is complex, since these optical properties are affected by several other factors, including high stress imposed by the embedding matrix [15], and the presence and nature of nanocrystal surface passivation [16, 17]. These effects makes a direct translation between absolute nanocrystal sizes and their optical properties very difficult, if not impossible. However, it is not the size of nanocrystals, but their optical properties and the ability to tune them that are of most interest for photovoltaic purposes.

Sain and Das showed that the optical band gap for silicon nanocrystal containing films of silicon nitride films increases for increasing nitrogen concentrations [48]. For thermally annealed Si-rich amorphous silicon carbide films, Song *et al.* showed that upon annealing the band gap increases with increasing temperature [49]. Both these findings were obtained from reflectance and transmittance measurements. Ding *et al.* performed optical measurements using photothermal deflection spectroscopy (PDS) on thermally annealed SiC, SiO_x, and SiC/SiO_x hetero-superlattices [23]. Their results showed that an increase in annealing temperature leads to a significant increase in sub-band gap absorption and a red-shift of the E_{04} gap (the photon energy at which the absorption coefficient equals $10^4\ cm^{-1}$) for SiC films. SiO_x films and SiC/SiO_x hetero-superlattices show a similar decrease of the E_{04} gap upon annealing, followed by an increase for annealing temperatures greater than the crystallization temperature [23]. However, several changes occur in the material during annealing, such as broadening of tail states and an increasing defect density caused by hydrogen effusion. Furthermore, depending on the material, a subsequent decreasing defect density at elevated annealing temperatures can occur, as annihilation of dangling bonds during thermally activated restructuring of the material takes place [50]. Therefore, a shift in the band gap cannot be solely attributed to nanocrystal absorption, since it is also affected by other changes in the material. Reducing these different contributions to the absorption spectrum to a single band gap value does not accurately reflect the material's complexity. Instead, distinguishing the contributions of the a-SiO_x matrix and the nanocrystals to the absorption spectrum provides better insight on the different processes taking place during annealing. Upon pinpointing the

nanocrystal absorption contribution, their density of states (DOS) can be reconstructed. Furthermore, such a detailed analysis allows us to study the effect the annealing conditions on the nanocrystal absorption properties and their related DOS.

A similar approach has been used to study microcrystalline silicon. Chen *et al.* demonstrated a method to model and fit the absorption coefficient based on the DOS for microcrystalline silicon samples [51]. Their method uses an effective medium approximation based on the complex refractive indices of amorphous silicon and bulk c-Si. It does not, however, allow for a change in the optical properties and DOS of nanocrystalline silicon, caused by quantum confinement. This method can therefore not be applied to nanocrystals. So, a method to obtain the nanocrystal absorption properties and their DOS from absorption spectra has been lacking. How can information about the silicon nanocrystal density of states be obtained from absorption spectra?

1.4.4 Hydrogen passivation during annealing

Since hydrogen effusion occurs at lower temperatures than phase separation and crystallization, this cannot be avoided, leading to an increased defect density. Reincorporation of hydrogen into the material is considered to be an effective method to reduce the defect density [52, 53]. One option is to use a hydrogen plasma in a post-annealing passivation step, which increases the photoluminescence intensity [54]. Another option is to expose samples to a H_2 atmosphere in a post-annealing passivation step at 400 °C [55, 56] or 500 °C [53]. Similarly, López *et al.* reported an increase in photoluminescence for samples passivated in forming gas (N_2+H_2) atmosphere at 450 °C [57]. Decreasing the defect density using post-annealing passivation requires an extra processing step, which to some extent complicates the process and increases the thermal budget, thereby potentially limiting throughput by extended processing time. Another approach is to combine annealing and hydrogen passivation in a single processing step, by annealing in a H_2 containing atmosphere. Comedi *et al.* observed a fourfold increase in photoluminescence intensity, accompanied by a change in the spectral shape, for samples annealed in Ar+H_2 atmosphere, compared to samples annealed in pure Ar [58]. Since x-ray diffraction measurements on their samples show no significant differences, they conclude the hydrogen does not affect the nanocrystal growth and the changes in photoluminescence are caused by a decrease in defect density. In contrast, Cheylan and Elliman reported no significant differences in photoluminescence intensity and position when annealing at 1100 °C in N_2+H_2 atmosphere, compared to a pure N_2 atmosphere [59]. Based on these results they conclude that annealing in a hydrogen containing atmosphere does not affect nanocrystals.

Although photoluminescence measurements provide valuable information on the mean nanocrystal size and their passivation, no detailed information on the defect density of the film can be obtained. Furthermore, the discordant results

reported in literature suggest a detailed study of the effect of hydrogen on the nanocrystal growth during annealing has been lacking. Is combining the annealing and passivation steps by annealing in a hydrogen-containing annealing atmosphere effective in reducing the defect density created during annealing? How does hydrogen affect the nanocrystal growth?

1.4.5 Research questions

The research approach described above can be condensed into the following list of research questions which will be addressed in this thesis:

1. What is the optimal SiO_x stoichiometry and how does it depend on the crystallinity of the film and the thicknesses of the multilayer structure?
2. How can the nanocrystal size distribution of embedded silicon nanocrystals be determined objectively and quickly?
3. How can information about the silicon nanocrystal density of states be obtained from absorption spectra?
4. Is combining the annealing and passivation steps by annealing in a hydrogen-containing annealing atmosphere effective in reducing the defect density created during annealing? How does hydrogen affect the nanocrystal growth?

1.5 Outline of this thesis

The experimental details for the most used techniques and setups are described in chapter 2. This includes both sample fabrication and characterization techniques. Furthermore, methods to analyze data are described in this chapter, including the method to obtain the crystallinity from Raman measurements and the far-refractive index from ellipsometry measurements.

The effects of stoichiometry, crystallinity and layer thickness on the properties of layers that contain nanocrystals are examined in chapter 3. In this chapter an analytical method is developed which can be used to optimize the stoichiometry and thickness of multilayer silicon oxide films in order to achieve the highest density of non-touching and closely spaced silicon nanocrystals after annealing. The probability of a nanocrystal nearest-neighbor distance within a limited range is calculated using the crystallinity and stoichiometry of the as-deposited film as input parameters. Multiplying this probability with the nanocrystal density results in the density of non-touching and closely spaced silicon nanocrystals. This method can be used to find the best as-deposited stoichiometry in order to achieve optimal nanocrystal density and spacing after a subsequent annealing step.

A method to quickly detect and measure the nanocrystal size distribution from transmission electron microscopy (TEM) images with minimal bias caused by

user input is developed and demonstrated in chapter 4. The method uses a combination of Laplacian of Gaussian filters and non-maximum suppression and is demonstrated on bright-field TEM images of an a-SiC:H sample containing embedded silicon nanocrystals with varying magnifications. The accuracy and speed are compared with size distributions obtained by alternative methods. Finally, the error induced by slicing nanocrystals during TEM sample preparation on the measured nanocrystal size distribution is considered analytically and an equation to correct for this effect is formulated.

In chapter 5 a non-destructive measurement and simple analysis method for obtaining the absorption coefficient of silicon nanocrystals embedded in an amorphous matrix is presented. This method enables one to pinpoint the contribution of silicon nanocrystals to the absorption spectrum of nanocrystal containing films. The density of states (DOS) of the amorphous matrix is modeled using the standard model for amorphous silicon while the nanocrystals are modeled using one Gaussian distribution for the occupied states and one for the unoccupied states. The method is used to analyze a laser annealed silicon oxide sample annealed with varying laser fluences. The results of this analysis are used to propose a model for the nanocrystal growth for these fabrication conditions.

The effects of hydrogen during annealing on the nanocrystal crystallization and passivation processes is examined in chapter 6. The use of hydrogen gas during annealing leads to a lower sub-band gap absorption, indicating passivation of defects created during annealing. Samples annealed in pure nitrogen show expected trends according to crystallization theory. Samples annealed in forming gas, however, deviate from this trend. Their crystallinity decreases for increased annealing time. Furthermore, we observe a decrease in the mean nanocrystal size and the size distribution broadens, indicating that hydrogen causes a size reduction of the silicon nanocrystals.

1.6 Contribution to the research field

This doctoral thesis contains a number of characterization methods and experimental results regarding embedded silicon nanocrystals.

We demonstrated an analytical method to optimize the composition and thickness of multilayer silicon oxide films in order to achieve the highest density of non-touching and closely spaced silicon nanocrystals after annealing. The probability of a nanocrystal nearest-neighbor distance within a limited range is calculated using the crystallinity and composition of the as-deposited film as input parameters. Multiplying this probability with the nanocrystal density results in the density of non-touching and closely spaced silicon nanocrystals. This method can be used to find the best as-deposited composition in order to achieve optimal nanocrystal density and spacing after a subsequent annealing step.

We have also developed a semi-automatic method with minimal bias caused by user input to quickly detect and measure the nanocrystal size distribution

from transmission electron microscopy images and demonstrated this method on bright-field TEM images. The accuracy and speed of this novel method was compared with conventional methods used in literature and the proposed method performed comparable or better in the image test set. Furthermore, we have developed an analytical correction for the effect of slicing nanocrystals during transmission electron microscopy sample preparation on the apparent nanocrystal size distribution. We derived an equation for the apparent nanocrystal size for a given real nanocrystal size. Assuming a certain nanocrystal distribution shape, this equation can be used to fit a real nanocrystal size distribution from a measured apparent size distribution.

Furthermore, we have developed a simple analysis method for obtaining the absorption coefficient of silicon nanocrystals embedded in an amorphous matrix. This method enables us to pinpoint the contribution of silicon nanocrystals to the absorption spectrum of nanocrystal containing films. The density of states of the amorphous matrix is modeled using the standard model for amorphous silicon while the nanocrystals are modeled using one Gaussian distribution for the occupied states and one for the unoccupied states.

Finally, we reported the effect of hydrogen on the nanocrystal crystallization process for silicon nanocrystals embedded in a silicon oxide matrix. We show that hydrogen gas during annealing leads to a lower sub-band gap absorption, indicating passivation of defects created during annealing. Samples annealed in pure nitrogen show expected trends according to crystallization theory. Samples annealed in forming gas, however, deviate from this trend. Their crystallinity decreases for increased annealing time. Furthermore, we observe a decrease in the mean nanocrystal size and the size distribution broadens, indicating that hydrogen causes a size reduction of the silicon nanocrystals.

2

Experimental details

2.1 Sample fabrication

Samples were fabricated using thin film deposition techniques and were subsequently annealed in order to obtain embedded silicon nanocrystals. All depositions and thermal annealing were performed in a cleanroom class 10000. The details of the techniques and setups used are described below.

2.1.1 Radio frequency plasma enhanced chemical vapor deposition

Radio frequency plasma enhanced chemical vapor deposition (RF-PECVD) is a process in which a plasma is used to deposit a thin film on a substrate. The substrate is placed between two perpendicular electrodes and a radio frequency (13.56 MHz) discharge between them is used to partially ionize precursor gases between the electrodes. A bias voltage between the electrodes accelerates ionized atoms or molecules towards the substrate, where they deposit a thin film.

The RF-PECVD setup (built by Elletrorava S.p.A.) used in this research is a multi chamber system consisting of a central transport chamber equipped with a robot arm. Six deposition process chambers and a load lock are connected to the transport chamber. In the process chambers, intrinsic and doped amorphous silicon, as well as silicon alloys can be deposited. The system is fully automated, so once programmed, complex multilayer structures can be deposited easily. Layers are deposited in ultra-high vacuum (10^{-9} mbar) chambers. The load lock can be pumped down from atmospheric pressure to high vacuum (10^{-6} mbar) within a few minutes. Once introduced in the cluster tool, substrates can be processed layer by layer without breaking the vacuum. Cross contamination between the different processes is prevented by using dedicated processing chambers for each type of material. The deposition conditions used for the different experiments are described in their respective chapters.

2.1.2 Tube furnace

A tube furnace is a conventional furnace that uses hot gases to heat up the sample. For the experiments described in chapter 3, a Tempress horizontal tube furnace was used, with a maximum temperature of 1000 °C, maximum ramp rate of 10 °C min^{-1}, and capable of annealing in pure nitrogen and forming gas (90 % N_2 + 10 % H_2) atmospheres at atmospheric pressure.

2.1.3 Rapid thermal annealing furnace

In contrast to the tube furnace, heating in a rapid thermal annealing furnace is not achieved by hot gas or by substrate heating, but by the absorption of light. For the experiments described in chapter 3 and 6 a Solaris 100 Rapid Thermal Processor was used, which is outfitted with thirteen quartz halogen lamps on top and bottom of the sample. This furnace has a maximum temperature of 1100 °C, a maximum ramp rate of 60 °C s^{-1}, and is capable of annealing in pure nitrogen and forming gas atmospheres at atmospheric pressure.

2.2 Sample characterization

2.2.1 X-ray photoelectron spectroscopy

X-ray photoelectron spectroscopy (XPS) is a technique that can be used to measure the elemental composition of samples. XPS measurements are obtained by irradiating a sample with a x-ray beam and measuring the number of electrons that escape from the film and their kinetic energy, shown schematically in figure 2.1. The obtained spectrum shows the number of photo-emitted electrons as

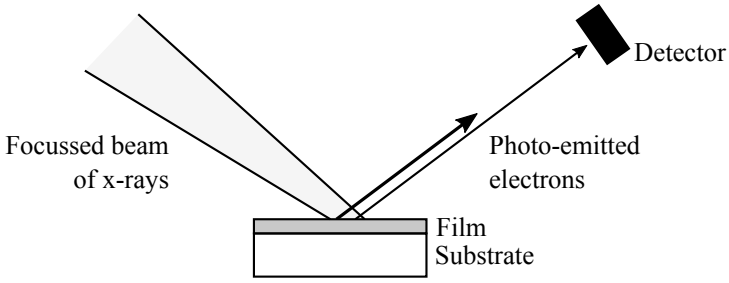

Figure 2.1: Schematic representation of an XPS setup.

a function of their binding energy. Since each element has a distinct set of spectral peaks, corresponding to its electron configuration within the atoms, the number of detected electrons in each of the peaks can be related to the amount of the element in the measured volume. In order to generate atomic percentages of the elements present, the measurement is corrected for the relative sensitivity.

XPS measurements were used to obtain the bulk stoichiometry of the deposited films. The measurements were performed using a Thermo Scientific K-Alpha setup. It is a surface-sensitive measurement, so in order to obtain bulk properties of the films examined and to remove surface contamination, the film surface was etched with an ion gun prior to measurements.

2.2.2 Spectroscopic ellipsometry

Ellipsometry is an optical measurement technique based on the change in polarization of light upon interaction with the examined sample. Light of a white light source is passed through a polarizer before interaction with the sample, as shown in figure 2.2. After interaction with the sample, the light is reflected and passes

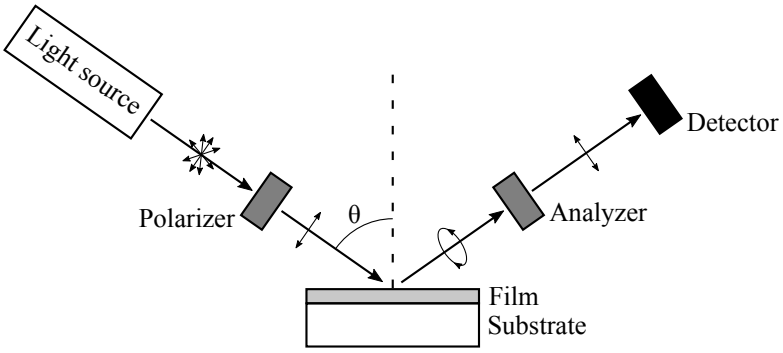

Figure 2.2: Schematic representation of a spectroscopic ellipsometry setup.

through an analyzer before entering a detector, which measures the wavelength dependent change in amplitude ratio and phase. A Cody-Lorentz model is used to fit the measured data [60]. This provides information about the film's dielectric properties, including its thickness, band gap and complex refractive index. Spectroscopic ellipsometry was also used to determine the far-infrared refractive index n_0 [61]. The far-infrared refractive index is obtained by fitting the wavelength dependent refractive index n in the range where the extinction coefficient $k = 0$ with

$$\frac{1}{n^2 - 1} = a - bE^2, \tag{2.1}$$

where E is the photon energy. The coefficients a and b are obtained from the fit and can then be used to obtain n_0 by solving equation (2.1) for $E = 0$. Figure 2.3 shows the far-refractive index for SiO_x films with varying oxygen content, obtained using equation 2.1. The far-refractive index n_0 is linearly dependent on the oxygen content in the film, according to

$$n_0 = -3\Gamma_O + 3.3, \tag{2.2}$$

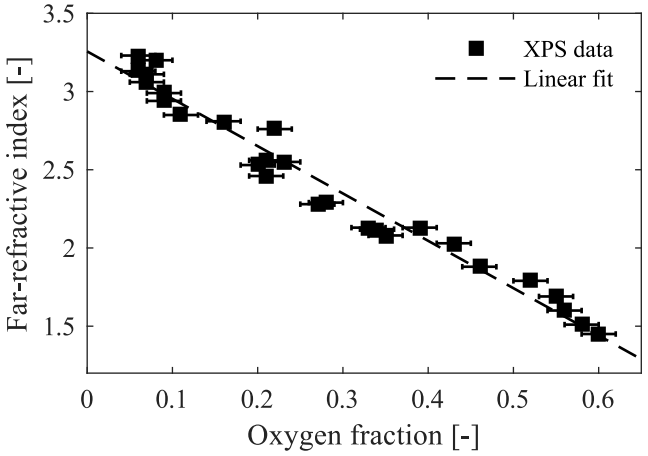

Figure 2.3: Far-refractive index as a function of the film's oxygen fraction obtained using XPS measurements. The data is fitted with a linear fit according to equation 2.2.

where Γ_O is the oxygen fraction. This relationship can be used as a quick and non-destructive alternative to XPS to obtain an indication of film's stoichiometry.

Spectroscopic ellipsometry measurements were carried out using a J.A. Woollam Co., Inc. M-2000 Spectroscopic Ellipsometer, using a wavelength range of 192 to 1690 nm.

2.2.3 Raman spectroscopy

Raman spectroscopy is a technique used to observe low-frequency modes in thin films, using inelastic scattering of monochromatic light. Upon illumination with a monochromatic light, the incident photons can interact with the atoms in the film, resulting in scattering of the incident photons, shown in figure 2.4. The dominant scattering process is Rayleigh scattering, which is an elastic form of scattering, meaning that the photon's energy is conserved and that only its direction is changed. A much less likely process is inelastic scattering, or Raman scattering, resulting in a reduction (Stokes) or increase (anti-Stokes) of the scattered photon's energy. Measuring the spectrally dependent Raman scattering intensity results in a phonon spectrum, indicating the acoustic and optical modes of the atomic lattice. A typical Raman spectrum for the systems used in this thesis is shown in figure 2.5. In this figure the phonon modes of a-Si at 170, 360, 445 and 495 cm^{-1} can be observed, as well as the c-Si TO mode at 517 cm^{-1}. The crystallinity X_C is the ratio of Si–Si bonds in crystalline phase over the Si–Si bonds in amorphous and crystalline phase [62] and can be calculated as follows

$$X_C = \frac{I_{\text{TO,c-Si}}}{\sigma I_{\text{TO,a-Si}} + I_{\text{TO,c-Si}}}, \tag{2.3}$$

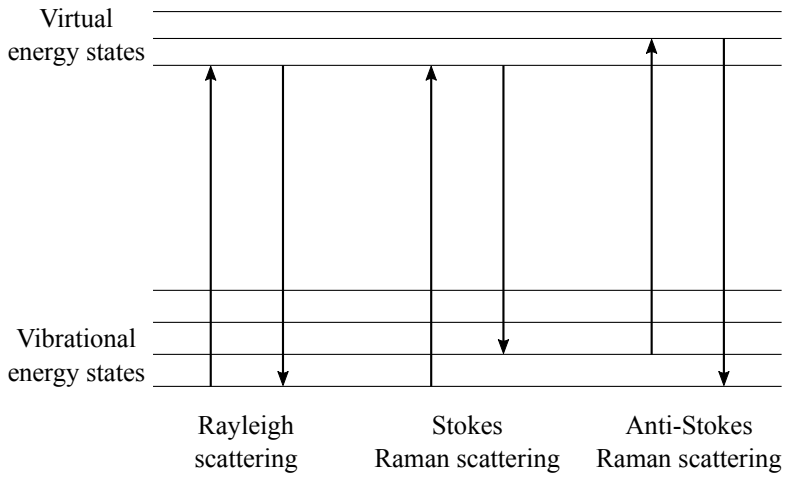

Figure 2.4: Energy-level diagram showing the states involved in Raman scattering.

where $I_{\text{TO,c-Si}}$ and $I_{\text{TO,a-Si}}$ are the integrated transverse optical (TO) phonon modes of crystalline and amorphous silicon, respectively. σ is a factor to correct for the difference in scattering cross section between these modes and is set to 0.8 [62].

The crystallinity of silicon oxide films annealed at a certain temperature depends on the stoichiometry of the as-deposited film. The effect of stoichiometry on intrinsic, and p- and n-type doped SiO_x samples annealed at 1000 °C is shown in figure 2.6. For low stoichiometry the film reaches a high crystallinity for the annealing conditions used and decreases with increasing stoichiometry. Furthermore, increased p-type doping concentration leads to an increase in crystallinity for similar stoichiometries, while increased n-type doping concentration leads to a slight decrease in crystallinity. For stoichiometries greater than approximately $SiO_{1.2}$ no crystallization occurs. This makes silicon oxide with such a stoichiometry suitable as buffer layers in a multilayer structure. A buffer layer stoichiometry of $SiO_{1.3}$ was used in chapters 3 and 6. We stress that the crystallinity achieved for varying stoichiometry depends greatly on the deposition technique and the annealing conditions used [63].

Raman spectra were measured using a Renishaw InVia setup in backscattering geometry, with a 25 mW Ar laser as excitation source with a wavelength of 514 nm and focused on a spot of approximately 1 µm.

2.2.4 Photothermal deflection spectroscopy

Photothermal deflection spectroscopy (PDS) is an optical absorption measurement technique based on the thermal relaxation of excited carriers. A schematic representation of the PDS setup used in shown in figure 2.7. Light of a white light source is passed through a monochromator and a chopper before illuminat-

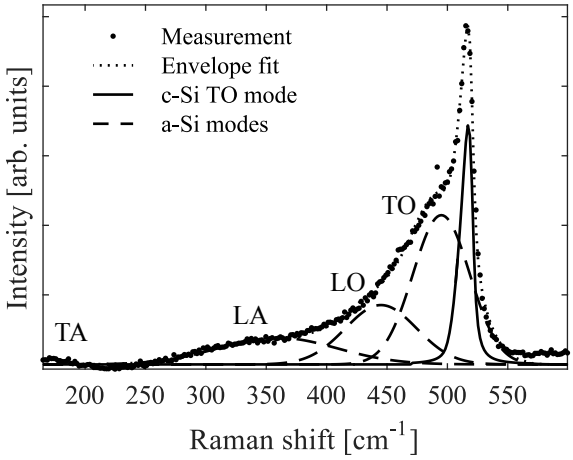

Figure 2.5: A typical Raman spectrum for a sample containing silicon nanocrystals embedded in silicon oxide. The dots, the dotted line and the solid line shown the measurement data, the envelope fit and the crystalline silicon TO mode, respectively. The dashed lines show the labeled amorphous silicon modes. The crystallinity of this sample is 0.33.

ing a sample, which is submerged in non-toxic liquid perfluorohexane Fluorinert FC-72. Simultaneously, a laser, aligned parallel to the sample, skims the sample surface. Upon absorption of the chopped monochromatic light, electrons are excited and subsequently thermalize, heating the liquid in which the sample is immersed. The liquid's refractive index is highly sensitive to temperature change, so upon heating, the laser light is deflected, which is measured by two photodiodes. This deflection can be used to determine the absorption coefficient of the film [64]. The absolute PDS setup is capable of providing a dynamic detection range in the optical absorptance up to 4 orders of magnitude [65] and measures transmittance (T), reflectance (R) and absorptance (A) spectra on the same spot simultaneously, allowing for the correction of interference fringes [65]. The T, R and A spectra are calibrated with a cuvette with FC-72, a sapphire sample, and carbon nanotubes, respectively.

2.2.5 Transmission electron microscopy

Transmission electron microscopy (TEM) is a microscopy technique in which an electron beam is passed through a thin sample. The sample interacts with the electron beam and the transmitted electrons are detected on a CCD camera, forming an image. Different TEM setups were used for the experiments shown in this thesis. Their details are described in their respective chapters.

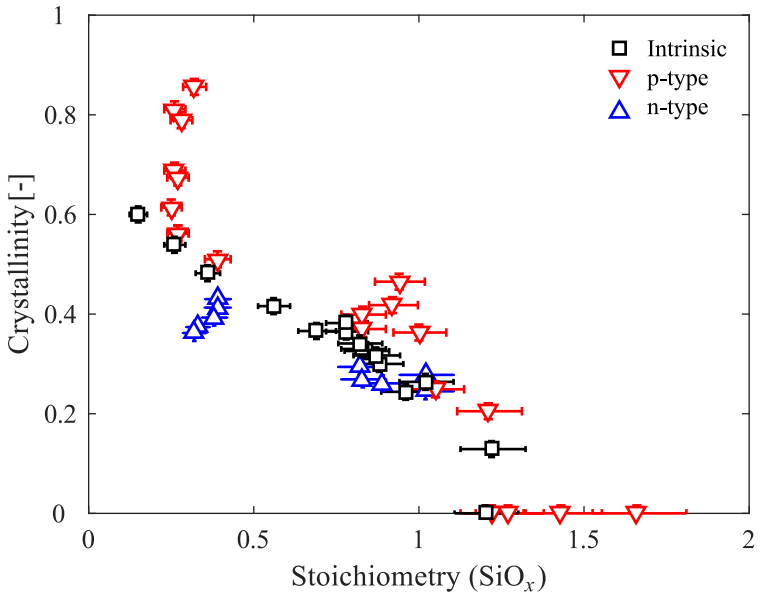

Figure 2.6: Crystallinity of monolayer silicon oxide films annealed at 1000 °C in a tube furnace of RTP as a function of their stoichiometry. The stoichiometry reported here is obtained from ellipsometry measurements using equation 2.2. The variations in crystallinity for the doped films around $x = 0.3$ and $x = 0.9$ are caused by differences in doping concentrations.

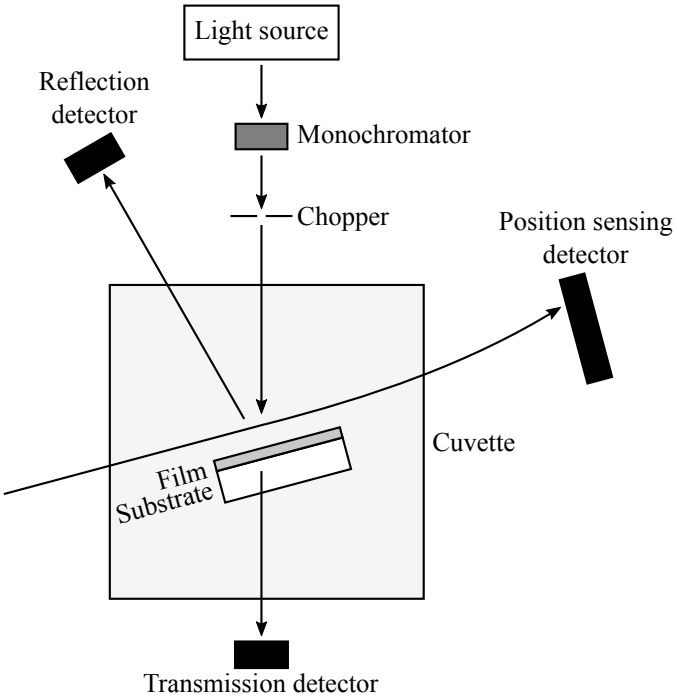

Figure 2.7: Schematic representation of the absolute PDS setup.

3

Optimizing silicon oxide embedded silicon nanocrystal inter-particle distances

This chapter is based on the following publication:

M. van Sebille, J. Allebrandi, J. Quik, R. A. C. M. M. van Swaaij, F. D. Tichelaar and M. Zeman, *Optimizing silicon oxide embedded silicon nanocrystal inter-particle distances*, Nanoscale Research Letters **11**, 355 (2016).

Abstract

We demonstrate an analytical method to optimize the stoichiometry and thickness of multilayer silicon oxide films in order to achieve the highest density of non-touching and closely spaced silicon nanocrystals after annealing. The probability of a nanocrystal nearest-neighbor distance within a limited range is calculated using the stoichiometry of the as-deposited film and the crystallinity of the annealed film as input parameters. Multiplying this probability with the nanocrystal density results in the density of non-touching and closely spaced silicon nanocrystals. This method can be used to estimate the best as-deposited stoichiometry in order to achieve optimal nanocrystal density and spacing after a subsequent annealing step.

3.1 Introduction

Using films containing alternating layers of stoichiometric and silicon-rich silicon alloys allows for the control over the nanocrystal size, limited by the silicon-rich layer thickness [28, 29]. Under certain conditions charge transport between nanocrystals is possible. Various charge transport mechanisms for embedded silicon nanocrystal have been suggested, including direct tunneling [30], trap-assisted tunneling [31], and hopping [32]. No clear consensus exists concerning the exact mechanisms, especially concerning the role of defects in the matrix and at the nanocrystal interface [31–35]. Nonetheless, the total charge transport is expected to be highly dependent on the nanocrystal spacing and the choice of dielectric material [36]. For SiO_2 films, inter-particle spacing up to 2 nm is acceptable, which provides a minimum mobility of $10^{-1}\,cm^2\,V^{-1}\,s$, as calculated by Green *et al.* [8].

The nanocrystal density in the silicon-rich layers can be controlled by tuning the composition of these layers during deposition. A low silicon content leads to relatively few isolated nanocrystals, and increasing the excess silicon content will eventually lead to clustering of nanocrystals, shown schematically in figure 3.1. When the nanocrystal density is too low, the probability of nearest-

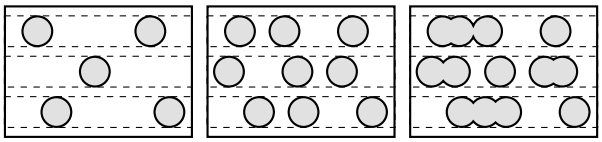

Figure 3.1: Nanocrystals formed in silicon-rich layers with relatively low (a), medium (b) and high (c) excess silicon, separated by stoichiometric buffer layers.

neighbor nanocrystal within 2 nm is too low. In contrast, when the excess silicon content is too high, nanocrystals are so closely spaced that they start clustering, which reduces the quantum confinement in these crystals. This means there is an optimal composition to achieve a limited nanocrystals spacing, while limiting clustering. In this chapter we demonstrate an analytical method to optimize the composition and thickness of multilayer silicon oxide films in order to achieve the highest density of non-touching and closely spaced silicon nanocrystals after annealing.

3.2 Experimental details

We deposited approximately 100 nm thick a-SiO_x:H films on Spectrosil 2000 quartz substrates in a radio frequency plasma-enhanced chemical vapor deposition (PECVD) reactor, described in section 2.1.1. The following deposition parameters were

used: a power density of $2.1 \times 10^{-2}\,\mathrm{W\,cm^{-2}}$, a deposition pressure of 1.4 mbar and a substrate temperature of 95 °C. The film composition was varied by changing the SiH_4 over CO_2 flow ratio from 0.07 to 0.37. A H_2 flow rate of 200 sccm was used for all depositions. N- and p-type films were fabricated by including PH_3 and B_2H_6 flows, respectively. The dopant over SiH_4 flow rate ratio was 2.0×10^{-3}. The atomic compositions of the silicon-rich and buffer layers were determined using x-ray photoelectron spectroscopy measurements, using a Thermo Scientific K-Alpha setup, described in section 2.2.1. The film surface was etched with an ion gun prior to measurements to remove surface contamination. Annealing was carried out using a Tempress horizontal tube stack (described in section 2.1.2) or a Solaris 100 RTA furnace (described in section 2.1.3) for 1 h and 3 min, respectively. All samples were annealed at 1000 °C, at atmospheric pressure and in pure nitrogen gas. The composition of the buffer layer used in these experiments is $SiO_{1.3}$. Measurements show that this stoichiometry is sufficiently high to prevent crystallization for the annealing conditions used, shown in figure 2.6. Raman spectra were measured to determine the crystallinity, using a Renishaw InVia setup in backscattering geometry. The setup and method used and to obtain the crystallinity is described in detail in section 2.2.3. Imaging the silicon crystals in the amorphous silicon layer was done using a FEI Tecnai F20ST/STEM Transmission Electron Microscope (TEM) operated at 200 kV. Thin samples for TEM were prepared in cross-section following a standard procedure after gluing the two samples together face to face: a 500 µm thick lamellae was cut out using a diamond saw, subsequently thinned to approximately 15 µm thickness by mechanical polishing, glued on a copper support ring and argon ion milled to electron transparency. The silicon nanocrystals were marked using the free hand selection tool in ImageJ [66]. The surface area was then determined and an effective diameter was recorded.

3.3 Results and Discussion

Figure 3.2 illustrates nanocrystals with radius r in a multilayer structure, including their parameters needed to determine the inter-particle distance d. We assume that the mean nanocrystal diameter equals the silicon-rich layer thickness. In order to validate this assumption, a multilayer sample with silicon-rich and buffer layer thicknesses of 3 and 1 nm has been measured with high-resolution TEM, shown in figure 3.3a. The histogram of the obtained nanocrystal diameters is shown in figure 3.3b. The mean nanocrystal diameter obtained from TEM is 2.4 nm. Figure 3.4 shows the mean nanocrystal diameter as a function of its silicon-rich layer thickness of this sample, as well as data obtained by Gutsch *et al.* [67]. For thin silicon-rich layer thicknesses the deviation between the mean nanocrystal diameter and the sample's silicon-rich layer thickness is reasonable. For thicker layers, the deviation increases. However, we should note that instead of being interested in nanocrystal diameters, we are interested in the volume

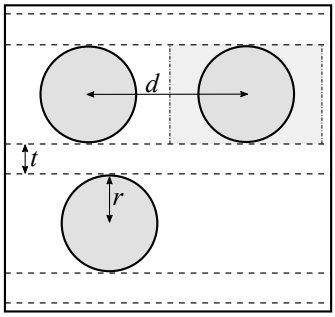

Figure 3.2: Nanocrystals in a multilayer structure shown schematically, including the nanocrystal radius r, buffer layer thickness t and inter-particle distance d. The enclosing box around a nanocrystal is shown for the right-hand nanocrystal.

these nanocrystals occupy, since that allows us to predict the nanocrystal density and their inter-particle distance for varying stoichiometry and crystallinity. The size distribution of such multilayer samples is log-normally shaped, as was observed by Gutsch *et al.* [67] and can be seen from figure 3.3b. Since the volume of the nanoparticles depends on the third power of their radius, the larger nanocrystals have a greater contribution to the mean volume $\bar{V}$. This is given by

$$\bar{V} = \frac{\sum \frac{4}{3}\pi r^3}{n_{\mathrm{NC}}}, \tag{3.1}$$

where r and n_{NC} are the nanocrystal radius and the number of nanocrystals obtained from TEM, respectively. The equivalent diameter of the mean nanocrystal $\bar{D}_{\mathrm{equiv}}$ can be expressed by

$$\bar{D}_{\mathrm{equiv}} = 2\sqrt[3]{\frac{\bar{V}}{\frac{4}{3}\pi}}. \tag{3.2}$$

Combining equations (3.1) and (3.2) results in

$$\bar{D}_{\mathrm{equiv}} = 2\sqrt[3]{\langle r^3 \rangle}, \tag{3.3}$$

where $\langle r^3 \rangle$ represents the mean value of r^3. The equivalent diameter of the sample shown in figure 3.3 is 2.6 nm and is shown in figure 3.4 along with the equivalent diameters of the data obtained by Gutsch *et al.* [67]. Because of the asymmetrical, log-normally shaped nanocrystal size distributions, all equivalent diameters are greater than their corresponding mean diameters. In general the equivalent diameters are very close to the assumed equality between the nanocrystal diameter and the silicon-rich layer thickness. This result implies that our assumption is reasonable, at least up to silicon-rich layer thicknesses up to 4.5 nm. Fortunately this range is most interesting for photovoltaic purposes because of their increased confinement.

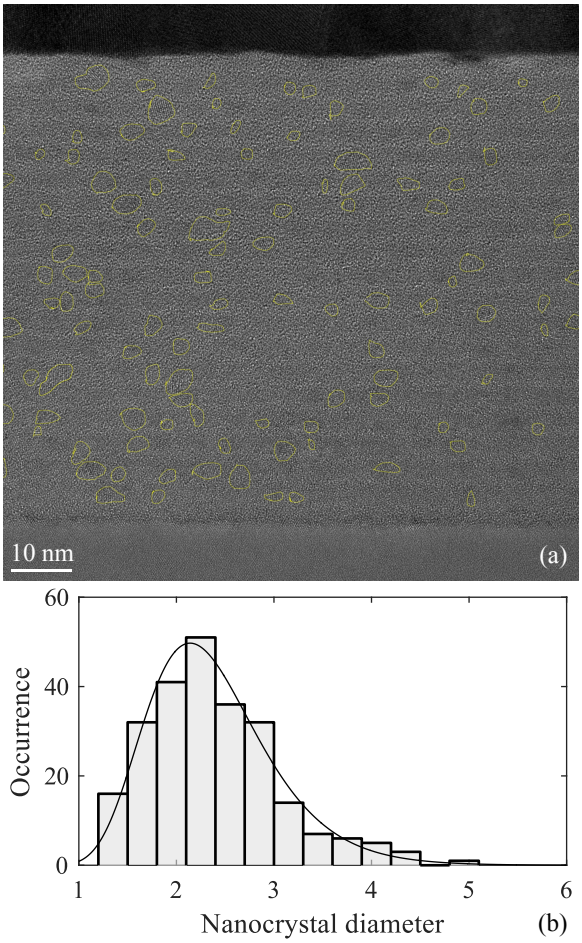

Figure 3.3: (a) Cross-sectional high-resolution TEM image of an annealed multilayer sample with silicon-rich and buffer layer thicknesses of 3 and 1 nm and (b) the histogram of the sample's nanocrystal diameters. Approximately 250 nanocrystals were measured. The histogram is fitted with a lognormal probability density function with $\mu = 0.83$ nm and $\sigma = 0.27$ nm.

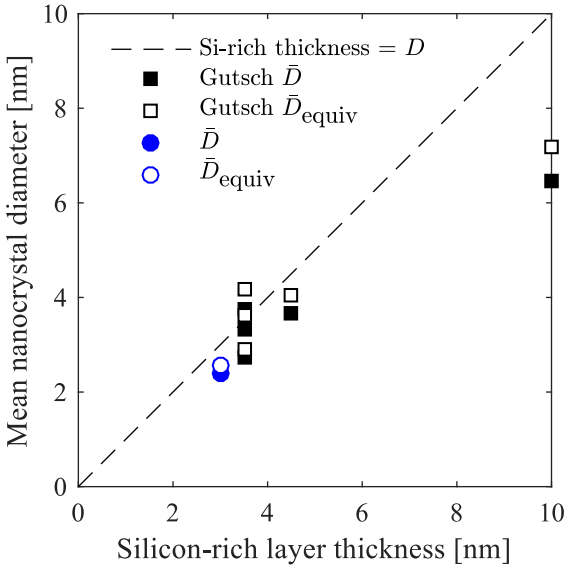

Figure 3.4: The mean nanocrystal diameter $\bar{D}$ (solid symbols) and the mean equivalent diameter $\bar{D}_{equiv}$ (open symbols) for samples with varying silicon-rich layer thicknesses. The black data points are obtained from Gutsch *et al.* [67]. The dashed line represents the equality between the nanocrystal diameter and the silicon-rich layer thickness.

Note that we do not include a core/shell structure in this approach. An amorphous sub-oxide shell is likely to form around silicon nanocrystals [28, 68]. Iacona *et al.* measured a shell to be approximately 1 nm thick [69]. This thickness corresponds with theoretical calculations and experimental measurements by Daldosso *et al.* [70]. However, Queeney *et al.* determined the shell thickness to be less than 6 Å [71]. Zimina *et al.* measured shell thicknesses of 2 to 5 Å and suggested a dependence on nanocrystal size [72]. These disagreeing results complicate the incorporation of a core/shell structure in our method. Since the aim of this chapter is to provide a simple method to predict the inter-nanocrystal distance, we do not include the core/shell structure.

In order to optimize the density of non-touching and closely spaced silicon nanocrystals, the nanocrystal density in the silicon-rich layers should be determined first. This depends on the excess silicon in these layers and can be calculated from its composition as follows

$$\mathrm{SiO}_x \longrightarrow \tfrac{x}{2}\,\mathrm{SiO}_2 + (1\text{-}\tfrac{x}{2})\mathrm{Si}. \tag{3.4}$$

The excess silicon can be in amorphous or crystalline phase, so the total atomic density in the layer ρ_{layer} is given by

$$\rho_{\text{layer}} = \Gamma_{\text{c-Si}}\rho_{\text{c-Si}} + \Gamma_{\text{a-Si}}\rho_{\text{a-Si}} + \Gamma_{\text{SiO}_2}\rho_{\text{SiO}_2}, \tag{3.5}$$

where $\rho_{\text{c-Si}}$ and $\rho_{\text{a-Si}}$ are the atomic densities of c-Si and a-Si, respectively, ρ_{SiO_2} is the molecular density of SiO_2, and $\Gamma_{\text{c-Si}}$, $\Gamma_{\text{a-Si}}$ and Γ_{SiO_2} are their respective atomic and molecular percentages. Using the definition of crystallinity and Eq. (3.4), the atomic percentages of c-Si, a-Si and SiO_2 can be written as

$$\Gamma_{\text{c-Si}} = X_{\text{C}}\left(1 - \tfrac{x}{2}\right)\cdot 100\% \tag{3.6}$$

$$\Gamma_{\text{a-Si}} = (1 - X_{\text{C}})\left(1 - \tfrac{x}{2}\right)\cdot 100\% \tag{3.7}$$

$$\Gamma_{\text{SiO}_2} = \tfrac{x}{2}\cdot 100\% \tag{3.8}$$

The atomic density of c-Si in the layer can then be determined by

$$\rho_{\text{c-Si,layer}} = \Gamma_{\text{c-Si}}\rho_{\text{layer}}. \tag{3.9}$$

The number of atoms in a nanocrystal is $N_{\text{NC}} = \frac{4}{3}\pi r^3\rho_{\text{c-Si}}$, which can be used to calculate the 2D nanocrystal density n_{2D} in a silicon-rich layer with thickness $2r$

$$n_{\text{2D}} = \frac{\rho_{\text{c-Si,layer}}}{N_{\text{NC}}}2r. \tag{3.10}$$

Figure 3.5a shows the 2D nanocrystal density for a sample with silicon-rich and buffer layer thicknesses of 3 and 1 nm, respectively, using $\rho_{\text{c-Si}}$, $\rho_{\text{a-Si}}$ and ρ_{SiO_2} 5.0×10^{28}, 5.0×10^{28} and $2.2\times10^{28}\,\mathrm{m}^{-3}$, respectively [73–76]. The 2D nanocrystal density is highest for silicon-rich layers with high crystallinity and low stoichiometry. However, in that case the nanocrystal density can be so high that crystals cluster together as illustrated in figure 3.1c. To find the fraction of nanocrystals that are properly spaced, we use the probability density function $\mathcal{F}$ of finding

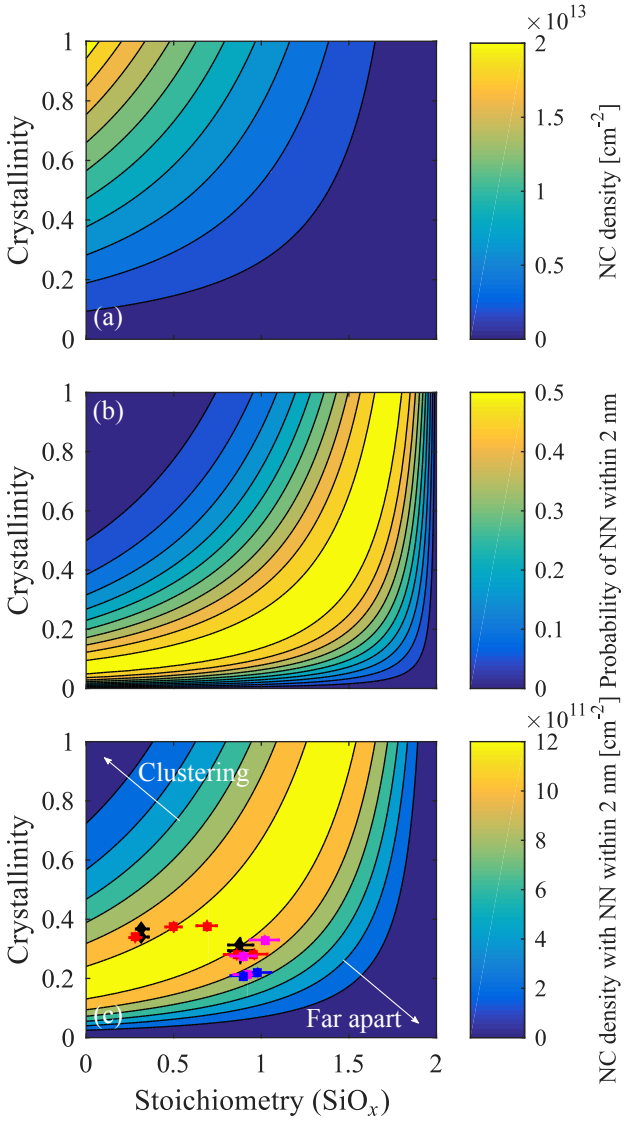

Figure 3.5: The 2D nanocrystal (NC) density (a), the probability of finding a nearest-neighbor (NN) within 2 nm (b) and the density of nanocrystals with a NN within 2 nm (c) as a function of the silicon-rich layer composition and crystallinity for a sample with silicon-rich and buffer layer thicknesses of 3 and 1 nm, respectively. The black diamonds represent tube furnace annealed intrinsic samples. The red, magenta and blue squares show intrinsic, p-type and n-type samples annealed using RTA.

a nearest-neighbor at distance d for a nanocrystal in a multilayer sample. For randomly distributed point particles this is given by [77]

$$\mathcal{F}(d) = (4j+2)\, n_{2D}\pi d \exp\left[-(2j+1)\, n_{2D}\pi d^2\right] \times \exp\left[\frac{n_{2D}\pi t^2 j\,(j+1)\,(2j+1)}{3}\right], \tag{3.11}$$

where t is the buffer layer thickness and $j = \lfloor r/t \rfloor$. Note that this probability density function describes center-to-center distances. Integrating this equation from $2r$ to $2r+2$ nm provides the edge-to-edge probability of finding a nearest-neighbor within 2 nm for a multilayer structure with silicon-rich layer thickness of 3 nm. This is shown in figure 3.5b and confirms that the optimal probability of finding the nearest-neighbor between 0 to 2 nm is very low in the range where the 2D nanocrystal density is highest, caused by clustering of the nanocrystals. We can find an optimum stoichiometry for a given crystallinity using the result shown in figure 3.5b, but aside from proper spacing of nanocrystals, we are also interested in a high nanocrystal density. Integrating Eq. (3.11) and multiplying with the 2D nanocrystal density provides the non-touching nanocrystal density with a nearest neighbor within d

$$n_{NN}(d) = n_{2D} \int_{2r}^{2r+d} \mathcal{F}(d)\, \mathrm{d}d. \tag{3.12}$$

The nanocrystal density with a nearest neighbor within 2 nm for a sample with silicon-rich layer thickness of 3 nm is shown in figure 3.5c. The highest non-touching nanocrystal density for this structure can be achieved by tuning the silicon-rich layer's composition from pure Si to approximately $SiO_{1.5}$, with crystallinity values of 0.15 to 1 , respectively. A too high crystallinity for layers with relatively low stoichiometry will lead to clustering, while too low crystallinity in layers with high stoichiometry will result in separated, but too isolated nanocrystals.

We deposited multilayer films with silicon-rich layer and buffer layer thicknesses of 3 and 1 nm and varied the silicon-rich layer's compositions and doping. The films were annealed in a tube furnace or rapid thermal annealing furnace. The crystallinity of these films after annealing are shown in figure 3.5.[‡] The crystallinity in our films does not exceed 0.4. We expect that this is caused by incomplete phase separation prior to crystallization, as observed before for silicon oxide films deposited using PECVD [63]. This means that only part of all excess silicon (see Eq. (3.4)) clusters into silicon nanoparticles, which can subsequently crystallize. The rest of the excess silicon remains in the surrounding matrix, which will

[‡]Note that the buffer layer composition is not stoichiometric and therefore will contain some excess silicon as well. This excess silicon will increase the amorphous Si–Si bond density, resulting in an underestimation of the crystallinity. However, since the buffer layer thickness is only 1 nm, compared to 3 nm for the silicon-rich layer, we expect this effect to be limited and assume it can be neglected.

not be SiO_2, but has a lower stoichiometry. This in turn will lower its energy barrier, increasing the tunneling probability and possibly enlarge the inter-particle distance at which the mobility remains sufficiently high [21]. However, for simplicity we will keep an inter-particle distance range from 0 to 2 nm. Assuming a maximum achievable crystallinity of 0.4 for PECVD films, an optimal stoichiometry to achieve the highest density of non-touching, closely spaced nanocrystals can be found. This optimal stoichiometry is $SiO_{0.84}$. In contrast, films deposited using magnetron sputtering are reported to lead to complete phase separation [63]. Assuming all silicon clusters crystallize upon annealing, this will lead to a crystallinity equal to unity. In reality the sub-oxide shell around the nanocrystal core will limit complete crystallization [78], but for simplicity we assume a crystallinity equal to unity. In that case the optimal stoichiometry of the silicon-rich layers is approximately $SiO_{1.4}$ for this structure. Note that in both cases the 2D nanocrystal density with nearest-neighbor within 2 nm is $1.3 \times 10^{12}\,\mathrm{cm}^{-2}$. This value corresponds well with results obtained experimentally by Laube *et al.* for single 4.5 nm thick layers [79] and is slightly lower than experimental results obtained by Gutsch *et al.* for single 3.5 nm thick layers [67]. However, we should note that these reported values are the total nanocrystal density, while we estimated the isolated nanocrystal density with nearest-neighbor within 2 nm. This excludes clustered nanocrystals and too isolated nanocrystals, which inevitably leaves out a portion of the total nanocrystal density. Furthermore, the thickness of the silicon-rich layer affects the estimated nanocrystal density, with lower values for thicker layers.

The optimal stoichiometry decreases for increasing silicon-rich layer thicknesses, as shown in figure 3.6. Note that the model's accuracy decreases for greater

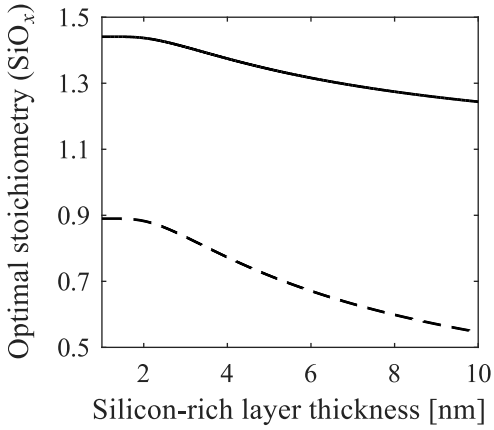

Figure 3.6: The optimal stoichiometry for films with varying silicon-rich layer thicknesses for a sample with crystallinity of 1 (solid line) and 0.4 (dashed line). The buffer layer thickness is kept constant at 1 nm.

silicon-rich layers thicknesses, as shown in figure 3.4. Nonetheless, from a theoretical perspective the observed trend for thick silicon-rich layers is still interesting. This is caused by the differences in volume between a nanocrystal and its enclosing box (see figure 3.2). The volume of a nanocrystal is $\frac{4}{3}\pi r^3$ and its enclosing box is approximately $2r(2r+d)^2$. The volume ratio of the enclosing box over the nanocrystal decreases with increasing silicon-rich layer thickness, explaining de trend observed in figure 3.6 for relatively large silicon-rich layer thicknesses. However, for very small silicon-rich layer thicknesses the optimal composition does not vary. To explain this, we look closer into their probability density functions, shown in figure 3.7. The peak at 1 nm is caused by the availability of nearest

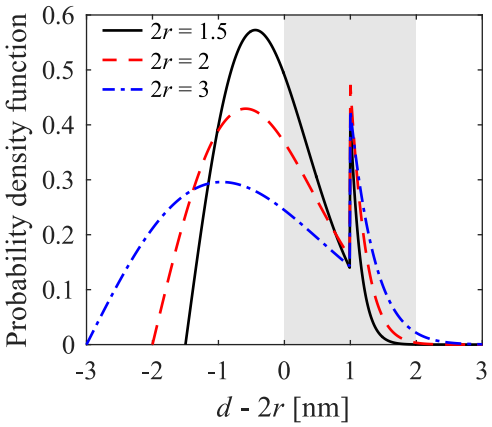

Figure 3.7: The nearest neighbor distance probability density functions for samples with silicon-rich layer thicknesses of 1.5, 2 and 3 nm and buffer layer thickness of 1 nm, calculated using their respective optimal compositions. The gray area depicts the range of desired nearest neighbor distances. Shorter distances imply clustering and greater distances lead to an insufficient tunneling probability.

neighbors in the neighboring silicon-rich layers. The probability density function broadens for larger silicon-rich layer thicknesses, because its standard deviation is related to the 2D nanocrystal density by $\sigma_{2D} \propto 1/\sqrt{n_{2D}}$ [77]. Since n_{2D} decreases for greater silicon-rich layer thicknesses, the probability density functions broaden. The optimal composition depends on the probability of finding a nearest neighbor within a limited range (2 nm for SiO_x). For silicon-rich layer thicknesses up to approximately 2 nm, the probability of finding a nearest neighbor beyond 2 nm is negligible, as can be observed in figure 3.7. For these thicknesses there is no reason to increase the nanocrystal density, since more closely packed nanocrystals will not increase the probability of finding a nearest neighbor within 2 nm. On the contrary, an increase in nanocrystal density will increase the probability of clustering.

3.4 Conclusions

We demonstrated an analytical method to optimize the composition of silicon-rich layer for different crystallinities thicknesses in order to achieve the highest density of non-touching and closely spaced silicon nanocrystals after annealing. The optimal stoichiometry depends on the crystallinity decreases for increasing silicon-rich layer thicknesses. However, for very small silicon-rich layer thicknesses the optimal composition does not vary. This method can be used to find the best as-deposited composition in order to achieve optimal nanocrystal density and spacing after a subsequent annealing step.

4

Obtaining the nanocrystal size distribution

This chapter is based on the following publication:

M. van Sebille, L. J. P. van der Maaten, L. Xie, K. Jarolimek, R. Santbergen, R. A. C. M. M. van Swaaij, K. Leifer, M. Zeman, *Nanocrystal size distribution analysis from transmission electron microscopy images*, Nanoscale **7**, 20593–20606 (2015).

Abstract

We propose a method with minimal bias caused by user input to quickly detect and measure the nanocrystal size distribution from transmission electron microscopy (TEM) images using a combination of Laplacian of Gaussian filters and non-maximum suppression. We demonstrate the proposed method on bright-field TEM images of an a-SiC:H sample containing embedded silicon nanocrystals with varying magnifications and we compare the accuracy and speed with size distributions obtained by manual measurements, a thresholding method and `PEBBLES`. Finally, we analytically consider the error induced by slicing nanocrystals during TEM sample preparation on the measured nanocrystal size distribution and formulate an equation to correct for this effect.

4.1 Introduction

As explained in section 1.4.2, a quick method to measure nanocrystals in TEM images with minimal user input to minimize user bias has been lacking. In this chapter we propose a semi-automatic method to quickly measure the sizes of nanocrystals in any type of TEM image in order to obtain the nanocrystal size distribution, using a combination of Laplacian of Gaussian (LoG) filters, non-maximum suppression, and a boundary overlay. The only user input required is a minimum and a maximum nanocrystal size, and a non-maximum suppression threshold value. After applying the automated part of the method, the user is able to judge the quality of the result in a manual verification step. We also show in this chapter that these parameters can be determined for one image and then be accurately used in similar images. Furthermore, we analytically consider the effect of slicing nanocrystals during sample preparation on the nanocrystal distribution as measured with TEM. We establish equations describing this effect and propose a simple method to correct for it.

This chapter is organized as follows. We first describe the experimental details under which the sample was fabricated and measured in section 4.2. Next, we describe the principles and mathematics behind the developed method in section 4.3 and we go through the method step by step, demonstrating the steps on a small section of a bright-field TEM (BF-TEM) image. The results of applying our method on several test images, and the results of the other methods we use to compare with, are shown in section 4.4. We also present the effect of nanocrystal slicing on the obtained size distribution for one of the test images. Finally, we discuss the results and each method's advantages and disadvantages in section 4.5. Furthermore, we also compare evaluate the effect of slicing on the observed size distribution.

4.2 Experimental details

All TEM images were made on the same sample. We deposited a-$Si_{0.71}C_{0.29}$:H on quartz substrates from G.M. Associates in a radio frequency plasma-enhanced chemical vapor deposition reactor, described in section 2.1.1. The sample was deposited and annealed with the following deposition parameters: a power density of 0.139 W cm^{-2}, substrate temperature of 360 °C, and SiH_4 and CH4 flows of 10.2 and 91.8 sccm, respectively. After deposition the sample was annealed in a furnace at 1100 °C for 60 min.

Transmission electron microscopy (TEM) measurements were performed using a FEI Tecnai F30ST microscope, described in section 2.2.5. Conventional TEM sample preparation techniques including mechanical polishing and grazing incidence (6°, 5 kV) Ar-ion milling was used to obtain samples in plan-view geometry.The sample thickness is assumed to be 25 nm, which was the sample target thickness during sample preparation.

All computer assisted analyses were performed on a computer with Intel Core2 Quad CPU at 2.66 GHz, with 4 GB RAM and 64-bit operating system, using MATLAB R2015A.

4.3 Theory, method and distribution correction

4.3.1 Theory

The analysis method is based on the application of Laplacian of Gaussian (LoG) filters, which are commonly used in image processing [80–82]. These filters are blob-detectors which respond to circular image structures with certain sizes, determined by their scale parameters. This makes these filters very suitable for the detection of nanocrystals in TEM images. LoG filters combine a Gaussian and Laplacian filter in one. The Gaussian filter G serves to reduce noise by smoothing the image and is given by

$$G(x, y, \sigma) = \frac{1}{2\pi\sigma^2} \exp\left(-\frac{x^2 + y^2}{2\sigma^2}\right), \tag{4.1}$$

where x and y are the two dimensions of the image, and σ is the scale parameter. The Laplacian filter is the sum of the second spatial derivative in x- and y-directions, and calculates the local curvature of intensities in the image $I(x, y)$ and is given by

$$L(x, y) = \frac{\partial^2 I}{\partial x^2} + \frac{\partial^2 I}{\partial y^2}. \tag{4.2}$$

Combining these two filters results in the second spatial derivative of the Gaussian filter, or Laplacian of Gaussian filter $\nabla^2 G$

$$\nabla^2 G(x, y, \sigma) = \frac{\partial^2 G}{\partial x^2} + \frac{\partial^2 G}{\partial y^2}. \tag{4.3}$$

An example of a LoG filter is shown in figure 4.1. The scale parameter σ determines the width of the LoG filter in x- and y-dimensions. A range of LoG filters with different scale parameters is applied. All possible scales within this range are referred to as the scale space. The scale space is sampled linearly, since the nanocrystal size distributions are expected to be relatively narrow, spanning one or at most two orders of magnitude.

The intensity of the response of LoG filters is used in a later step to determine the position and size of the detected nanocrystals, as described in section 4.3.2. This response decreases as its scale parameter increases, so in order to prevent a bias towards smaller scales, the LoG filters are normalized by multiplying them with σ^2 [80]

$$\nabla^2_{norm} G(x, y, \sigma) = \sigma^2 \left(\frac{\partial^2 G}{\partial x^2} + \frac{\partial^2 G}{\partial y^2}\right), \tag{4.4}$$

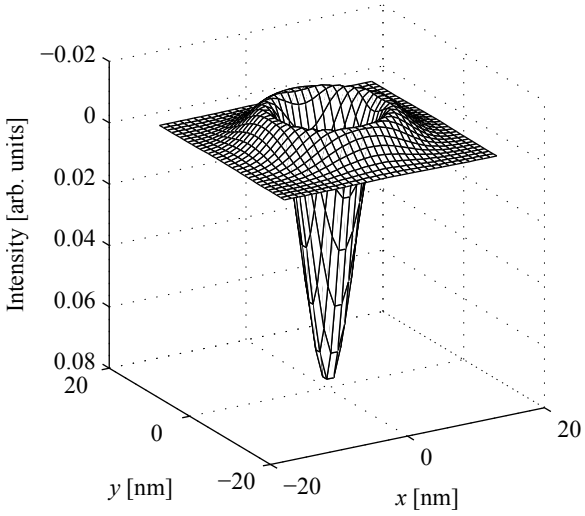

Figure 4.1: A normalized LoG filter with $\sigma = 8\,\text{nm}$.

where $\nabla^2_{norm} G(x, y, \sigma)$ is the normalized Laplacian of Gaussian (NLoG) filter. NLoG filters are applied by convoluting the original image $I(x, y)$ with the NLoG filter $\nabla^2_{norm} G$, resulting in a three-dimensional response image $f(x, y, \sigma)$ [81]

$$f(x, y, \sigma) = \nabla^2_{norm} G(x, y, \sigma) * I(x, y). \tag{4.5}$$

The response of an NLoG filter achieves a maximum amplitude at the center of the nanocrystal, provided the scale of the NLoG filter matches the scale of the nanocrystal. For disks, this is the case when the zero-crossing of an NLoG filter overlaps with the edge of the nanocrystal and can be expressed as $\sigma = r/\sqrt{2}$, where r is the nanocrystal radius in the TEM image. However, for the intensity profiles of nanocrystals in amorphous silicon alloys this is not the case, shown in figure 4.2. The ratio between a nanocrystal radius and its matching scale parameter was obtained using the validation image (see section 4.4.1). The ratio was determined for all correctly detected nanocrystals (the number of detected nanocrystals minus false positives) and was found to be 1.52 ± 0.113, so

$$\sigma = \frac{r}{1.52}. \tag{4.6}$$

This will be used in section 4.3.2.

4.3.2 Method

The semi-automatic method consists of a series of steps in order to quickly determine the position and nanocrystal size distribution within a TEM image. These steps are:

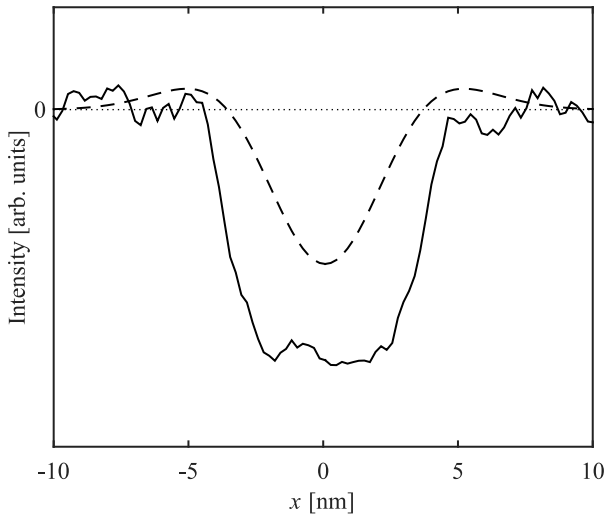

Figure 4.2: 1D intensity profile of a nanocrystal with radius of 4.2 nm (solid line), the LoG filter corresponding to the maximum intensity response, with σ of 2.53 nm (dashed line) and zero intensity (dotted line).

1. **Preprocessing** of the image
2. **Convolution of TEM image with NLoG filters** within a sampled scale space
3. **Determining the position and characteristic scale of nanocrystals** by finding the local maximums in the 3D NLoG response and subsequent application of non-maximum suppression
4. **Verification** of analysis by overlaying the obtained nanocrystal positions and boundaries on the original TEM image

These steps will be discussed in more detail below. The method is available as `MATLAB` code.*

Preprocessing.

During preprocessing the contrast of a raw TEM image is adjusted for two purposes. The first is to make the contrast profiles similar for the different TEM images. This allows us to determine the optimal non-maximum suppression threshold value, as described in section 4.3.2, and directly apply it to comparable TEM images. The second reason is to ensure the user can clearly distinguish the nanocrystals from the background, allowing the user to verify whether the method worked correctly, as described in section 4.3.2. Preprocessing is realized

*`MATLAB` code available. See DOI: 10.1039/c5nr06292f

by normalizing the intensity of the image $I(x, y)$ and subsequently changing the contrast to match a normally distributed histogram with mean and standard deviation of 0.5 and 0.1, respectively. This is achieved by a gray-scale transformation T to minimize

$$|c_1(T(k)) - c_0(k)|, \tag{4.7}$$

where c_0 is the cumulative histogram of $I(x, y)$ and c_1 is the cumulative sum of the normally distributed histogram for all intensities k [83]. The result is that all images have comparable contrast. Note that all analyses were performed after these preprocessing steps, except for the PEBBLES method, which uses the original TEM image.

Convolution with NLoG filters.

The scale space range is determined by estimating the range of nanocrystal radii in the TEM image. The smallest expected nanocrystal size is determined by an optimization using the validation image, described in section 4.4.1. The step size in expected nanocrystal radii is set by an increment of 1 pixel and the largest nanocrystal radius is estimated by the user. The largest nanocrystal can be estimated by manually guessing or measuring the largest nanocrystal in a given image. The expected range of nanocrystal sizes is then divided by 1.52, according to equation (4.6) to obtain the sampled scale space. Note that when the largest nanocrystal radius to be detected is set too small, the biggest nanocrystals will not be detected correctly, resulting in a bias towards smaller nanocrystals. However, this can be verified quickly in the verification step, discussed in section 4.3.2. When the largest nanocrystal is set too big, computation times will increase and there is a risk of incorrectly detecting other, larger features, should there be any. When the smallest nanocrystal radius to be expected is set too small, there is a risk of falsely detecting noise as nanocrystals. Alternatively, when the smallest expected nanocrystal size is too large, the smallest nanocrystals might not be detected and there might be a bias towards bigger nanocrystals.

To illustrate this step, we consider a small section of a BF-TEM image, shown in figure 4.3a, containing several small nanocrystals and a bigger nanocrystal near the top of the image. Figures 4.3b and 4.3c show the result of the convolutions of the original TEM image with NLoG filters with scales of 1.9 nm and 4.3 nm, respectively. The result of the small NLoG filter, shown in figure 4.3b, is that the contrast for the small nanocrystal (labeled B) is enhanced. Also note that the bigger nanocrystal (labeled A) results in a relatively low intensity. Since the background noise feature size is quite close to the size of the smallest nanocrystals, the background noise is also enhanced to some extent, although not as significantly as the small nanocrystals. The result of the larger NLoG filter, shown in figure 4.3c, is that the largest nanocrystal A is enhanced with the highest image intensity in its center. The smaller nanocrystals are also detected, but their intensity is lower, indicating that the scale parameter of this NLoG filter is not the best match for these nanocrystals.

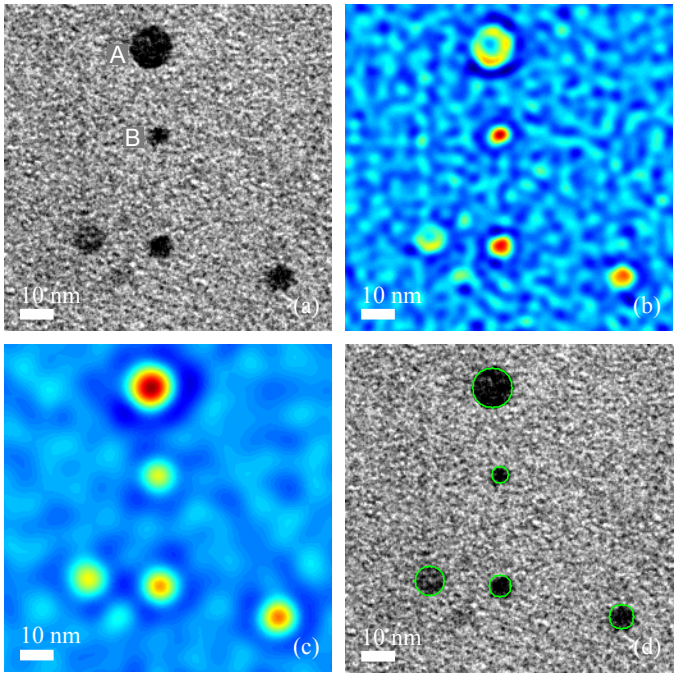

Figure 4.3: (a) A section of a BF-TEM image with several nanocrystals of different sizes. The result of the convolutions of the original image with NLoG filters with σ of 1.9 nm (b) and 4.3 nm (c), corresponding to nanocrystal radii of 2.9 nm and 6.5 nm, respectively. Figures (b) and (c) are displayed with the same color scale, which indicates the intensity of the resulting response image $f(x, y, \sigma)$, see equation (4.5). (d) Nanocrystals encircled to verify correct identification of nanocrystals.

Determining the position and characteristic scale of nanocrystals.

Next, non-maximum suppression (NMS) is applied to simultaneously determine the nanocrystal position and size, and to discard noise. This is achieved by finding the local maximum values in the three-dimensional response image $f(x, y, \sigma)$, from equation (4.5). In order to prevent the false detection of noise as nanocrystals, a maximum is only considered as such when it is the maximum value within its local $5 \times 5 \times 5$ pixel-subset of the three-dimensional array and if its value is equal to or larger than the NMS threshold. The physical size of 5 pixels depends on the pixel size of the TEM image and ranges between 1.035 to 2.880 nm for the images used in this study.

The first of these two conditions causes only the best scale space-nanocrystal match to show up as a maximum. If we consider figure 4.3c, we see that a scale parameter of 4.3 nm enhances the smallest nanocrystal (labeled B), with its center the local intensity peak in the (x, y) plane. However, in scale space, it is not the

maximum, since figure 4.3b shows the same nanocrystal with higher intensity. In scale space, the intensity at that position will change and peak at the best scale space-nanocrystal match.

The second requirement, stating that each intensity peak in the local $5 \times 5 \times 5$ sub-array should at least be as high as the NMS threshold value, discards noise. Figures 4.3b and 4.3c show several lower intensity peaks due to background noise. These peaks might have a local maximum at some scale parameter, but they are not nanocrystals. The NMS threshold prevents the noise from being detected as nanocrystals. The NMS threshold value influences the outcome of the procedure significantly and could lead to inaccurate results if applied incorrectly. However, we will show that this threshold can be determined for one type of TEM image and can then be safely and correctly applied to similar TEM images, limiting user-caused bias. Furthermore, the next step is used to manually verify the outcome of the automated method and an incorrect value will be clear.

Verification.

After obtaining a three-dimensional array with nanocrystal position and size, the outcome can be verified by overlaying the results with the original TEM image, as shown in figure 4.3d. This allows for a quick verification of the applied parameters and shows whether anything has been set incorrectly. A too low value for the largest nanocrystal would reveal the biggest nanocrystals not encircled. When the NMS threshold parameter is set too low, noisy background peaks will be encircled and when set too high, some nanocrystals will not be encircled.

4.3.3 Distribution correction

During TEM sample preparation the sample is thinned to several tens of nanometers. When the sample thickness t approaches the size of nanocrystals, the chance of slicing a significant number of nanocrystals increases and thus the measured nanocrystal size distribution will get distorted. For simplicity, we will assume all nanocrystals are spherically shaped. When a nanocrystal is depicted in a TEM image, we observe its two-dimensional projection of the three-dimensional spherical nanocrystal.

There are three cases we should consider: (i) when the nanocrystal's center is inside the sample, (ii) when its center is less than R outside the sample, and (iii) when the nanocrystal's center is more than R outside the sample. Since we observe the nanocrystal's 2D projection, and we are using transmission measurements, for case (i) the apparent radius r is the same as its true radius R and will show up as such in the TEM image, as shown schematically in figure 4.4a. However, when a nanocrystal is sliced during sample preparation and its center is located up to R outside the sample (case ii), the apparent radius R will differ from r, as shown in figure 4.4b. The third case, when a nanocrystal is located more than R outside the sample (case iii), it will not be measured at all. We assume that the

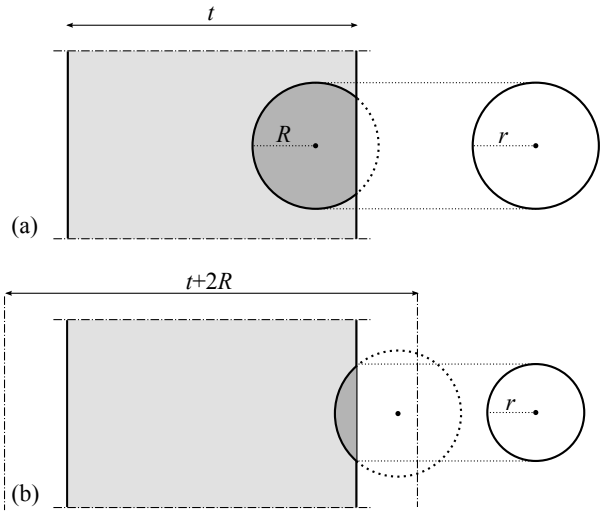

Figure 4.4: Schematic of a sample (light gray) with a nanocrystal (dark gray), with its center (•) inside the sample (a) and up to R outside the sample (b)

nanocrystals are distributed randomly throughout the sample. Nanocrystals that show up in TEM images have their center located within $t + 2R$. With this, the probability $P_{outside}$ of a nanocrystal's center for a given nanocrystal in the image being located up to R outside the sample, can be expressed as follows

$$P_{\text{outside}}(t, R) = \frac{2R}{t + 2R}. \tag{4.8}$$

The probability of a nanocrystal's center being located inside the sample is then

$$P_{\text{inside}}(t, R) = 1 - \frac{2R}{t + 2R} = \frac{t}{t + 2R}. \tag{4.9}$$

If a nanocrystal, shown schematically in figure 4.5, is sliced it happens at a random position, so every position x is equally likely. The probability density function $f_{apparent}$ of finding an apparent radius r is then

$$f_{\text{apparent}}(r) = C\frac{\partial x}{\partial r}, \tag{4.10}$$

where C is a normalization constant. According to Pythagoras' theorem

$$x^2 + r^2 = R^2, \tag{4.11}$$

which can be rewritten to

$$x = \pm\sqrt{R^2 - r^2}. \tag{4.12}$$

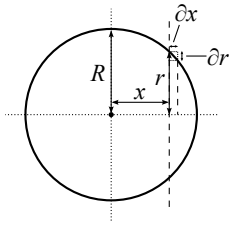

Figure 4.5: A nanocrystal shown schematically.

After finding and replacing the normalization constant in equation (4.15), the positive and negative versions of equation (4.12) both lead to equation (4.16). For simplicity we will continue the derivation with only the negative one. This leads to the following derivative

$$\frac{\partial x}{\partial r} = \frac{-r}{\sqrt{R^2 - r^2}}. \tag{4.13}$$

Combining equations (4.10) and (4.13) gives

$$f_{\text{apparent}}(r) = C\frac{-r}{\sqrt{R^2 - r^2}}. \tag{4.14}$$

The normalization constant C can be found by equating

$$\int_0^R f_{\text{apparent}}(r)\ \mathrm{d}x = 1 \rightarrow C = \frac{-1}{R}. \tag{4.15}$$

Combining equations (4.14) and (4.15) leads to

$$f_{\text{apparent}}(r) = \frac{r}{R\sqrt{R^2 - r^2}}. \tag{4.16}$$

The probability $P_{apparent}$ of finding a nanocrystal with apparent radius r in the interval $a \leq r \leq b$ can then be calculated with

$$P_{\text{apparent}}(r) = \int_a^b \frac{r}{R\sqrt{R^2 - r^2}}\,\mathrm{d}r. \tag{4.17}$$

For a nanocrystal with real radius of 5 nm, the result is shown in figure 4.6. The apparent radius for a nanocrystal measured by TEM depends on the real radius R and the sample thickness t and by combining equations (4.8), (4.9) and (4.17) can be written as follows

$$r(R,t) = R\left[\frac{2R}{t+2R}\int_0^R \frac{r}{R\sqrt{R^2 - r^2}}\,\mathrm{d}r + \frac{t}{t+2R}\right]. \tag{4.18}$$

This equation can be used on a known nanocrystal size distribution in order to calculate the distribution of apparent radius r, for a given sample thickness, as

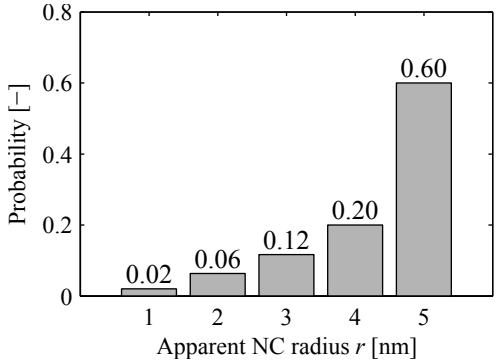

Figure 4.6: Probability of finding apparent radius r for real radius R of 5 nm, when the nanocrystal is sliced at a random position.

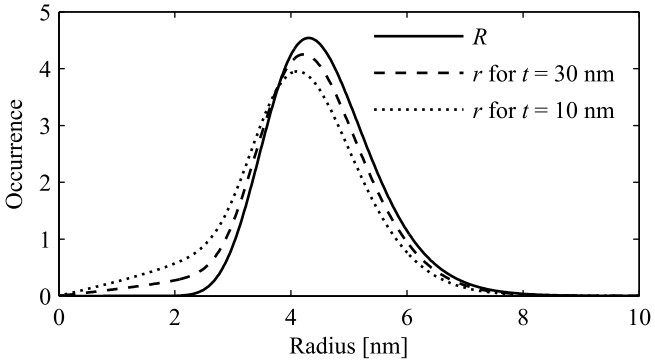

Figure 4.7: A log-normally distributed real nanocrystal radius R with $\mu = 1.5$ nm and $\sigma = 0.2$ nm (solid) and apparent radius distribution r for sample thickness of 30 and 10 nm shown as dashed and dotted lines, respectively.

shown in figure 4.7. This figure shows that the apparent nanocrystal size distribution can be significantly different from its real nanocrystal size distribution, depending on the nanocrystal size and sample thickness. Greater nanocrystal radii and a thinner sample thickness leading to more distorted apparent size distributions.

In practice the real size distribution is unknown. From TEM images we can obtain the size distribution of apparent radii and from the sample preparation we can get a close approximation of the sample thickness. We can then fit the real nanocrystal size distribution using equation (4.18), thereby correcting for possible slicing of nanocrystals.

4.4 Results

The proposed method to determine the nanocrystal size distribution will be demonstrated and tested as follows. It will be calibrated using a validation image, a BF-TEM image, shown in figure 4.8. This image will be used to determine the NMS threshold value and maximum nanocrystal size in section 4.4.1. This image has a relatively homogeneous background and high contrast between nanocrystals and background, making it easy to manually annotate the nanocrystals and to calibrate the proposed method. Next, using these parameters the method will be applied on a test set in section 4.4.2. The accuracy of the results on the test set is a measure of the quality of the method proposed.

Since the nanocrystal size distribution of any sample is not known a priori, there is no objective way to evaluate the performance of such an analysis method. Therefore we compare the results of our proposed method with a size distribution obtained by manually annotating all nanocrystals in the image. We assume that the nanocrystals annotated manually are correct, which implies that nanocrystals found automatically with the NLoG method, but not manually are false positives and vice versa are false negatives. The false positives and false negatives can be expressed as percentages of the total number of nanocrystals found with manual annotation in the image to indicate the accuracy of the method. In addition to the accuracy in detecting nanocrystals, there should not be a significant bias toward smaller or larger nanocrystals detected. The nanocrystal diameter found with the automated method should correspond with the actual nanocrystal size. The obtained size distribution should be accurate and represent the actual nanocrystal size distribution. Therefore we compare the obtained size distribution with the size distribution obtained from manual annotation of the nanocrystals. We also compare the mean nanocrystal size and mean absolute deviation of the size distribution. Additionally, we compare the results of our method to results obtained by `PEBBLES` and a thresholding method. `PEBBLES` was used with `MATLAB` R2014a and used according to the recommendations by Mondini *et al.* [47]. It was calibrated for all three images individually before running the automated method. First 10 random nanocrystals were fitted manually using the spherical quadratic model. Subsequently the image was fitted automatically with the same model, using the manually fitted average equivalent diameter and delta as guess diameter and delta value and a grid with default spacing, see Ref [47]. For the threshold method, all pixels with intensity values smaller than the threshold are considered to be part of a nanocrystal and all other pixels are background. Similar to the NLoG method, the threshold value was optimized for the validation image and subsequently used to analyze the test set.

4.4.1 Validation

The NMS threshold value and the smallest and largest nanocrystal radius are the three input parameters for the NLoG method. The largest nanocrystal in the val-

idation image, shown in figure 4.8, is measured manually and is approximated to be 8 nm for the validation image. Setting a higher largest nanocrystal radius

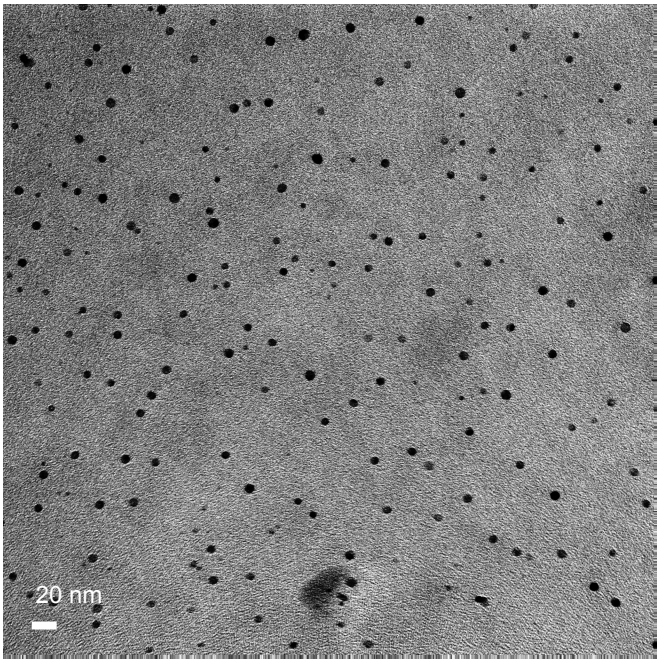

Figure 4.8: BF-TEM image used as validation image, taken at 35 000× magnification and pixel size of 0.379 nm.

mainly increases computation time, but does not affect results significantly. In order to determine the optimal NMS threshold and smallest nanocrystal radius, these parameters were varied with the goal of minimizing the sum of false positives and false negatives. The minimum of the sum of false positives and false negatives for the validation image is at a NMS threshold value of 0.203 and smallest nanocrystal radius of 4 pixels.

4.4.2 Test set

Next, the optimized parameters obtained from the validation image are applied on a test set, containing similar BF-TEM images.

Test image 1

The first is test image 1, taken at a lower magnification than the validation image and shown in figure 4.9a. This image has a background intensity gradient with a low-contrast region in the bottom-left corner and it has three nanocrystal clusters,

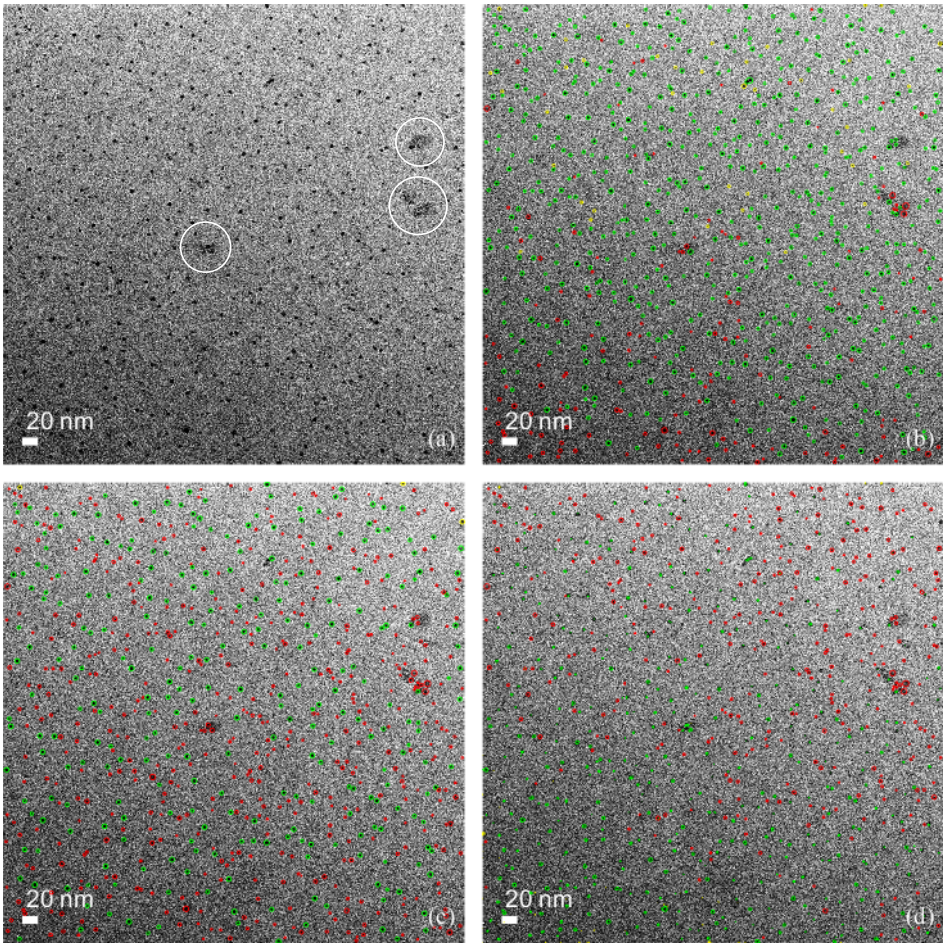

Figure 4.9: (a) BF-TEM image used as test image 1, taken at 22 500× magnification and pixel size of 0.576 nm. The three nanocrystal clusters are encircled in white. (b) The image with nanocrystals encircled detected using the NLoG method using a sampled scale space corresponding to nanocrystal radii of 4.6 to 8.6 nm (2.3 to 8.6 pixels) and NMS threshold of 0.203, optimized for the validation image. (c) TEM image with nanocrystals encircled detected using `PEBBLES` with guess diameter of 15.4 pixels, delta of −0.3937 and 99 327 grid points spaced by 7.0. (d) TEM image with nanocrystals encircled detected using threshold with value of 0.099 optimized for the validation image. Nanocrystals encircled green, yellow and red indicate correctly detected nanocrystals, false positives and false negatives, respectively.

which are encircled in white. The nanocrystals detected by the NLoG, PEBBLES and threshold methods are encircled in figures 4.9b–d, respectively. The NLoG method does not detect the nanocrystals in the low-contrast part of the image, while both PEBBLES and the threshold do detect some nanocrystals in this region. The NLoG method detects nanocrystals in the rest of the image as does PEBBLES. The thresholding method predominantly detects nanocrystals in the bottom-left corner and few in the rest of the image. NLoG correctly detects most nanocrystals in two of the three nanocrystal clusters, while the other two methods do not detect these nanocrystals.

The size distributions obtained by the manually annotated nanocrystals and the NLoG, PEBBLES and threshold method for test image 1 are shown in figure 4.10a–d, respectively. The nanocrystal distribution from manual annotation

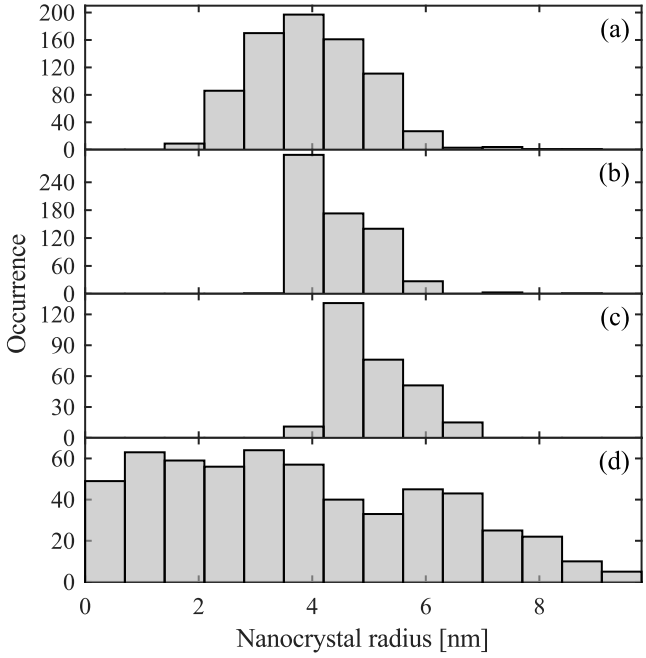

Figure 4.10: Histogram of nanocrystal size distribution for test image 1, obtained from manual annotation of nanocrystals (a), NLoG method (b), PEBBLES (c) and threshold (d).

shows a single size distribution with an average size of approximately 4 nm. Both the NLoG and PEBBLES methods detect only the upper part of this size distribution. The NLoG method detected 270 nanocrystals with radii between 3.6 to 4.2 nm, corresponding to the smallest scale in the sampled scale space. The size distribution obtained with the threshold differs most from the distribution obtained by manual annotation.

The results of the different methods applied on test image 1 are listed in ta-

ble 4.1.[†] The number of detected nanocrystals is the sum of correctly detected nanocrystals and false positives. The speed is defined as the number of correctly detected nanocrystals, which is the number of detected nanocrystals minus false positives, per second.

The NLoG method detected most nanocrystals out of the three automated methods. It had the lowest number of false negatives, but still this was 21 % of the total number of nanocrystals. The mean nanocrystal radius measured by the NLoG method is bigger than the mean radius obtained by manual annotation and differs by 7.3 %. The mean absolute deviation obtained with the NLoG method is closest to the one determined by manual annotation. The fastest method is the thresholding, followed by the NLoG method.

Test image 2

In the following we will analyze test image 2 (see figure 4.11a), which was taken at a greater magnification than the validation image. The nanocrystals detected by the NLoG, PEBBLES and threshold methods are encircled in figures 4.11b–d, respectively. The NLoG method correctly detects nanocrystals throughout the image, but did not detect some of the nanocrystals near the top edge of the image. PEBBLES did not detect a large number of nanocrystals throughout the image.

The size distributions obtained by the manually annotated nanocrystals and the NLoG, PEBBLES and threshold method for test image 2 are shown in figure 4.12a–d, respectively. A bimodal size distribution is obtained from manual annotation and the NLoG method matches this bimodal distribution closely. PEBBLES detected only nanocrystals with the smallest of the two size distributions, missing the larger of the nanocrystals. The thresholding method predominantly detected very small nanocrystals.

The results of the different methods applied on test image 2 are listed in table 4.2. The NLoG method generated 5.0 % false positives, while PEBBLES did not generate any false positives. The NLoG method had the lowest number of false negatives, however, compared to PEBBLES and threshold. Both the mean nanocrystal radius and mean absolute deviation obtained with the NLoG method are closest to their values obtained from manual annotation.

Test image 3

In order to illustrate the potential of the routine, we have also applied it on a more challenging image with irregular background and lower contrast, shown in figure 4.13a. A low-contrast region in the lowest left corner of the image is encircled in white. The nanocrystals detected by the NLoG, PEBBLES and threshold meth-

[†]The number of detected nanocrystals plus false negatives minus false positives does not (always) equal the number of detected nanocrystals using manual annotation. This is caused by touching nanocrystals. If nanocrystals touch in manual annotation, they are counted as a single nanocrystal. If they happen not to touch when detected automatically, they are then counted as two separate nanocrystals. The other way around can also occur.

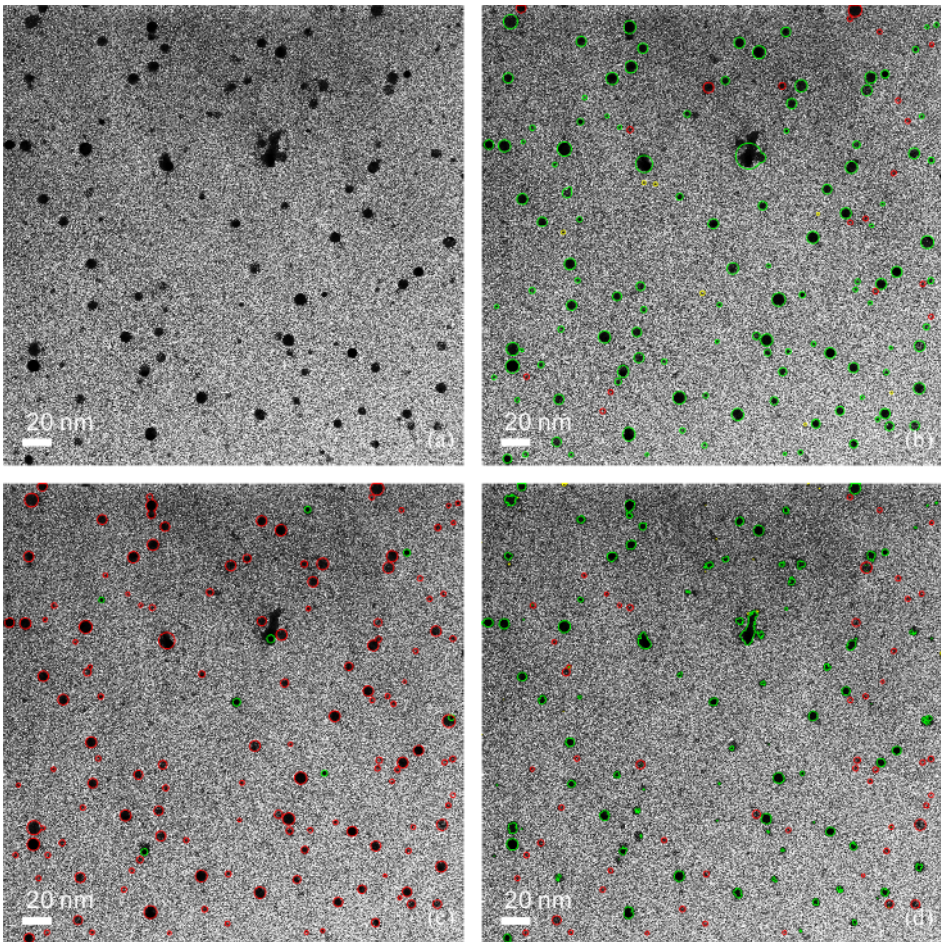

Figure 4.11: (a) BF-TEM image used as test image 2, taken at 63 000× magnification and pixel size of 0.207 nm. (b) The image with nanocrystals encircled detected using the NLoG method using a sampled scale space corresponding to nanocrystal radii of 0.83 to 7.88 nm (4 to 38 pixels) and NMS threshold of 0.203, optimized for the validation image. (c) TEM image with nanocrystals encircled detected using `PEBBLES` with guess diameter of 23 pixels, delta of −0.0073 and 40 392 grid points spaced by 11.0. (d) TEM image with nanocrystals encircled detected using threshold with value of 0.099 optimized for the validation image. Nanocrystals encircled green, yellow and red indicate correctly detected nanocrystals, false positives and false negatives, respectively.

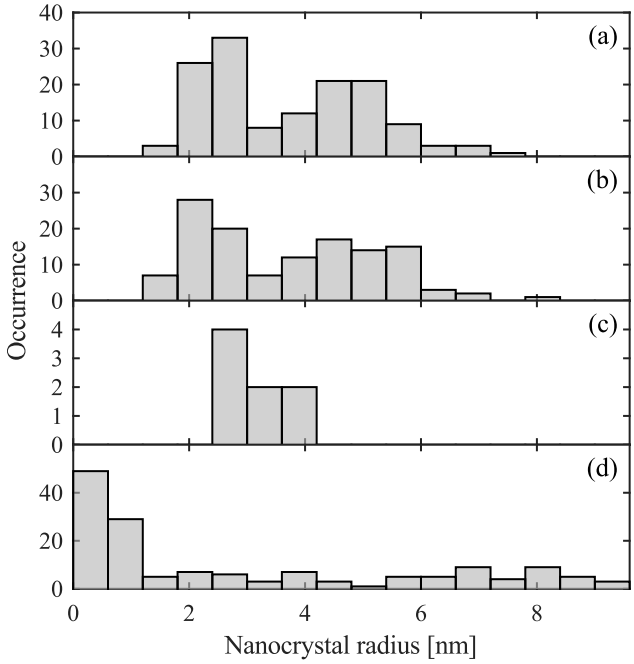

Figure 4.12: Histogram of nanocrystal size distribution for test image 2, obtained from manual annotation of nanocrystals (a), NLoG method (b), PEBBLES (c) and threshold (d).

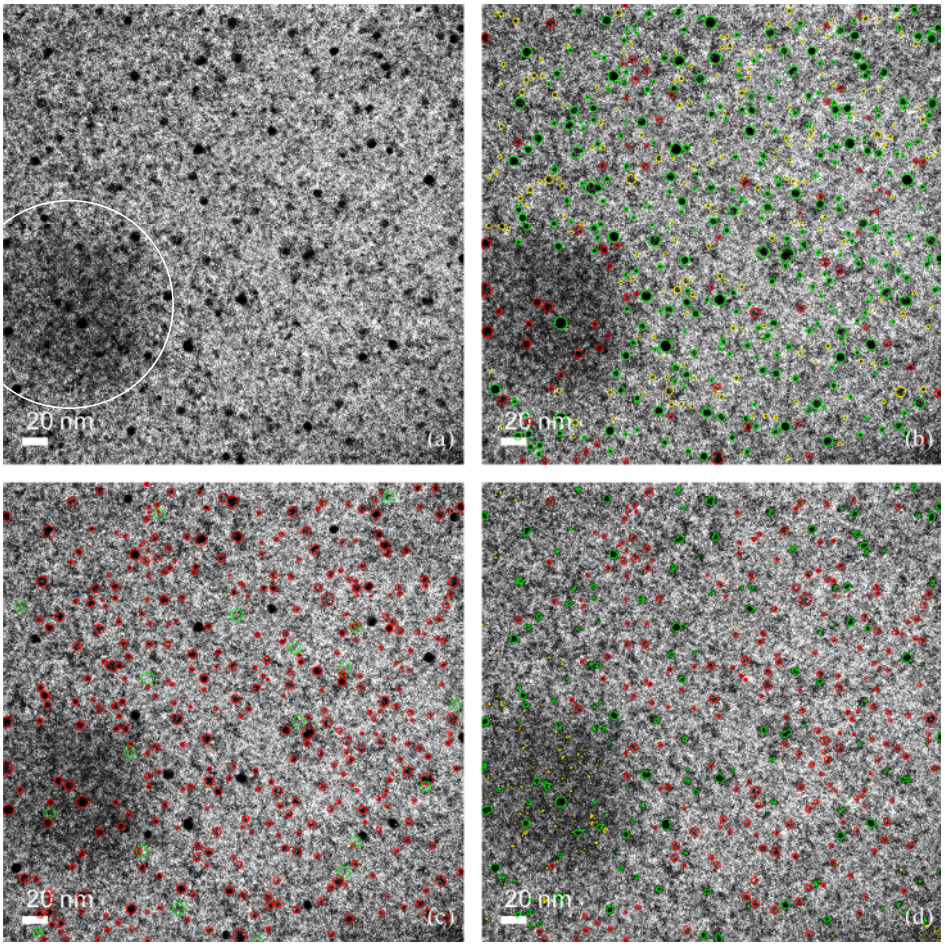

Figure 4.13: (a) BF-TEM image used as test image 3, taken at 52 000× magnification and pixel size of 0.254 nm. The low-contrast region is encircled in white. (b) The image with nanocrystals encircled detected using the NLoG method using a sampled scale space corresponding to nanocrystal radii of 1.02 to 5.85 nm (4 to 23 pixels) and NMS threshold of 0.203, optimized for the validation image. (c) TEM image with nanocrystals encircled detected using `PEBBLES` with guess diameter of 39 pixels, delta of -0.0052 and 13 608 grid points spaced by 19.0. (d) TEM image with nanocrystals encircled detected using threshold with value of 0.099 optimized for the validation image. Nanocrystals encircled green, yellow and red indicate correctly detected nanocrystals, false positives and false negatives, respectively.

Table 4.1: Results of manual annotation, NLoG, PEBBLES and threshold on test image 1

Method	Detected	False positives	False negatives	Mean r [nm] (error)	MAD [nm] (error)	Time [s]	Speed [s^{-1}]
Manual	770	-	-	3.98	0.82	8820	0.09
NLoG	644	39 (5.1 %)	160 (21 %)	4.27 (7.3 %)	0.65 (21 %)	96	6.3
PEBBLES	284	3 (0.4 %)	483 (63 %)	5.18 (30 %)	0.59 (27 %)	10683	0.03
Threshold	576	75 (9.7 %)	333 (43 %)	3.84 (3.4 %)	2.03 (148 %)	0.5	938

Table 4.2: Results of manual annotation, NLoG, PEBBLES and threshold on test image 2

Method	Detected	False positives	False negatives	Mean r [nm] (error)	MAD [nm] (error)	Time [s]	Speed [s^{-1}]
Manual	140	-	-	3.70	1.26	1800	0.08
NLoG	127	7 (5.0 %)	19 (14 %)	3.79 (2.5 %)	1.43 (14 %)	694	0.17
PEBBLES	8	0 (0.0 %)	133 (95 %)	3.10 (16 %)	0.31 (75 %)	4326	0.002
Threshold	162	21 (15 %)	53 (38 %)	3.48 (5.9 %)	1.26 (151 %)	0.1	1382

Table 4.3: Results of manual annotation, NLoG, PEBBLES and threshold on test image 3

Method	Detected	False positives	False negatives	Mean r [nm] (error)	MAD [nm] (error)	Time [s]	Speed [s^{-1}]
Manual	390	-	-	3.59	1.10	4500	0.09
NLoG	499	183 (47 %)	76 (19 %)	3.08 (14 %)	1.10 (0.3 %)	312	1.01
PEBBLES	19	0 (0 %)	370 (95 %)	5.93 (65 %)	0.52 (53 %)	2653	0.007
Threshold	475	203 (52 %)	219 (56 %)	2.21 (39 %)	1.84 (68 %)	0.2	1388

ods are encircled in figures 4.13b–d, respectively. The NLoG method performed reasonably well throughout the entire image, except for the low-contrast region. The number of false negatives for PEBBLES is considerably higher, but the method detected nanocrystals throughout the image, including the low-contrast region. The threshold method detected all nanocrystals correctly in the low-contrast region, but also generated most false positives. For the rest of the image, the threshold method detected some of the nanocrystals correctly.

The size distributions obtained by the manually annotated nanocrystals and the NLoG, PEBBLES and threshold method for test image 3 are shown in figure 4.14a–d, respectively. The nanocrystal distribution from manual annotation

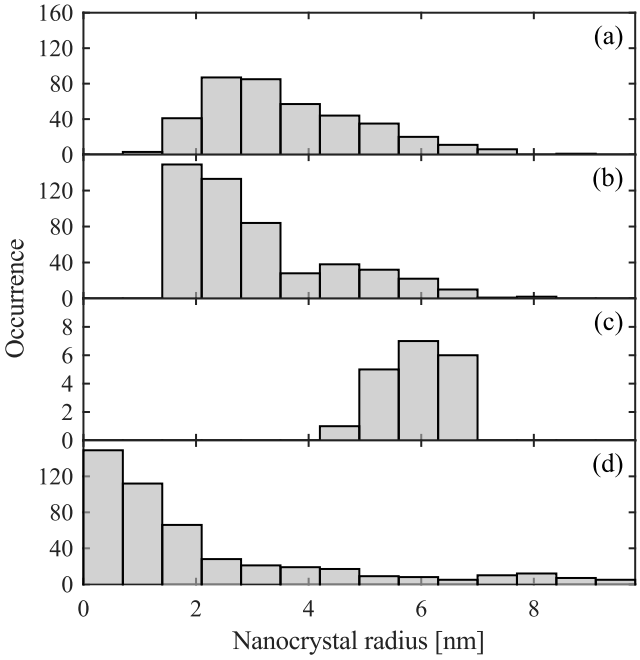

Figure 4.14: Histogram of nanocrystal size distribution for test image 3, obtained from manual annotation of nanocrystals (a), NLoG method (b), PEBBLES (c) and threshold (d).

shows a single size distribution with an average size of approximately 3.6 nm. The NLoG method detected significantly more smaller sized nanocrystals than obtained from manual annotation, while the histograms match reasonably well for the larger nanocrystals. PEBBLES detected only the larger nanocrystals in the size distribution. The size distribution obtained with the threshold differs most from the distribution obtained by manual annotation.

The results of the different methods applied on test image 3 are listed in table 4.3. The NLoG method generated 47 % false positives, while PEBBLES did not generate any false positives. The NLoG method had the lowest number of

false negatives, however, compared to PEBBLES and threshold. Both the mean nanocrystal radius and mean absolute deviation obtained with the NLoG method are closest to their values obtained from manual annotation.

Nanocrystal slicing correction

The effect of nanocrystal slicing will be demonstrated on test image 2, since it was obtained at highest magnification of the test set and has a high contrast. Nanocrystal size distributions are typically considered to be log-normally distributed [38, 42], so in order to correct for slicing, the size distribution obtained by manual annotation was fitted with a bimodal log-normal distribution, described by

$$L(r) = p\frac{1}{rs_1\sqrt{2\pi}}\exp\left[-\frac{(\ln r-\mu_1)^2}{2s_1^2}\right] + (1-p)\frac{1}{rs_2\sqrt{2\pi}}\exp\left[-\frac{(\ln r-\mu_2)^2}{2s_2^2}\right]. \quad (4.19)$$

The histogram of nanocrystal sizes obtained by manual annotation for test image 2 and the histogram with nanocrystal sizes corrected for slicing are shown in figure 4.15. There is a distinct difference in the shape of the nanocrystal size distribution after correcting for nanocrystal slicing. The distribution parameters of the measured and corrected nanocrystal sizes are listed in table 4.4.

Table 4.4: Distribution parameters of measured apparent nanocrystal radii r and corrected real radii R on test image 2

Radius	Measured r	Corrected R
p [-]	0.476	0.399
μ_1 [nm]	0.864	0.893
s_1 [nm]	0.161	0.095
μ_2 [nm]	1.57	1.59
s_2 [nm]	0.180	0.185
Mean [nm]	3.70	3.96
Mean absolute deviation [nm]	1.26	1.26

The mean nanocrystal radius after correction for nanocrystal slicing is 7.1 % larger than the measured mean nanocrystal radius, while the mean absolute deviation after correction does not change significantly. Furthermore, the relative contribution of the bigger nanocrystals increased after correction, indicated by a lower p.

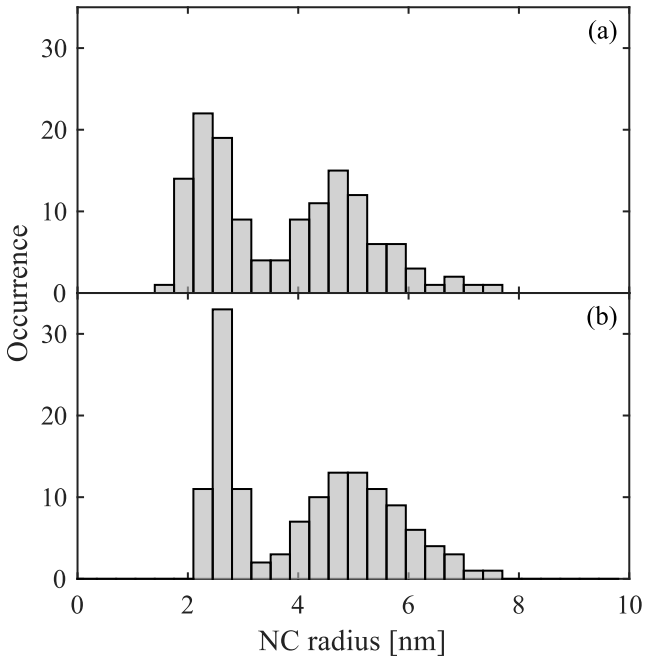

Figure 4.15: (a) Histogram of uncorrected, apparent nanocrystal radii r for test image 2, obtained by manual annotation. (b) Histogram of the log-normal size distribution of real radii R that would, after correcting for slicing, best fit the measured apparent radii distribution. The sample thickness is assumed to be 25 nm, which is the sample target thickness during this sample's preparation.

4.5 Discussion

Applying the three automated nanocrystal detection and measuring methods on the image test set, we can observe that all three methods have their own strengths and weaknesses. The threshold method is faster by at least two orders of magnitude than the fastest of the other methods. Its accuracy in false positives and false negatives and its accuracy in mean nanocrystal size and mean absolute deviation is low, however. Furthermore, the shape of the size distribution histograms differs most from the size distributions obtained by manual annotation.

PEBBLES is slowest for the images and settings used, even slower than manual annotation. It generated a negligible number of false positives, but the number of false negatives was highest of all methods in all test images. For all test images, the accuracy of PEBBLES in mean nanocrystal size was worst. For the unimodally distributed nanocrystal sizes of test image 1, its accuracy in mean absolute deviation was worse than the NLoG method, but not as bad as the threshold method. The histogram shape for test image 1 is similar to the one obtained by manual

annotation, albeit right-shifted by approximately 1 nm. For test image 2, containing bimodally distributed nanocrystal sizes, PEBBLES failed to detect the larger nanocrystals. This resulted in 95 % false negatives and an error of 151 % for the mean absolute deviation. For test image 3 PEBBLES failed to detect the smaller nanocrystals, also resulting in 95 % false negatives.

The NLoG method performed best with regards to accuracy of mean nanocrystal size and mean absolute deviation for all three test images and for test image 2 it accurately captured the histogram shape of the nanocrystal size distribution. It did not perform as well for test image 1, however. Although it detected a number of the small nanocrystals, it overestimated their sizes. This is caused by the input parameters used in the NLoG method and the difference in pixel size between the validation image and this specific test image. The relevant NLoG input parameter for this case is the smallest value in the sampled scale space. Together with the NMS threshold this parameter distinguishes the smallest nanocrystals from background noise. A too small value would cause the method to falsely detect noise as nanocrystals, but a too large value will cause the method to fail to detect the smallest nanocrystals, or still detect them at a greater scale. The latter happened in test image 1. The NLoG method was optimized for an image at relatively high magnification, so the nanocrystals in that image are of relatively large sizes in pixels. The smallest value in the sampled scale space could therefore be relatively large, minimizing false positives. Applying these parameters on test image 1, with lower magnification and relatively small nanocrystals in pixels, resulted in many of the smallest nanocrystals being detected at the smallest scale in the sampled scale space. However, although the NLoG method performed worse in test image 1, its results were comparable or better than the other automated methods used. For test image 1 the magnification is so low that the smallest nanocrystals are of similar size as noise fluctuations. In that case the NLoG method does not perform very well. However, such a low magnification makes all methods of nanocrystal detection difficult, including manual annotation. For test image 3, the NLoG method captured the histogram shape of the nanocrystal size distribution reasonably well, although it falsely detected too many smaller-sized nanocrystals. Note that because of the greater sample thickness used for this image, its contrast is considerably worse and there is an increased probability of overlapping nanocrystals. This makes the analysis significantly harder, not only for the automated routines, but also for manual annotation. Since manual annotation is used as a benchmark for the routine's performance, uncertainty in the manual annotation's results, leads to greater uncertainty in the performance of the evaluated routines.

For the test image set we find that a greater TEM image magnification leads to increased accuracy for the NLoG method. However, this effect is expected to be limited, since the number of nanocrystals captured is lower for greater magnifications, increasing the statistical error of the obtained size distribution. Furthermore, the contrast generated in HR-TEM images is different from BF-TEM images. The contrast due to lattice fringes will dominate in HR-TEM images in-

stead of the high-contrast black nanocrystals seen in BF-TEM images, possibly decreasing the effectiveness of the NLoG method. This may imply that there is an optimal magnification range for TEM images, in order to achieve the highest possible accuracy for the NLoG method. However, this is beyond the scope of this article.

Also note that although all TEM images were taken from the same sample, the obtained size distributions differ significantly. Since we have no reason to expect sample inhomogeneity, this difference is attributed to the different magnifications used during imaging and the related pixel sizes. Test image 1, taken at 22 500× magnification, shows a unimodal size distribution. The pixel size for this image is 0.576 nm, which means that the smallest nanocrystals, with diameters of 1 to 2 nm will span only 2 to 4 pixels. Such small features are easily lost in background noise. This implies that an image with such a magnification is ill-suited to measure the smallest of the nanocrystals, leading to a distortion of the obtained size distribution. In contrast, test image 2 shows a bimodal nanocrystal size distribution. This image was taken at a greater magnification of 63 000× and has a pixel size of 0.207 nm. This means that nanocrystals with 1 to 2 nm diameter show up as features of 5 to 10 pixels, which makes them much easier to distinguish from background noise. Since the magnification of test image 3 is greater than that of test image 1, its size distribution should be more accurate. However, the contrast and background inhomogeneity is significantly worse, making it harder to correctly distinguish nanocrystals from background noise and possibly distorting the obtained size distribution with false positives and false negatives.

We stress that it is very difficult, if not impossible to obtain the true size distribution from TEM images. Slicing nanocrystals alters the apparent size distribution and it is very hard to objectively detect and correctly measure all nanocrystals in an image. Manual annotation leads to a user bias and is time-consuming. The NLoG method leads to comparable results and takes significantly less time. For test image 2 we analytically corrected the nanocrystal size distribution for nanocrystal slicing. We find that the error in mean absolute deviation by the NLoG method is larger than the error induced by slicing, but the error for the mean size is smaller for the NLoG method than induced by slicing.

The NLoG method was optimized and tested for BF-TEM images, but can also be optimized for dark-field or high-resolution TEM images.

4.6 Conclusions

We have demonstrated the NLoG method to quickly detect and measure nanocrystals in a TEM image to obtain the nanocrystal size distribution with minimum user input. The method uses a convolution of the TEM image with NLoG filters. Furthermore, we show that the input parameters for this method can be optimized for one image and can then be applied to similar images with comparable or smaller pixel sizes, leading to accurate results. We compared the accuracy and

speed of this method with other methods used in literature and the proposed method performed comparable or better in the image test set. Furthermore, we have developed an analytical correction for the effect of slicing nanocrystals during TEM sample preparation on the apparent nanocrystal size distribution. We derived an equation for the apparent nanocrystal size for a given real nanocrystal size. Assuming a certain nanocrystal distribution shape, this equation can be used to fit a real nanocrystal size distribution from a measured apparent size distribution.

5

Obtaining the nanocrystal density of states

This chapter is based on the following publication:

M. van Sebille, R. A. Vasudevan, R. J. Lancee, R. A. C. M. M. van Swaaij, M. Zeman, *Optical characterization and density of states determination of silicon nanocrystals embedded in amorphous silicon based matrix*, Journal of Physics D: Applied Physics **48**, 325302 (2015).

Abstract

We present a non-destructive measurement and simple analysis method for obtaining the absorption coefficient of silicon nanocrystals embedded in an amorphous matrix. This method enables us to pinpoint the contribution of silicon nanocrystals to the absorption spectrum of nanocrystal containing films. The density of states (DOS) of the amorphous matrix is modeled using the standard model for amorphous silicon while the nanocrystals are modeled using one Gaussian distribution for the occupied states and one for the unoccupied states. For laser annealed a-$Si_{0.66}O_{0.34}$:H films, our analysis shows a reduction of the nanocrystal band gap from approximately 2.34 to 2.08 eV indicating larger mean nanocrystal size for increasing annealing laser fluences, accompanied by a reduction in nanocrystal DOS distribution width from 0.28 to 0.26 eV, indicating a narrower size distribution.

5.1 Introduction

As explained in section 1.4.3, a method to obtain the nanocrystal absorption properties and their DOS from absorption spectra has been lacking. In this chapter we show how to obtain the absorption parameters of embedded nanocrystals directly using a non-destructive measurement. We studied the optical properties of embedded silicon nanocrystals and pinpointed the nanocrystal contribution to the absorption spectrum of nanocrystal containing films. Furthermore, we propose a model to extract the optical properties and the DOS of both the nanocrystals and their embedding matrix. The model is demonstrated on laser-annealed amorphous silicon-rich silicon oxide (a-SiO_x) films.

This chapter is organized as follows. First, we provide the experimental details in section 5.2. The method to determine the relative hydrogen content is also discussed in detail in this section. In section 5.3 we describe the model used to obtain DOS parameters from absorption measurements. In particular we will describe the model for the DOS of a-SiO_x and the DOS of nanocrystals in detail. In section 5.4 the results of our measurements on the series of laser annealed a-SiO_x samples, used to demonstrate the model, is shown. Finally, we provide a discussion on the results obtained in section 5.5, by applying our method on the sample series and we postulate a nanocrystal growth model for laser annealed a-SiO_x films.

5.2 Experimental details

We deposited 90-nm thick a-$Si_{0.66}O_{0.34}$:H on Quartz Unlimited electric fused quartz substrates using the PECVD setup described in section 2.1.1. The following deposition parameters were used: a power density of 0.139 W cm^{-2}, a deposition pressure of 1.4 mbar, a substrate temperature of 180 °C, and SiH_4 and CO_2 flows of 8 and 48 sccm, respectively. The atomic composition of the deposited film was determined using x-ray photoelectron spectroscopy measurements, using a Thermo Scientific K-Alpha setup described in section 2.2.1. The film surface was etched with an ion gun prior to measurements to remove surface contamination. Laser annealing was performed at 10^{-6} mbar with 25 overlapping pulses using a Lambda Physics XeCl excimer laser with a wavelength of 308 nm and pulse duration of 25 ns. A laser fluence series of 60 to 240 mJ cm^{-2} with 20 mJ cm^{-2} intervals was studied.

Raman spectra were measured to determine the crystallinity. The method and setup used are described in section 2.2.3. Raman results were averaged over 5 measurements per sample to account for sample inhomogeneity. Raman spectroscopy was also used to determine the *relative* hydrogen concentration in the films. Typically, Fourier transform infrared spectroscopy (FTIR) is used to determine the hydrogen concentration for thin film amorphous silicon [84] and silicon alloys [85]. For FTIR, however, the thickness of the film should be large

enough for notable absorbance and the substrate should be transparent in the infrared range [86]. Therefore, c-Si wafers are often used as substrates, while for PDS measurements, the substrate should also be transparent in the visible part of the spectrum. Laser annealing of silicon-based alloy films on different substrates would result in significantly different samples, caused by a difference in heat dissipation due to the different heat transfer coefficients. We therefore chose to use only quartz substrates, which are not transparent in the entire infrared range. Therefore we used Raman to determine the hydrogen concentration in our silicon alloy layers, using a similar method demonstrated before for hydrogenated amorphous silicon [86]. The relative hydrogen content R_{H} was determined as the ratio between the sum of integrated Si–H stretching modes and the sum of integrated TO phonon modes of a-SiO_x $I_{\mathrm{TO,a-SiO}_x}$ at 485 cm^{-1} and c-Si $I_{\mathrm{TO,c-Si}}$ around 520 cm^{-1}

$$R_{\mathrm{H}} = \frac{I_{\mathrm{LSM}} + I_{\mathrm{HSM}}}{0.8 I_{\mathrm{TO,a-SiO}_x} + I_{\mathrm{TO,c-Si}}}, \tag{5.1}$$

where I_{LSM} and I_{HSM} are the integrated Si–H low stretching mode and high stretching mode, respectively, both in the range of 2000 to 2300 cm^{-1} [87, 88]. We account for the difference in cross-section of the two phonon excitations by using a factor 0.8, which is a typically used value [89, 90]. Since the Raman capture cross-section of the two Si–H stretching modes are different for a-Si:H [91], we assume this is also the case for a-SiO_x:H. However, as the ratio R^*, defined as $I_{\mathrm{HSM}}/(I_{\mathrm{HSM}} + I_{\mathrm{LSM}})$ [92], is constant throughout our sample series (not shown here), we disregard differences in capture cross-sections for the hydrogen modes. For Si–H stretching modes, the baseline was fitted with a second order polynomial in the range 1900 to 2400 cm^{-1}, excluding 2000 to 2350 cm^{-1} and was subsequently removed from the spectra.

The thickness and complex refractive index were obtained from spectroscopic ellipsometry (SE) measurements, using the setup described in section 2.2.2. Although SE can also be used to measure the absorption coefficient of films, it is less sensitive in the near-infrared. In this part of the spectrum, absorption is related to optical transitions to and from sub-band gap states [65]. In section 5.3, we describe an optical model, which will be used to fit the absorption coefficient to a DOS. In order to do this accurately for a DOS in a wide electron energy range, including states within the band gap, we need accurate absorption measurements over a wide photon energy range, including the low photon energy range.

Absorption spectra were obtained using an absolute PDS setup, described in section 2.2.4. Measurements were carried out in the range 1 to 3.5 eV (1240 to 355 nm) and data with unstable phase were discarded. The absorption coefficient was calculated using the Ritter-Weisser formula [93].

5.3 Optical model

In this section we will present the model for obtaining the optical absorption of an amorphous silicon (alloy) with silicon nanocrystals. With this model we can extract the optical properties and the DOS of both the nanocrystals and their embedding matrix. The absorption coefficient $\alpha(E)$ can be calculated from the DOS using the following equation [94]

$$\alpha(E) = \frac{C}{E}\int g(\epsilon)\, f(\epsilon)\, g(\epsilon + E)\,[1 - f(\epsilon + E)]\,\mathrm{d}\epsilon, \tag{5.2}$$

where E and ϵ are photon and electron energy respectively, f is the Fermi-Dirac distribution, g is the DOS distribution, and C is a constant that is weakly photon energy dependent and includes the photon energy dependence of the refractive index and the dipole matrix element with value of $3.34 \times 10^{-38}\,\mathrm{cm^5eV^2}$ [94]. Since the nanocrystals and a-SiO_x matrix are geometrically separated, electron transitions caused by photoexcitation between the two are considered impossible. Hence, we model the matrix and nanocrystal DOS contributions to the absorption coefficient separately.

The DOS of a-SiO_x matrix is modeled using the standard model for amorphous silicon [95], shown for as-deposited a-$Si_{0.66}O_{0.34}$:H in figure 5.1. The conduction band $N_{\mathrm{CB+CBT}}$ is composed of extended states N_{CB} and tail states N_{CBT}, which are described by

$$N_{\mathrm{CB}}(\epsilon) = N^0\sqrt{(\epsilon - \epsilon_{\mathrm{C}})} \tag{5.3}$$

$$N_{\mathrm{CBT}}(\epsilon) = N_{\mathrm{C}}^{\mathrm{tail}}\exp\left[-\left(\frac{\epsilon_{\mathrm{C}}^{\mathrm{tail}} - \epsilon}{\epsilon_{\mathrm{C0}}^{\mathrm{tail}}}\right)\right], \tag{5.4}$$

where N^0 is the parameter describing the parabolic distribution of states in the extended states of the conduction and valence bands. The extended and tail states are connected by imposing continuity of both the DOS (5.5) and its energy derivative (5.6) at the connecting point $\epsilon_{\mathrm{C}}^{\mathrm{tail}}$.

$$N_{\mathrm{CB}}\left(\epsilon_{\mathrm{C}}^{\mathrm{tail}}\right) = N_{\mathrm{CBT}}\left(\epsilon_{\mathrm{C}}^{\mathrm{tail}}\right) \tag{5.5}$$

$$\frac{\mathrm{d}N_{\mathrm{CB}}\left(\epsilon_{\mathrm{C}}^{\mathrm{tail}}\right)}{\mathrm{d}\epsilon} = \frac{\mathrm{d}N_{\mathrm{CBT}}\left(\epsilon_{\mathrm{C}}^{\mathrm{tail}}\right)}{\mathrm{d}\epsilon} \tag{5.6}$$

Solving these equations lead to an expression of ϵ_C, which is used in equation (5.3)

$$\epsilon_{\mathrm{C}} = \epsilon_{\mathrm{C}}^{\mathrm{tail}} + \tfrac{1}{2}\epsilon_{\mathrm{C0}}^{\mathrm{tail}}. \tag{5.7}$$

Likewise, the DOS for the valence band $N_{\mathrm{VB+VBT}}$ is defined as follows.

$$N_{\mathrm{VB}}(\epsilon) = N^0\sqrt{(\epsilon - \epsilon_{\mathrm{V}})} \tag{5.8}$$

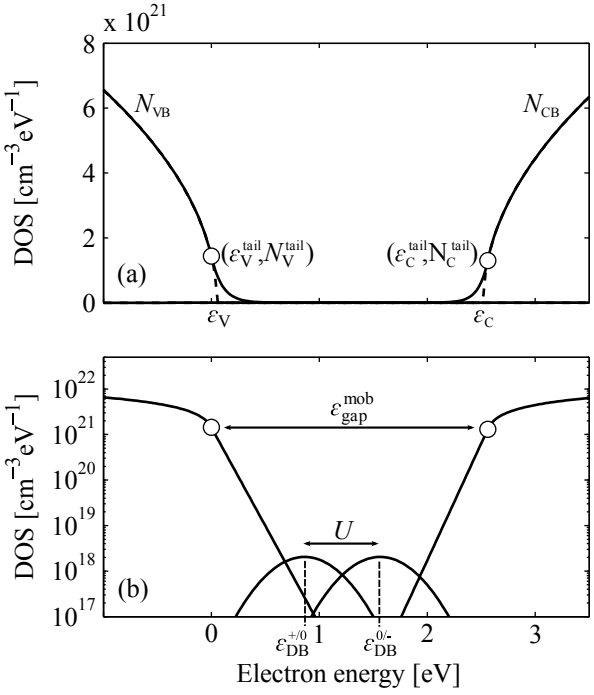

Figure 5.1: Standard model of single electron DOS for a-$Si_{0.66}O_{0.34}$:H shown in linear scale (a) and logarithmic scale (b)

$$N_{\mathrm{VBT}}(\epsilon) = N_{\mathbf{V}}^{\mathrm{tail}} \exp\left[-\left(\frac{\epsilon_{\mathrm{V}}^{\mathrm{tail}} - \epsilon}{\epsilon_{\mathrm{V0}}^{\mathrm{tail}}}\right)\right] \tag{5.9}$$

$$\epsilon_{\mathrm{V}} = \epsilon_{\mathrm{V}}^{\mathrm{tail}} + \tfrac{1}{2}\epsilon_{\mathrm{V0}}^{\mathrm{tail}} \tag{5.10}$$

We assume that the parabolic shape of the extended states is equal for both the conduction and valence band, described by N^0 [96]. $\epsilon_{\mathrm{C0}}^{\mathrm{tail}}$ and $\epsilon_{\mathrm{V0}}^{\mathrm{tail}}$ describe the exponential slope of the conduction band and valence band, respectively, and $\left(\epsilon_{\mathrm{C}}^{\mathrm{tail}}, N_{\mathrm{C}}^{\mathrm{tail}}\right)$ and $\left(\epsilon_{\mathrm{V}}^{\mathrm{tail}}, N_{\mathrm{V}}^{\mathrm{tail}}\right)$ are the connection points of the tail states to extended states of the conduction and valence band, respectively. We set $\epsilon_{\mathrm{C}}^{\mathrm{tail}} = \epsilon_{\mathrm{V}}^{\mathrm{tail}} + \epsilon_{\mathrm{gap}}^{\mathrm{mob}}$, where $\epsilon_{\mathrm{gap}}^{\mathrm{mob}}$ is the mobility gap.

Defects are modeled with two Gaussian distributions using the following set of equations

$$N_{\mathrm{DB}}^{+/0}(\epsilon) = \frac{N_{\mathrm{DB}}^{\mathrm{tot}}}{\sigma_{\mathrm{DB}}\sqrt{2\pi}} \exp\left[\frac{\left(\epsilon - \epsilon_{\mathrm{DB}}^{+/0}\right)^2}{2{\sigma_{\mathrm{DB}}}^2}\right] \tag{5.11}$$

$$N_{\mathrm{DB}}^{0/-}(\epsilon) = \frac{N_{\mathrm{DB}}^{\mathrm{tot}}}{\sigma_{\mathrm{DB}}\sqrt{2\pi}} \exp\left[\frac{\left(\epsilon - \epsilon_{\mathrm{DB}}^{0/-}\right)^2}{2{\sigma_{\mathrm{DB}}}^2}\right] \tag{5.12}$$

$$N_{\mathrm{DB}}^{0/-}(\epsilon) = N_{\mathrm{DB}}^{+/0}(\epsilon + U) \tag{5.13}$$

$$\epsilon_{\mathrm{DB}}^{0/-} = \epsilon_{\mathrm{DB}}^{+/0} + U \tag{5.14}$$

$$\epsilon_{\mathrm{DB}} = \epsilon_{\mathrm{DB}}^{+/0} + \tfrac{1}{2}U = \epsilon_{\mathrm{DB}}^{0/-} - \tfrac{1}{2}U, \tag{5.15}$$

where $\epsilon_{\mathrm{DB}}^{0/-}$ and $\epsilon_{\mathrm{DB}}^{+/0}$ are the energy levels of the acceptor-like states $N_{\mathrm{DB}}^{0/-}$ and donor-like states $N_{\mathrm{DB}}^{+/0}$, respectively, $N_{\mathrm{DB}}^{\mathrm{tot}}$ is the total defect density, σ_{DB} is the distribution width and U is the correlation energy.

Since the material is intrinsic, we can state that the hole density in the valence band is equal to the electron density in the conduction band, so

$$\int g_{\mathrm{CB}}(\epsilon)\, f(\epsilon)\, \mathrm{d}\epsilon = \int g_{\mathrm{VB}}(\epsilon)\,(1 - f(\epsilon))\, \mathrm{d}\epsilon. \tag{5.16}$$

Solving this equation for a given DOS fixes the Fermi level.

For embedded nanocrystals, both volume and interface states contribute to the total nanocrystal DOS. To determine their relative contributions to the optical properties, the ratio Γ_{states} between the volume state density N_{vol} over interface state density N_{int} can be approximated using the following equation

$$\Gamma_{\mathrm{states}} = \frac{N_{\mathrm{vol}}}{N_{\mathrm{int}}} = \frac{\frac{4}{3}\pi r^3 \rho_{\mathrm{vol}} z_{\mathrm{vol}} V^{-1}}{4\pi r^2 \rho_{\mathrm{int}} z_{\mathrm{int}} V^{-1}} = \frac{r\rho_{\mathrm{vol}} z_{\mathrm{vol}}}{3\rho_{\mathrm{int}} z_{\mathrm{int}}}, \tag{5.17}$$

where r is the nanocrystal radius, ρ_{vol} and ρ_{int} are the atomic and the surface atomic densities, respectively, z_{vol} is the number of valence electrons per atom, z_{int} is the number of non-backbonded bonds per nanocrystal surface atom, and V is the measured sample volume. For c-Si, ρ_{vol} is $5.02 \times 10^{22}\,\mathrm{cm}^{-3}$ [73], and for ρ_{int} the average of the density of surface atoms for the three principle crystals planes, (100), (110) and (111), is taken, which is $1 \times 10^{15}\,\mathrm{cm}^{-2}$ [73]. z_{vol} is 4 for silicon and for z_{int} the average of the three principle crystals planes is taken, which is $1\frac{1}{3}$ [97]. Using equation (5.17), the ratio of nanocrystal volume state density over interface state density is 7.5 and 12.6 for nanocrystals with 1.5 nm and 2.5 nm radii, respectively. So, for these typical silicon nanocrystal sizes [38, 41, 98], the density of volume states is approximately an order of magnitude larger than the density of interface states. Assuming similar absorption cross-section for these states, we conclude that volume states dominate the optical properties of embedded nanocrystals and we can disregard interface states.

For nanocrystals, we propose a DOS model with two Gaussian distributions, one for highest occupied states $N_{\mathrm{NC}}^{\mathrm{HOS}}$ and one for lowest unoccupied states $N_{\mathrm{NC}}^{\mathrm{LUS}}$

$$N_{\mathrm{NC}}(\epsilon) = N_{\mathrm{NC}}^{\mathrm{HOS}} + N_{\mathrm{NC}}^{\mathrm{LUS}} \tag{5.18}$$

$$N_{\mathrm{NC}}^{\mathrm{HOS}} = \frac{N_{\mathrm{NC}}^{0}}{\sigma_{\mathrm{NC}}\sqrt{2\pi}} \exp\left[-\frac{\left(\epsilon - \mu_{\mathrm{NC}}^{\mathrm{HOS}}\right)^{2}}{2{\sigma_{\mathrm{NC}}}^{2}}\right] \tag{5.19}$$

$$N_{\mathrm{NC}}^{\mathrm{LUS}} = \frac{N_{\mathrm{NC}}^{0}}{\sigma_{\mathrm{NC}}\sqrt{2\pi}} \exp\left[-\frac{\left(\epsilon - \mu_{\mathrm{NC}}^{\mathrm{LUS}}\right)^{2}}{2{\sigma_{\mathrm{NC}}}^{2}}\right] \tag{5.20}$$

$$\mu_{\mathrm{NC}}^{\mathrm{HOS}} = \epsilon_{\mathrm{F}} - \tfrac{1}{2}\epsilon_{\mathrm{gap}}^{\mathrm{NC}} \tag{5.21}$$

$$\mu_{\mathrm{NC}}^{\mathrm{LUS}} = \epsilon_{\mathrm{F}} + \tfrac{1}{2}\epsilon_{\mathrm{gap}}^{\mathrm{NC}}, \tag{5.22}$$

where N_{NC}^{0} and σ_{NC} are the amplitude and width of the two Gaussian distributions describing the nanocrystal DOS. $\mu_{\mathrm{NC}}^{\mathrm{HOS}}$ and $\mu_{\mathrm{NC}}^{\mathrm{LUS}}$ are the mean of the highest occupied and lowest unoccupied states, respectively, and ϵ_F is the Fermi level. We define the nanocrystal band gap $\epsilon_{\mathrm{NC}}^{\mathrm{gap}}$ as follows

$$\epsilon_{\mathrm{NC}}^{\mathrm{gap}} = \mu_{\mathrm{NC}}^{\mathrm{LUS}} - \mu_{\mathrm{NC}}^{\mathrm{HOS}} - 2\sigma_{\mathrm{NC}}. \tag{5.23}$$

Note that this DOS describes all nanocrystal states in the measured sample volume, containing multiple nanocrystals of varying sizes. Very small silicon nanocrystals in a-SiO_x matrix have discrete, quantized energy states, according to density functional theory calculations [17, 99]. However, these calculations are performed on crystals of up to a few hundred atoms, while nanocrystals of several nanometres contain typically hundreds to thousands of atoms. This means that for bigger nanocrystals, the quantification of energy levels decreases and the nanocrystal's energy states can be more accurately described by semi-continuous energy bands. Furthermore, we probe a collection of nanocrystals, of which the sizes are typically distributed normally [41, 98] or log-normally [38, 42]. The result is that we measure a nanocrystal size distribution with semi-quantized energy states. As we have no means to distinguish between these two effects, we assume that the collection of semi-quantized nanocrystals can be modeled by the two Gaussian distributions, described in equations described above.

The energy difference between the peak position of the two Gaussian distributions is a measure of the average NC band gap, the width of the distributions is a measure of the nanocrystal size uniformity [100], and the integral of one of these two Gaussian distributions is a measure of the total density of nanocrystal states. We assume these distributions are centered symmetrically around the Fermi level, since the surrounding amorphous matrix imposes its occupation on the nanocrystals. Using this model, the absorption spectrum can be fit, by changing the DOS parameters of the a-SiO_x and NCs. We used non-linear regression with a proportional error model to ensure a good fit at both low and high values of the logarithmically scaled absorption coefficient. Figure 5.2 shows PDS data measured on a sample laser annealed at 200 mJ cm^{-2}, together with the contribution of the host material and the nanocrystals to the spectrum as obtained by applying this method. The associated DOS for the amorphous matrix and the nanocrystals for this sample is shown in figure 5.3.

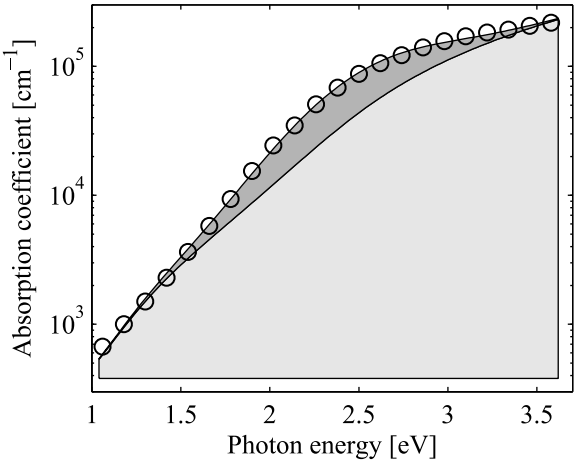

Figure 5.2: Resulting fit of PDS measurement for sample laser annealed at 200 mJ cm^{-2}. The dark and light grey areas are the contribution from the amorphous matrix and the nanocrystals, respectively. The circles show the PDS data measured at photon energy interval of 1 to 3.6 eV. Some data points (∘) have been omitted for presentation purposes only; the actual data values are more closely spaced.

5.4 Results

Figure 5.4 shows Raman measurements on as-deposited and laser annealed samples, scaled to their respective amorphous silicon transverse optical (TO) modes at 480 cm^{-2}. For as-deposited a-$Si_{0.66}O_{0.34}$:H, the Si–H stretching modes at 2100 cm^{-1} are clearly visible, as well as the amorphous phonon modes in the range 100 to 550 cm^{-1}. Upon laser annealing, the Si–H stretching modes decrease in amplitude. At a laser fluence of 140 mJ cm^{-2} crystallization of silicon occurs as indicated by the appearance of the sharp c-Si TO mode at 520 cm^{-2} [62]. We will refer to this laser fluence as the crystallization threshold. Additionally, a smaller peak appears at 965 cm^{-1}, which is the second order c-Si TO mode [101]. The Si–H stretching mode has disappeared for laser fluences larger than the crystallization threshold.

PDS measurements are shown in figure 5.5. The absorption spectrum of as-deposited a-$Si_{0.66}O_{0.34}$:H is typical for hydrogenated amorphous silicon (alloys), showing sub-band gap absorption related to defects, a typical exponentially shaped Urbach tail [102] and super-band gap absorption. Upon laser annealing with a laser fluence of 60 mJ cm^{-2}, the sub-band gap absorption increases significantly and the Urbach tail broadens. For increasing laser fluence, the sub-band gap absorption slightly increases, but the shape of the absorption spectrum does not change significantly up to the crystallization threshold. For partially crystallized samples, annealed with laser fluences greater than the crystallization threshold,

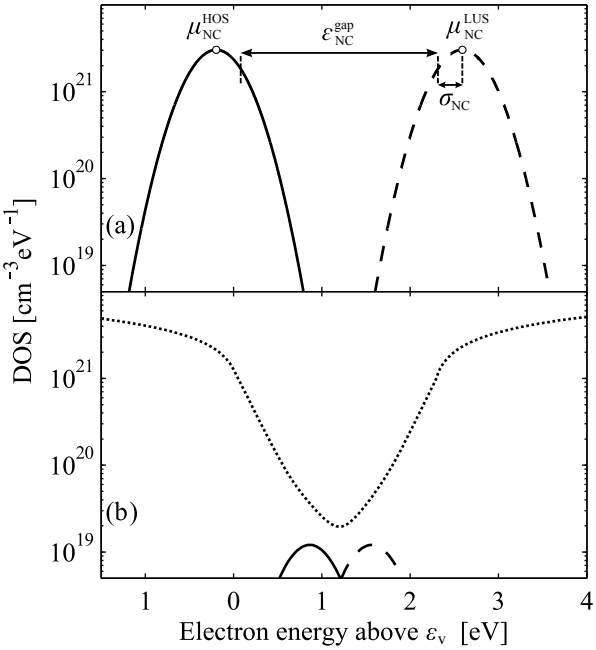

Figure 5.3: For an a-SiO_x film annealed with a laser fluence of 200 mJ cm^{-2}, the single electron DOS is shown of (a) nanocrystals, with solid and dashed line displaying the highest occupied and the lowest unoccupied states, respectively. (b) The single electron DOS of a-SiO_x matrix with the dotted line showing a-SiO_x DOS and solid and dashed lines showing donor-like and acceptor-like defect states, respectively.

we observe an additional absorption feature in the range from 1.6 to 3 eV, which we attribute to nanocrystal absorption.

Figure 5.6a shows the crystallinity as a function of laser fluence. Crystallization starts for a laser fluence in excess of 120 mJ cm^{-2} and the crystallinity increases with increasing laser fluence, before levelling off at 160 mJ cm^{-2}. Figure 5.6b shows the relative hydrogen content R_H. From the as-deposited sample, this ratio decreases rapidly upon laser annealing. R_H is negligible for 140 mJ cm^{-2} and remains so for increasing laser fluences. The sub-band gap absorption at a photon energy of 1.5 eV is also shown in figure 5.6b and shows a similar, but inverse trend. The sub-band gap absorption at 1.5 eV is low for the as-deposited sample and increases rapidly upon laser annealing. Similar to the relative hydrogen content, the sub-band gap absorption stabilizes for increasing laser fluences.

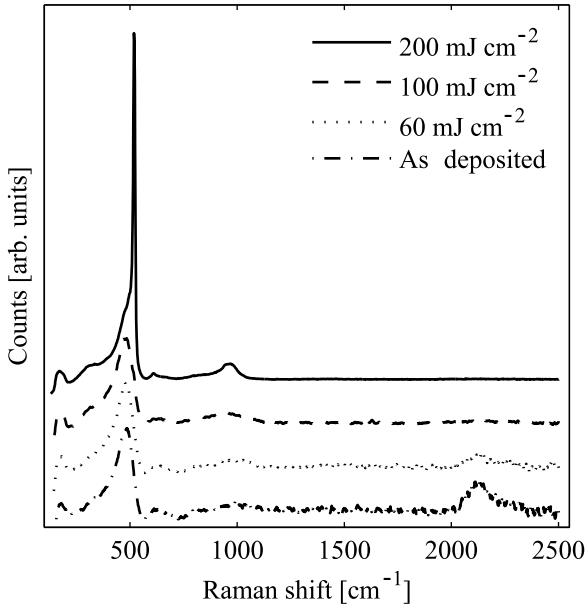

Figure 5.4: Raman measurements of as-deposited and laser annealed samples

5.5 Discussion

From Raman and PDS measurements, we can distinguish two regimes for laser annealing. The first regime is at low laser fluences, below the crystallization threshold. The intensity of Si–H stretching modes decreases and disappears for increasing laser fluences, as shown in figure 5.6b. Furthermore, PDS measurements show an increase in sub-band gap absorption for this regime, also shown in figure 5.6b. These results indicate that hydrogen effusion occurs at all laser fluences, creating optically active dangling bonds. Furthermore, we observe that these dangling bonds are already created at low laser fluences. The second regime is at higher laser fluences, above the crystallization threshold. In this regime, crystallization occurs and the crystallinity increases with increasing laser fluence. Increasing the laser fluence beyond 140 mJ cm^{-2} does not significantly change the relative hydrogen content, nor the sub-band gap absorption. This indicates that the majority of sub-band gap absorption is directly related to dangling bonds caused by hydrogen effusion and that these changes to the amorphous matrix occur before crystallization. From these results we conclude that little changes occur in the a-SiO_x matrix in the second regime.

Considering these results, we use the following approach and assumptions to fit our data, using the model described above. For the fitting routine we start with fitting as-deposited a-$Si_{0.66}O_{0.34}$:H, using N^0, ϵ_{V0}^{tail}, ϵ_{C0}^{tail}, ϵ_{gap}^{mob}, ϵ_{DB}, U, σ_{DB} and N_{DB}^{tot}

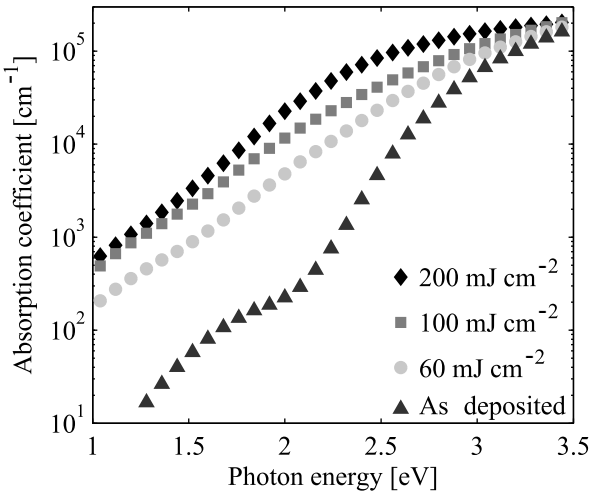

Figure 5.5: PDS measurements for as-deposited and laser annealed samples. Some data points have been omitted for presentation purposes only; the actual data values are more closely spaced.

as free fit parameters. Subsequently, the laser annealed samples were fitted, keeping ϵ_{DB}, U and σ_{DB} constant. For the partially crystallized samples, we fix more parameters. Our results indicate that from the crystallization onset, the sub-band gap absorption and the relative hydrogen content do not change significantly, so we also keep the amorphous matrix related parameters $\epsilon_{\mathrm{V0}}^{\mathrm{tail}}$, $\epsilon_{\mathrm{C0}}^{\mathrm{tail}}$, $\epsilon_{\mathrm{gap}}^{\mathrm{mob}}$, and defect related parameters ϵ_{DB}, U and σ_{DB} fixed. We allow N^0 to change, since crystallization leads to a decrease in the atomic density of atoms in the amorphous phase, causing a decrease in amorphous silicon DOS. The total defect density $N_{\mathrm{DB}}^{\mathrm{tot}}$ can also change, since it has been reported that increased annealing temperatures can actually lead to a decrease in defect density in the material, as recombination of dangling bonds during thermally activated restructuring of the material takes place [50]. However, for our samples such a trend was not clearly discerned.

As shown in figure 5.7a, we observe that the integrated unoccupied nanocrystal DOS I_{NC} follows the same trend as the crystallinity: both increase with increasing laser fluence. This is expected, since a higher crystallinity reflects a larger nanocrystal state density within the measured sample volume. This is either caused by an increased density of nanocrystals, an increase in average nanocrystal size, or both. The crystallinity and I_{NC} both level off around 160 mJ cm^{-2}. We also find that the nanocrystal band gap $\epsilon_{\mathrm{NC}}^{\mathrm{gap}}$, defined in equation (5.23), decreases from approximately 2.34 to 2.08 eV with increasing laser fluence, as shown in figure 5.7b. These values seem high compared to optical band gap values typically reported from photoluminescence measurements [11, 18–20], but note that these two band gap values are defined differently. From the DOS, we cannot pre-

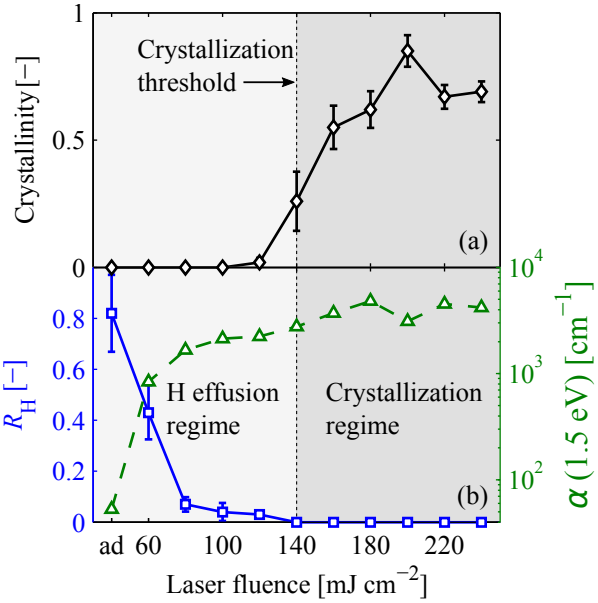

Figure 5.6: (a) Crystallinity for samples laser annealed with varying laser fluences. The as-deposited sample is depicted as 'ad' in the x-axis. (b) Relative hydrogen content (blue solid line, left axis) and sub-band gap absorption from PDS measurements at 1.5 eV (green dashed line, right axis).

dict exactly to which state densities hot carriers will thermalize before radiative recombination. Still, this energy range corresponds well with calculations performed using density functional theory [17, 105]. However, as noted before, it is impossible to relate the nanocrystal band gap ϵ_{NC}^{gap} directly to a nanocrystal size, since the band gap is also affected by other factors, such as stress imposed by the embedding matrix [15] and surface passivation [16, 17]. Furthermore, we observe that the nanocrystal DOS distribution width σ_{NC} decreases from 0.28 eV to 0.26 eV, as shown in figure 5.7c. The smaller nanocrystal distribution width for the sample annealed at 220 mJ cm^{-2} is an outlier.

From these results we can construct a nanocrystal growth model for laser annealed nanocrystals. Since the nanocrystal band gap is inversely related to their size, we conclude that small nanocrystals are formed at the crystallization onset and grow bigger at increasing laser fluence. From the nanocrystal DOS distribution width we can deduce that at the crystallization onset, the nanocrystal size uniformity increases for increasing laser fluence.

5.6 Conclusions

A non-destructive measurement and simple analysis method for obtaining the absorption coefficient of silicon nanocrystals embedded in an amorphous matrix is presented. Furthermore, we proposed a model to extract the optical properties and the DOS of both the nanocrystals and their embedding matrix. Using this model, we propose a growth model for embedded nanocrystals created by laser annealing silicon-rich a-SiO_x. We find that an increasing laser fluence leads to a reduction of the nanocrystal band gap and a reduction in nanocrystal DOS distribution width, indicating larger mean nanocrystal sizes and narrower nanocrystal size distribution for increasing laser fluences.

For laser annealed a-$Si_{0.66}O_{0.34}$:H films, we observe hydrogen effusion and an increase in sub-band gap absorption at low laser fluences. For laser fluences in excess of 120 mJ cm^{-2}, crystallization of silicon occurs and the crystallinity increases with increasing laser fluence. For laser fluences larger than the crystallization threshold of 140 mJ cm^{-2}, changes to the sub-band gap absorption and relative hydrogen content are insignificant. From these results we conclude that defect creation occurs predominantly at laser fluences below the crystallization threshold.

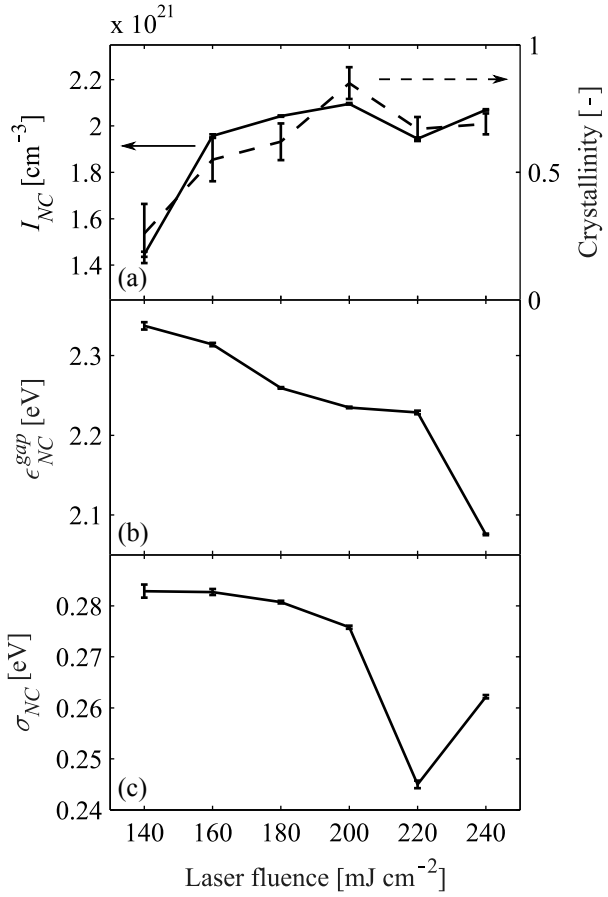

Figure 5.7: (a) Integrated unoccupied nanocrystal DOS I_{NC} with 95 % confidence intervals (solid line, left axis) and crystallinity from Raman measurements (dashed line, right axis) for varying laser fluences, (b) nanocrystal band gap ϵ_{NC} with 95 % confidence intervals for varying laser fluences, (c) nanocrystal DOS distribution width σ_{NC} with 95 % confidence intervals for varying laser fluences

6

Shrinking of silicon nanocrystals during annealing in forming gas atmosphere

This chapter is based on the following publication:

M. van Sebille, A. Fusi, L. Xie, H. Ali, R. A. C. M. M. van Swaaij, K. Leifer and M. Zeman, *Shrinking of silicon nanocrystals embedded in amorphous silicon oxide matrix during rapid thermal annealing in forming gas atmosphere*, Nanotechnology **27**, 365601 (2016).

Abstract

We report the effect of hydrogen on the crystallization process of silicon nanocrystals embedded in a silicon oxide matrix. We show that hydrogen gas during annealing leads to a lower sub-band gap absorption, indicating passivation of defects created during annealing. Samples annealed in pure nitrogen show expected trends according to crystallization theory. Samples annealed in forming gas, however, deviate from this trend. Their crystallinity decreases for increased annealing time. Furthermore, we observe a decrease in the mean nanocrystal size and the size distribution broadens, indicating that hydrogen causes a size reduction of the silicon nanocrystals.

6.1 Introduction

As explained in section 1.3.2, hydrogen effusion occurs at lower temperatures than phase separation and crystallization, so this cannot be avoided during the necessary high-temperature annealing step, leading to an increased defect density. Reincorporation of hydrogen into the material is considered to be an effective method to reduce the defect density [52, 53]. One option is to combine annealing and hydrogen passivation in a single processing step, by annealing in a H_2 containing atmosphere. However, a detailed study of the effect of hydrogen on the nanocrystal growth during annealing has been lacking.

In this chapter we report the effects of a hydrogen containing atmosphere on the nanocrystal incubation time, growth and stabilization using Raman spectroscopy, photothermal deflection spectroscopy (PDS) and transmission electron microscopy (TEM). We show that samples annealed in pure nitrogen show expected trends according to crystallization theory, including an incubation time and subsequent increase and stabilization of crystallinity. Samples annealed in forming gas (90 % N_2 + 10 % H_2), however, deviate from this expected trend. After an incubation time and increase in crystallinity, the crystallinity decreases for increased annealing time. Furthermore, PDS measurements show that the mean nanocrystal size decreases and the size distribution broadens, indicating that hydrogen diffuses into the material and causes a size reduction of the silicon nanocrystals.

This chapter is organized as follows. First, we provide the experimental details in section 6.2. The methods to determine the crystallinity and nanocrystal density of states parameters are also discussed in this section. In section 6.3 the results of our measurements on annealed amorphous silicon oxide samples are shown. Finally, we provide a discussion on the results obtained in section 6.4. In particular we discuss possible mechanisms to explain the unexpected decrease in crystallinity for increasing annealing time when using a hydrogen containing atmosphere.

6.2 Experimental details

We deposited multilayer stacks of silicon oxide on Hereaus Spectrosil 2000 fused quartz substrates. The stacks contained 35 periods of alternating layers of 1 nm thick buffer layer and 3 nm thick silicon-rich hydrogenated silicon oxide. The samples were fabricated using a RF-PECVD setup described in section 2.1.1, using a deposition pressure of 1.4 mbar, substrate temperature of 70 °C and plasma power density of $2.1 \times 10^{-2}\,\mathrm{W\,cm^{-2}}$. The precursor flow rates used for the layers are listed in table 6.1. The atomic composition of the deposited films was determined using x-ray photoelectron spectroscopy (XPS) measurements, using a Thermo Scientific K-Alpha setup, described in section 2.2.1. The film surface was etched with an ion gun prior to measurements to remove surface contamina-

Table 6.1: Precursor flow rates in sccm

Material	SiH_4	CO_2	H_2
Si-rich silicon oxide	10	27	200
Buffer layer	2	72	200

tion. The atomic concentration of silicon in the silicon-rich and buffer layers was 78 and 43 %, respectively. The buffer layer stoichiometry of $SiO_{1.3}$ is sufficiently high to prevent crystallization, as shown in figure 2.6. Annealing was carried out at temperatures of 980, 1000 and 1020 °C and at atmospheric pressure in either pure nitrogen gas, or forming gas using a Solaris 100 RTA furnace, described in section 2.1.3. Samples were measured with XPS before and after annealing and, aside from differences in oxidation states caused by phase separation, no changes in the stoichiometry of the film were observed, indicating that no oxidation from outside the sample occurred during the annealing process.

Raman spectra were measured to determine the crystallinity, using a Renishaw InVia setup in backscattering geometry. The setup and analysis method used are described in section 2.2.3. The cross-sectional transmission electron microscopy (TEM) samples were prepared by mechanical polishing and grazing incidence (6°, 5 kV, final step at 2 kV) Ar-ion milling. The structural properties of the samples were investigated in a FEI-Tecnai F30 TEM with incident electron energy of 300 kV. The inner annular detection angle was set at 10 mrad. The thickness and complex refractive index were obtained from spectroscopic ellipsometry measurements, using a J.A. Woollam Co., Inc. M-2000 Spectroscopic Ellipsometer, described in section 2.2.2. Absorption spectra were obtained using an absolute PDS setup, described in section 2.2.4.

The absorption spectrum of a SiO_x film containing embedded silicon nanocrystals is composed of several contributions: absorption by the silicon nanocrystals, the embedding matrix and defects. Dangling bond defects can mask the low-energy absorption features of nanocrystals [106]. To distinguish between these contributions we use the optical model to fit the absorption coefficient to obtain the material's density of states (DOS) [107], described in chapter 5. For this study, we are most interested in the integrated nanocrystal state density I_{NC}, the nanocrystal absorption energy ϵ_{NC}^{abs}, and the nanocrystal DOS distribution width σ_{NC}. The integrated nanocrystal state density is a measure of the total density of atoms in nanocrystals. The nanocrystal absorption energy is inversely related to the average nanocrystals size, and the nanocrystal DOS distribution width describes the nanocrystal size uniformity, where a narrower DOS distribution corresponds to a narrower size distribution.

6.3 Results

In the ADF images shown in figures 6.1a and b, the silicon nanoparticles appear as bright dot-like contrasts. The collection angle of the ADF images is such that

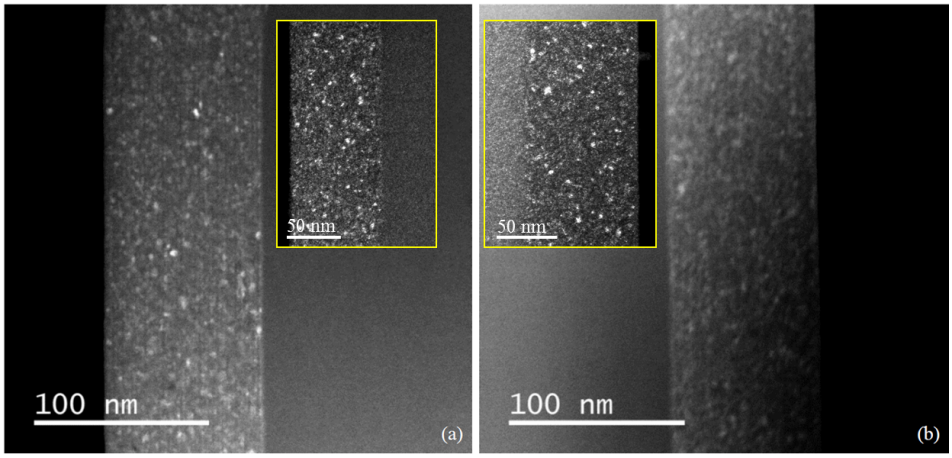

Figure 6.1: ADF TEM images and the dark field TEM images (Inset) were acquired on the sample annealed in forming gas at (a) 3.5 minutes and (b) 4.5 minutes. The inset images are the dark field TEM images.

both diffraction and Z-contrast will make silicon nanoparticles appear brighter. Some nanoparticles appear to be much brighter than others indicating that they are crystallized. To clarify, the inset dark field TEM (DFTEM) images in figures 6.1a and b were including the Si (111) and Si (220). The clear bright dots-like contrasts shown in the DFTEM images confirm the existence of crystalline silicon nanoparticles formed in both films. The contrast of crystalline silicon nanoparticles seen from the DFTEM images is consistent with the contrast observed in the ADF images.

Absorption spectra of an as-deposited sample and samples annealed at 500 °C are shown in figure 6.2. As described in section 1.3.2, this is within the temperature range at which hydrogen effusion occurs. For both annealing atmospheres the material's band gap decreases upon annealing, which is attributed to a decrease in hydrogen caused by hydrogen effusion [108]. Also the sub-band gap absorption increases for both annealing atmospheres, indicating an increase in defect density. The increase is lower for the forming gas annealed sample, compared to the sample annealed in pure nitrogen. Figure 6.3 shows the sub-band gap absorption for samples annealed for varying times in both forming gas and pure nitrogen atmosphere at 1000 °C. The sub-band gap absorption increases rapidly in both cases and subsequently levels off. The saturation of the sub-band gap absorption occurs at approximately 0.5 min and 1 min for samples annealed

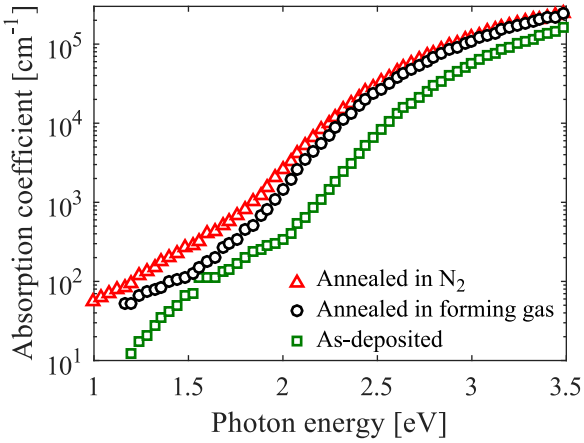

Figure 6.2: Absorption coefficient of an as-deposited sample and samples annealed in forming gas and pure nitrogen at 500 °C.

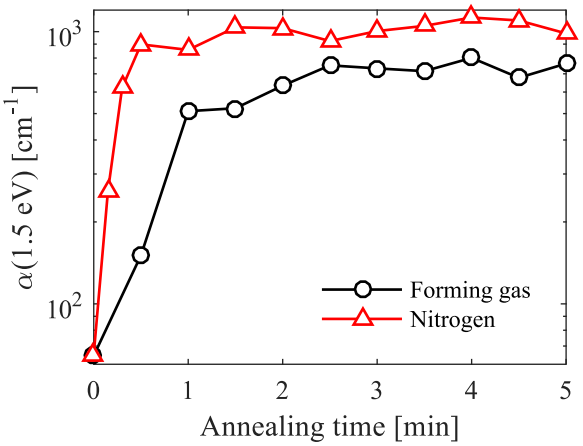

Figure 6.3: Absorption coefficient at 1.5 eV of SiO_x samples as a function of annealing time at 1000 °C. Samples were annealed in forming gas and nitrogen atmospheres.

in nitrogen and forming gas atmosphere, respectively. The sub-band absorption of samples annealed in forming gas is lower for all annealing times.

Figure 6.4 shows the Raman spectrum of a sample annealed at 1000 °C in pure nitrogen for 3 min, with a crystallinity of 0.33. Figure 6.5a shows the crystallinity

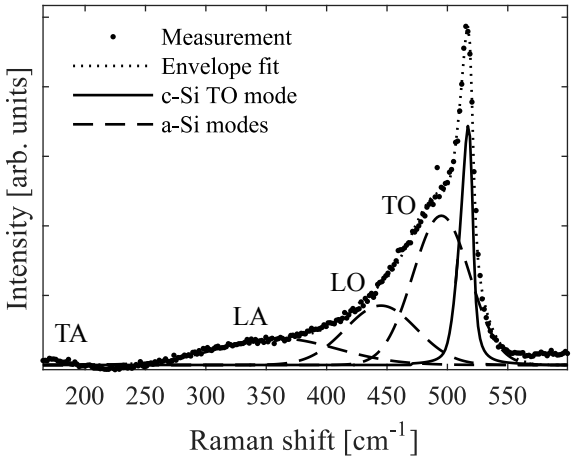

Figure 6.4: Raman spectrum for a sample annealed at 1000 °C in pure nitrogen for 3 min. The dots, the dotted line and the solid line shown the measurement data, the envelope fit and the crystalline silicon TO mode, respectively. The dashed lines show the labeled amorphous silicon modes. The crystallinity of this sample is 0.33.

for samples annealed in pure nitrogen for varying annealing times. The crystallization process follows expected kinetics, described in section 1.3.2. The incubation time and the crystallization and grain growth phase are longest for the lowest annealing temperature. The integrated nanocrystal states density I_{NC} for the samples annealed in nitrogen atmosphere, shown in figure 6.5b, follows a similar trend. This is expected, since an increase in crystallinity reflects an increase in nanocrystal state density within the measured sample volume. The crystallinity and nanocrystal state density for samples annealed in forming gas, shown in figure 6.5c and d, show a different and unexpected trend. Similar to the samples annealed in nitrogen, the crystallization process includes an incubation and crystal growth phase. However, the crystallinity does not saturate. Instead, the crystallinity decreases after reaching a peak. This trend is clearly visible in both Raman and PDS measurements, for samples annealed at varying temperatures.

Figure 6.6a shows the nanocrystal absorption energy for samples annealed in nitrogen atmosphere. The nanocrystal absorption energy at the crystallization onset is high, indicating a small average nanocrystal size. The absorption energy rapidly decreases and stabilizes at a lower value, indicating an increase and subsequent saturation of the nanocrystal size. In contrast, the nanocrystal absorption energy of samples annealed in forming gas, shown in figure 6.6b, does

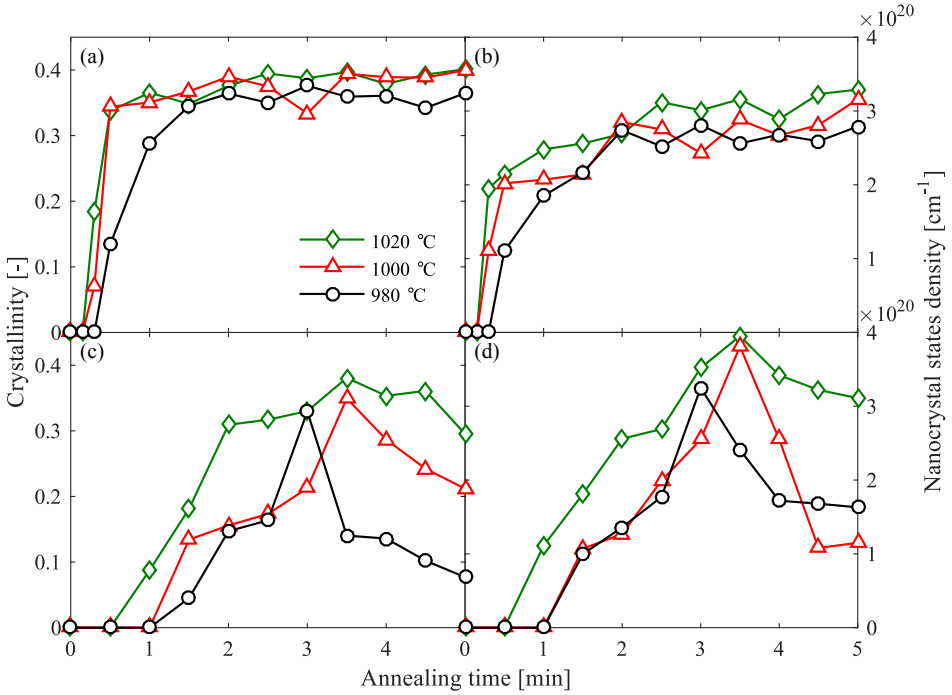

Figure 6.5: Crystallinity of samples annealed in nitrogen (a) and forming gas (c) atmospheres determined using Raman spectroscopy. Also shown are the integrated nanocrystal states obtained from PDS measurement for the same samples, annealed in nitrogen (b) and forming gas (d) atmospheres.

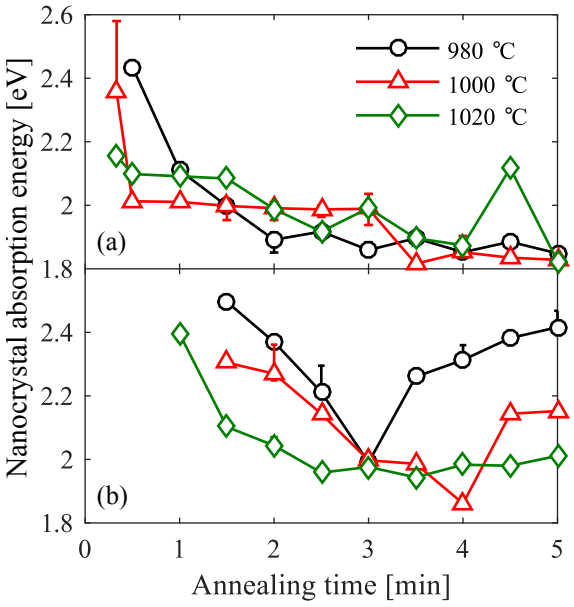

Figure 6.6: Nanocrystal absorption energy obtained from PDS measurements as a function of annealing time for varying annealing temperatures. Samples were annealed in nitrogen (a) and forming gas (b) atmospheres.

not saturate, but increases after an initial decrease, indicating that, on average, the nanocrystals first grow in size and subsequently shrink.

The nanocrystal absorption energy as a function of crystallinity is shown in figures 6.7a and b, for samples annealed in nitrogen and forming gas, respectively. As expected, the nanocrystal absorption energy of samples annealed in nitrogen

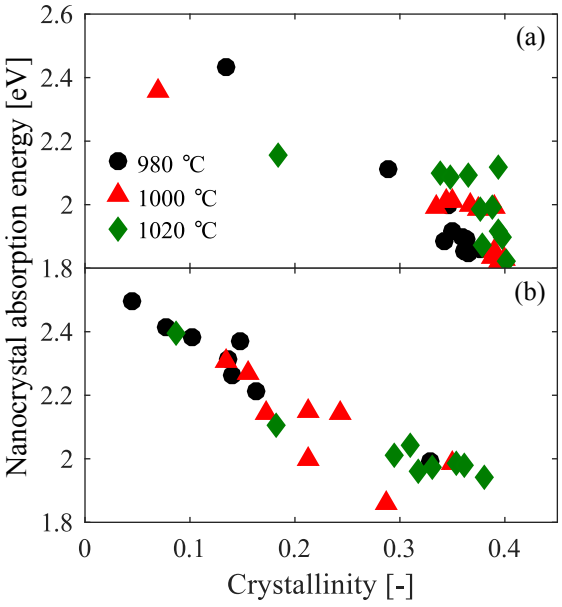

Figure 6.7: Nanocrystal absorption energy obtained from PDS measurements of samples annealed in nitrogen (a) and forming gas (b) as a function of crystallinity for varying annealing temperatures.

atmosphere decreases with increasing crystallinity, implying that the nanocrystals existing at the crystallization onset grow in size. Note that this does not exclude that new, small-sized nanocrystals are being formed, contributing to an increase in crystallinity. It does mean that the average nanocrystal size increases with increasing crystallinity.

Interestingly, a similar trend is observed for samples annealed in forming gas. For these samples the crystallinity decreases when annealed for longer times. This means that the decrease in crystallinity is directly related to a decrease in average nanocrystal size.

Figure 6.8a shows the nanocrystal DOS distribution width as a function of annealing time for samples annealed in a nitrogen atmosphere. The nanocrystal DOS distribution width decreases for samples annealed for a short time and, similar to the crystallinity and nanocrystal absorption energy, it stabilizes for longer annealing times. This indicates that after the crystallization onset, the nanocrystal size distribution is relatively wide and narrows for samples annealed

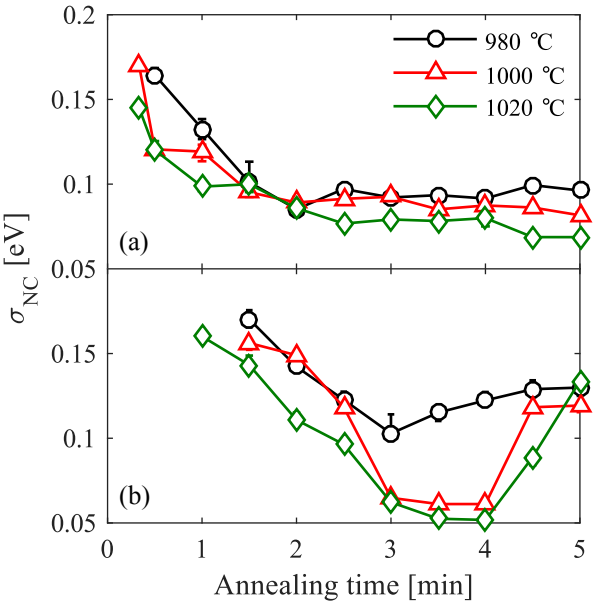

Figure 6.8: Nanocrystal DOS distribution width obtained from PDS measurements as a function of annealing time for varying annealing temperatures. Samples were annealed in nitrogen (a) and forming gas (b) atmospheres.

for longer times before stabilizing. For samples annealed in forming gas, shown in figure 6.8b, the nanocrystal DOS distribution width also shows a decrease for short annealing times, indicating a narrowing of the nanocrystal size distribution. However, instead of stabilizing like the samples annealed in nitrogen, the DOS distribution width of the forming gas annealed samples increases, indicating a decrease in nanocrystal size homogeneity in the measured sample volume.

6.4 Discussion

The sub-band gap absorption of samples annealed in forming gas is lower than samples annealed in pure nitrogen, indicating that hydrogen in the annealing atmosphere reduces the defect density generated during annealing. However, hydrogen in the annealing atmosphere also changes the crystallization process. As described in section 6.1, the expected crystallization behavior of amorphous silicon consists of three stages:

1. Incubation,
2. crystallization and grain growth,
3. and saturation.

All samples follow the first two of these phases. In line with phase (i), after an incubation time, the crystallinity and average crystal size increase for all samples, coherent with phase (ii). For samples annealed in pure nitrogen atmosphere, the crystallinity subsequently saturates, consistent with phase (iii). Furthermore, PDS measurements show that also the average crystal size and size uniformity saturate, indicating that the crystallization process is finished and the crystals stop growing at that point. Samples annealed in forming gas, however, do not saturate. Instead, their crystallinity, crystal size and size uniformity decrease after reaching a maximum. It was technically not possible to extend the annealing time further, but the trend is clear for all temperatures used, and was confirmed by PDS and Raman measurements. Note that although samples annealed in forming gas atmosphere exhibited an incubation and crystal growth phase, these phases are significantly longer compared to samples annealed in pure nitrogen atmosphere. So, aside from affecting the saturation phase, forming gas also causes a deceleration of the kinetics involved in the first two phases. The only difference between the two procedures is the annealing atmosphere. More specifically the presence of hydrogen gas in the forming gas atmosphere.

Spontaneous dissociation of molecular hydrogen into atomic hydrogen occurs at 5000 °C [109], which is significantly higher than the temperatures used in this study. However, Gabis showed that for amorphous silicon, molecular hydrogen can be captured at the film interface and can subsequently diffuse through the film. He determined that hydrogen in amorphous silicon is transported in its dissociated, atomic form [110]. For silicon dioxide, hydrogen molecules dissolve and

diffuse easily. Its solubility is almost independent of temperature and is proportional to the partial gas pressure [111]. Furthermore, several experimental studies have demonstrated the passivation of surface and bulk dangling bonds in silicon oxide using H_2 gas [112, 113] (at 23 to 450 °C and 23 to 900 °C, respectively), implying diffusion of molecular or atomic hydrogen into the film.

Since the only difference between the samples annealed in pure nitrogen and forming gas is the presence of hydrogen, hydrogen directly or indirectly causes the nanocrystal size reduction in samples annealed in forming gas. When the nanocrystals shrink, their outer shell is transformed into non-crystalline-silicon material. Such a core-shell structure has been observed with TEM for silicon nanocrystals [28, 69]. Since our samples contain silicon and oxygen, there is a limited number of options for the composition and phase of this shell: it can be either be amorphous silicon or silicon oxide. We will first discuss possible mechanisms for the growth of these respective shells and subsequently discuss which is more likely to occur.

Neitzert *et al.* observed the growth of an amorphous silicon layer on crystalline silicon when exposed to a hydrogen plasma [114]. Although our samples were not exposed to a plasma during annealing, the annealing temperature at approximately 1000 °C is significantly higher than the 250 °C used by Neitzert *et al.* Possibly, atomic hydrogen at high temperature could cause a similar amorphization reaction. Aside from possible amorphization, hydrogen also strongly increases the thermal oxidation rate of crystalline silicon [115, 116] and it is able to catalyze the oxidation reaction [117].

Thermodynamically, an extended amorphous silicon shell around a crystalline silicon core is unlikely, since it would involve a second interface formation energy between crystalline and amorphous silicon [68]. Furthermore, since also the incubation time and crystal growth rate are affected, hydrogen capture and diffusion can be assumed to be relatively fast processes. This implies that such an amorphization process should start quickly after or even at the same moment as the crystallization onset. In that case, crystallization and amorphization would be competing processes and eventually an equilibrium between the two processes should establish. So, after a longer time with respect to samples not exposed to hydrogen, a saturation in crystallinity should be reached. Instead, our measurements show that the crystallinity does not saturate. It initially increases and after reaching a maximum, the crystallinity decreases. This implies that the amorphization rate, at some point, is greater than the crystallization rate, which is unlikely.

The other option is that a silicon oxide shell around the crystalline silicon core is formed. In that case crystallization and oxidation are competing processes. Again, the duration of the incubation time and the crystal growth time will be increased by the competing oxidation process. In this case, however, an equilibrium does not necessarily need to be formed. At some point the excess silicon in a nanocrystal's immediate vicinity is depleted, preventing its further growth. Simultaneously, the oxidation could still occur, provided sufficient mobile oxy-

gen atoms are available in its vicinity. It is likely that more mobile oxygen atoms are available, since phase separation already occurred, resulting in silicon particles in a silicon-poor, oxide-rich matrix. Furthermore, the diffusion coefficient of oxygen in silicon oxide is five orders of magnitude higher than that of silicon in silicon oxide [118]. When that happens, crystallization is limited, slowing down the crystallization rate, while the oxidation rate remains high, leading to a size reduction of the nanocrystal.

This does not explain why the size distribution width increases, however. According to our observations, not all nanocrystals shrink with the same rate. Note that the nanocrystal DOS distribution width σ_{NC} is a convolution of the nanocrystal size distribution in the measured sample volume and their individual dispersion in energy states [107]. For a single infinitesimally small nanocrystal, σ_{NC} would be extremely narrow. A single bigger nanocrystal would contain a dispersion of energy states and would therefore result in a widening of σ_{NC}. This means that if all nanocrystals would shrink by the same amount (both relatively and absolute), σ_{NC} should decrease, reflecting the decrease in density of states and therefore also a decrease in their individual energy dispersion. Instead, we observe an increase in σ_{NC}, implying that the rate of size decrease is non-uniform. This suggests additional complex mechanisms, perhaps an oxidation rate which is dependent on the nanocrystal size. However, this is outside of the scope of this article.

6.5 Conclusions

We show that hydrogen gas during annealing leads to a lower sub-band gap absorption compared to samples annealed in pure nitrogen, indicating passivation of defects created during annealing. Samples annealed in pure nitrogen show expected trends according to crystallization theory, including an incubation time and subsequent increase and stabilization of crystallinity. Samples annealed in forming gas, however, deviate from this expected trend. After an incubation time and increase in crystallinity, the crystallinity decreases for increased annealing time. Furthermore, PDS measurements show that the mean nanocrystal size decreases and the size distribution broadens, indicating that hydrogen diffuses into the material and causes a size reduction of the silicon nanocrystals.

7 Conclusions

The major conclusions and achievements of our work are:

- We demonstrated an analytical method to optimize the composition of silicon-rich layer for different crystallinities thicknesses in order to achieve the highest density of non-touching and closely spaced silicon nanocrystals after annealing. The optimal stoichiometry depends on the crystallinity and decreases for increasing silicon-rich layer thicknesses. However, for silicon-rich layers thinner than approximately 2 nm the optimal composition does not vary with thickness. This method can be used to find the best as-deposited composition in order to achieve optimal nanocrystal density and spacing after a subsequent annealing step.

- We have demonstrated the NLoG method to quickly detect and measure nanocrystals in a TEM image to obtain the nanocrystal size distribution with minimum user input. The method uses a convolution of the TEM image with NLoG filters. Furthermore, we show that the input parameters for this method can be optimized for one image and can then be applied to similar images with comparable or smaller pixel sizes, leading to accurate results. We compared the accuracy and speed of this method with other methods used in literature and the proposed method performed comparable or better in the image test set.

- Furthermore, we have developed an analytical correction for the effect of slicing nanocrystals during TEM sample preparation on the apparent nanocrystal size distribution. We derived an equation for the apparent nanocrystal size for a given real nanocrystal size. Assuming a certain nanocrystal distribution shape, this equation can be used to fit a real nanocrystal size distribution from a measured apparent size distribution.

- A non-destructive measurement and simple analysis method for obtaining the absorption coefficient of silicon NCs embedded in an amorphous matrix is presented. Furthermore, we proposed a model to extract the optical properties and the DOS of both the NCs and their embedding matrix. Using this model, we propose a growth model for embedded NCs created by laser annealing Si-rich a-SiO_x. We find that an increasing laser fluence leads to a reduction of the NC band gap and a reduction in NC DOS distribution

width, indicating larger mean NC sizes and narrower NC size distribution for increasing laser fluences.

- For laser annealed a-$Si_{0.66}O_{0.34}$:H films, we observe hydrogen effusion and an increase in sub-band gap absorption at low laser fluences. For laser fluences in excess of 120 mJ cm^{-2}, crystallization of silicon occurs and the crystallinity increases with increasing laser fluence. For laser fluences larger than the crystallization threshold of 140 mJ cm^{-2}, changes to the sub-band gap absorption and relative hydrogen content are insignificant. From these results we conclude that defect creation occurs predominantly at laser fluences below the crystallization threshold.

- Using the model developed and described in chapter 5 we show that hydrogen gas during annealing leads to a lower sub-band gap absorption compared to samples annealed in pure nitrogen, indicating passivation of defects created during annealing. Samples annealed in pure nitrogen show expected trends according to crystallization theory, including an incubation time and subsequent increase and stabilization of crystallinity. Samples annealed in forming gas, however, deviate from this expected trend. After an incubation time and increase in crystallinity, the crystallinity decreases for increased annealing time. Furthermore, PDS measurements show that the mean nanocrystal size decreases and the size distribution broadens, indicating that hydrogen diffuses into the material and causes a size reduction of the silicon nanocrystals.

Bibliography

[1] W. Shockley and H. J. Queisser, J. Appl. Phys. **32**, 510 (1961).

[2] G. B. Rybicki and A. P. Lightman, eds., *Radiative Processes in Astrophysics* (Wiley-Blackwell, 1985).

[3] M. A. Green, Solid-State Electronics **24**, 788 (1981).

[4] P. T. Chiu, D. C. Law, R. L. Woo, S. B. Singer, D. Bhusari, W. D. Hong, A. Zakaria, J. Boisvert, S. Mesropian, R. R. King, and N. H. Karam, in *2014 IEEE 40th Photovoltaic Specialist Conference (PVSC)* (Institute of Electrical & Electronics Engineers (IEEE), 2014) pp. 0011–0013.

[5] M. A. Green, K. Emery, Y. Hishikawa, W. Warta, and E. D. Dunlop, Prog. Photovolt: Res. Appl. **24**, 3 (2015).

[6] G. B. Haxel, J. B. Hedrick, and G. J. Orris, *Rare Earth Elements – Critical Resources for High Technology*, U.S. Geological Survey 087-02 (U.S. Geological Survey, 2002).

[7] D. Roy, P. Gaur, N. Verma, M. Pathireddy, and K. P. Singh, International Journal of Environmental Bioremediation & Biodegradation **1**, 14 (2013).

[8] M. A. Green, E.-C. Cho, Y. Cho, Y. Huang, E. Pink, T. Trupke, A. Lin, T. Fangsuwannarak, T. Puzzer, G. Conibeer, and R. Corkish, in *Proceedings of the 20th European Photovoltaic Solar Energy Conference and Exhibition* (2005) pp. 3–7.

[9] E. H. Kennard, Zeitschrift für Physik **44**, 326 (1927).

[10] A. D. Yoffe, Adv. Phys. **42**, 173 (1993).

[11] G. Conibeer, M. A. Green, E.-C. Cho, D. König, Y.-H. Cho, T. Fangsuwannarak, G. Scardera, E. Pink, Y. Huang, T. Puzzer, S. Huang, D. Song, C. Flynn, S. Park, X. Hao, and D. Mansfield, Thin Solid Films **516**, 6748 (2008).

[12] M. Schnabel, C. Weiss, P. Löper, P. R. Wilshaw, and S. Janz, phys. stat. sol. (a) **212**, 1649 (2015).

[13] C. Bulutay and S. Ossicini, "Electronic and optical properties of silicon nanocrystals," in *Silicon Nanocrystals* (Wiley-Blackwell, 2010) pp. 5–41.

[14] P. Harrison, *Quantum Wells, Wires and Dots* (Wiley-Blackwell, 2005).

[15] K. Kůsová, L. Ondič, E. Klimešová, K. Herynková, I. Pelant, S. Daniš, J. Valenta, M. Gallart, M. Ziegler, B. Hönerlage, and P. Gilliot, Appl. Phys. Lett. **101**, 143101 (2012).

[16] K. Dohnalová, K. Kůsová, and I. Pelant, Appl. Phys. Lett. **94**, 211903 (2009).

[17] L. Koponen, L. Tunturivuori, M. Puska, and R. Nieminen, Phys. Rev. B **79**, 235332 (2009).

[18] T. van Buuren, L. N. Dinh, L. L. Chase, W. J. Siekhaus, and L. J. Terminello, Phys. Rev. Lett. **80**, 3803 (1998).

[19] F. Iacona, G. Franzò, and C. Spinella, J. Appl. Phys. **87**, 1295 (2000).

[20] H. Takagi, H. Ogawa, Y. Yamazaki, A. Ishizaki, and T. Nakagiri, Appl. Phys. Lett. **56**, 2379 (1990).

[21] G. Conibeer, M. A. Green, R. Corkish, Y. Cho, E.-C. Cho, C.-W. Jiang, T. Fangsuwannarak, E. Pink, Y. Huang, T. Puzzer, T. Trupke, B. Richards, A. Shalav, and K. lung Lin, Thin Solid Films **511–512**, 654 (2006).

[22] C. Song, G. R. Chen, J. Xu, T. Wang, H. C. Sun, Y. Liu, W. Li, Z. Y. Ma, L. Xu, X. F. Huang, and K. J. Chen, J. Appl. Phys. **105**, 054901 (2009).

[23] K. Ding, U. Aeberhard, O. Astakhov, W. Beyer, F. Finger, R. Carius, and U. Rau, Sol. Energy Mater. Sol. Cells **129**, 3 (2014).

[24] A. Sarikov and M. Zacharias, Journal of Physics: Condensed Matter **24**, 385403 (2012).

[25] L. X. Yi, J. Heitmann, R. Scholz, and M. Zacharias, Appl. Phys. Lett. **81**, 4248 (2002).

[26] R. B. Iverson and R. Reif, J. Appl. Phys. **62**, 1675 (1987).

[27] I.-C. Chen, P.-Y. Lin, T. T. Li, and J.-Y. Chang, ECS J. Solid State Sci. Technol. **3**, N75 (2014).

[28] J. López-Vidrier, S. Hernández, A. Hartel, D. Hiller, S. Gutsch, P. Löper, L. López-Conesa, S. Estradé, F. Peiró, M. Zacharias, and B. Garrido, Energy Procedia **10**, 43 (2011).

[29] G. Conibeer, I. Perez-Wurfl, X. Hao, D. Di, and D. Lin, Nanoscale Res. Lett. **7**, 193 (2012).

[30] B. Garrido, S. Hernández, Y. Berencén, J. López-Vidrier, J. Ramírez, O. Blázquez, and B. Mundet, in *Light Energy Harvesting with Group IV Nanostructures* (Pan Stanford, 2015) pp. 255–316.

[31] N. R. Mavilla, V. Chavan, C. S. Solanki, and J. Vasi, Thin Solid Films **612**, 41 (2016).

[32] I. Balberg, J. Appl. Phys. **110**, 061301 (2011).

[33] C.-W. Jiang and M. A. Green, J. Appl. Phys. **99**, 114902 (2006).

[34] A. R. Stegner, R. N. Pereira, K. Klein, R. Lechner, R. Dietmueller, M. S. Brandt, M. Stutzmann, and H. Wiggers, Phys. Rev. Lett. **100**, 026803 (2008).

[35] R. Lechner, A. R. Stegner, R. N. Pereira, R. Dietmueller, M. S. Brandt, A. Ebbers, M. Trocha, H. Wiggers, and M. Stutzmann, J. Appl. Phys. **104**, 053701 (2008).

[36] G. Conibeer, M. A. Green, D. KÃűnig, I. Perez-Wurfl, S. Huang, X. Hao, D. Di, L. Shi, S. Shrestha, B. Puthen-Veetil, Y. So, B. Zhang, and Z. Wan, Prog. Photovolt: Res. Appl. **19**, 813 (2010).

[37] J. Heitmann, F. Müller, M. Zacharias, and U. Gösele, Adv. Mater. **17**, 795 (2005).

[38] M. Künle, T. Kaltenbach, P. Löper, A. Hartel, S. Janz, O. Eibl, and K.-G. Nickel, Thin Solid Films **519**, 151 (2010).

[39] B. Puthen-Veettil, R. Patterson, D. König, G. Conibeer, and M. A. Green, J. Appl. Phys. **116**, 163707 (2014).

[40] V. Osinniy, S. Lysgaard, V. Kolkovsky, V. Pankratov, and A. Nylandsted Larsen, Nanotechnology **20**, 195201 (2009).

[41] Q. Cheng, E. Tam, S. Xu, and K. K. Ostrikov, Nanoscale **2**, 594 (2010).

[42] I. F. Crowe, M. P. Halsall, O. Hulko, A. P. Knights, R. M. Gwilliam, M. Wojdak, and A. J. Kenyon, J. Appl. Phys. **109**, 083534 (2011).

[43] M. Sezgin and B. Sankur, J. Electron. Imaging **13**, 146 (2004).

[44] G. H. Woehrle, J. E. Hutchison, S. Ozkar, and R. G. Finke, Turk. J. Chem. **30**, 1 (2006).

[45] L. C. Gontard, D. Ozkaya, and R. E. Dunin-Borkowski, Ultramicroscopy **111**, 101 (2011).

[46] W. D. Pyrz and D. J. Buttrey, Langmuir **24**, 11350 (2008).

[47] S. Mondini, A. M. Ferretti, A. Puglisi, and A. Ponti, Nanoscale **4**, 5356 (2012).

[48] B. Sain and D. Das, RSC Adv. **4**, 36929 (2014).

[49] D. Song, E.-C. Cho, G. Conibeer, Y.-H. Cho, Y. Huang, S. Huang, C. Flynn, and M. A. Green, J. Vac. Sci. Technol. B **25**, 1327 (2007).

[50] K. Ding, U. Aeberhard, W. Beyer, O. Astakhov, F. Köhler, U. Breuer, F. Finger, R. Carius, and U. Rau, phys. stat. sol. (a) **209**, 1960 (2012).

[51] S.-H. Chen, H.-W. Wang, and T.-W. Chang, Opt. Express **20**, A197 (2012).

[52] M. Zacharias, D. Hiller, A. Hartel, and S. Gutsch, phys. stat. sol. (a) **209**, 2449 (2012).

[53] R. Limpens, S. L. Luxembourg, A. W. Weeber, and T. Gregorkiewicz, Sci. Rep. **6**, 19566 (2016).

[54] Y.-J. Jung, J.-H. Yoon, R. G. Elliman, and A. R. Wilkinson, J. Appl. Phys. **104**, 083518 (2008).

[55] S. Godefroo, M. Hayne, M. Jivanescu, A. Stesmans, M. Zacharias, O. I. Lebedev, G. Van Tendeloo, and V. V. Moshchalkov, Nat. Nanotechnol. **3**, 174 (2008).

[56] J. Xu, W. Mu, Z. Xia, H. Sun, D. Wei, W. Li, Z. Ma, and K. Chen, J. Non-Cryst. Solids **358**, 2141 (2012).

[57] M. López, B. Garrido, C. García, P. Pellegrino, Pérez-Rodríguez, J. R. Morante, C. Bonafos, M. Carrada, and A. Claverie, Appl. Phys. Lett. **80**, 1637 (2002).

[58] D. Comedi, O. H. Y. Zalloum, and P. Mascher, Appl. Phys. Lett. **87**, 213110 (2005).

[59] S. Cheylan and R. G. Elliman, Appl. Phys. Lett. **78**, 1225 (2001).

[60] A. S. Ferlauto, G. M. Ferreira, J. M. Pearce, C. R. Wronski, R. W. Collins, X. Deng, and G. Ganguly, J. Appl. Phys. **92**, 2424 (2002).

[61] S. H. Wemple, Phys. Rev. B **7**, 3767 (1973).

[62] C. Smit, R. A. C. M. M. van Swaaij, H. Donker, A. M. H. N. Petit, W. M. M. Kessels, and M. C. M. van de Sanden, J. Appl. Phys. **94**, 3582 (2003).

[63] G. Franzò, M. Miritello, S. Boninelli, R. Lo Savio, M. G. Grimaldi, F. Priolo, F. Iacona, G. Nicotra, C. Spinella, and S. Coffa, J. Appl. Phys. **104**, 094306 (2008).

[64] W. B. Jackson, N. M. Amer, A. C. Boccara, and D. Fournier, Appl. Opt. **20**, 1333 (1981).

[65] Z. Remes, R. Vasudevan, K. Jarolimek, A. H. Smets, and M. Zeman, Solid State Phenomena **213**, 19 (2014).

[66] C. A. Schneider, W. S. Rasband, and K. W. Eliceiri, Nat. Methods **9**, 671 (2012).

[67] S. Gutsch, D. Hiller, J. Laube, M. Zacharias, and C. Kübel, Beilstein J. Nanotechnol. **6**, 964 (2015).

[68] D. Hiller, "Silicon nanoclusters embedded in dielectric matrices: Nucleation, growth, crystallization, and defects," in *Light Energy Harvesting with Group IV Nanostructures*, edited by J. Valenta and S. Mirabella (Pan Stanford Publishing, 2015) Chap. Silicon Nanoclusters Embedded in Dielectric Matrices: Nucleation, Growth, Crystallization, and Defects, pp. 99–144.

[69] F. Iacona, C. Bongiorno, C. Spinella, S. Boninelli, and F. Priolo, J. Appl. Phys. **95**, 3723 (2004).

[70] N. Daldosso, M. Luppi, G. Dalba, L. Pavesi, F. Rocca, F. Priolo, G. Franzò, F. Iacona, E. Degoli, R. Magri, and S. Ossicini, in *MRS Proc.*, Vol. 770 (2003) p. I6.

[71] K. T. Queeney, M. K. Weldon, J. P. Chang, Y. J. Chabal, A. B. Gurevich, J. Sapjeta, and R. L. Opila, J. Appl. Phys. **87**, 1322 (2000).

[72] A. Zimina, S. Eisebitt, W. Eberhardt, J. Heitmann, and M. Zacharias, Appl. Phys. Lett. **88**, 163103 (2006).

[73] X. Zhang, "Silicon/electrolyte interface," in *Electrochemistry of Silicon and Its Oxide* (Springer, 2001) pp. 45–90.

[74] W. Kessels, M. V. D. Sanden, R. Severens, L. V. Ijzendoorn, and D. Schram, in *MRS Proceedings*, Vol. 507 (Cambridge University Press, 1998) pp. 529–534.

[75] S. Sze and K. K. Ng, "Appendix G: Properties of Si and GaAs," in *Physics of Semiconductor Devices* (Wiley-Blackwell, 2006) p. 790.

[76] X. Zhang, "Anodic oxide," in *Electrochemistry of Silicon and Its Oxide* (Springer, 2001) pp. 91–130.

[77] F. Tournus, J. Nanopart. Res. **13**, 5211 (2011).

[78] J. López-Vidrier, S. Hernández, D. Hiller, S. Gutsch, L. López-Conesa, S. Estradé, F. Peiró, M. Zacharias, and B. Garrido, J. Appl. Phys. **116**, 133505 (2014).

[79] J. Laube, S. Gutsch, D. Wang, C. Kübel, M. Zacharias, and D. Hiller, Appl. Phys. Lett. **108**, 043106 (2016).

[80] T. Lindeberg, Int. J. Comput. Vision **30**, 79 (1998).

[81] D. Marr and E. Hildreth, Proc. R. Soc. Lond. B **207**, 187 (1980).

[82] J. Canny, IEEE Transactions on Pattern Analysis and Machine Intelligence **PAMI-8**, 679 (1986).

[83] R. Gonzalez and R. Woods, "Image enhancement in the spatial domain," in *Digital Image Processing*, International Edition (Prentice Hall, 2002) pp. 75–103, 2nd ed.

[84] A. A. Langford, M. L. Fleet, B. P. Nelson, W. A. Lanford, and N. Maley, Phys. Rev. B **45**, 13367 (1992).

[85] I. Jonak-Auer, R. Meisels, and F. Kuchar, Infrared Physics & Technology **38**, 223 (1997).

[86] V. A. Volodin and D. I. Koshelev, J. Raman Spectrosc. **44**, 1760 (2013).

[87] D. V. Tsu, G. Lucovsky, and B. N. Davidson, Phys. Rev. B **40**, 1795 (1989).

[88] K. Kawamura, S. Ishizuka, H. Sakaue, and Y. Horiike, Jpn. J. Appl. Phys. **30**, 3215 (1991).

[89] R. Tsu, J. Gonzalez-Hernandez, S. S. Chao, S. C. Lee, and K. Tanaka, Appl. Phys. Lett. **40**, 534 (1982).

[90] A. T. Voutsas, M. K. Hatalis, J. Boyce, and A. Chiang, J. Appl. Phys. **78**, 6999 (1995).

[91] V. Denisov, B. Mavrin, M. Koosh, and I. Pochik, J. Appl. Spectrosc. **55**, 1037 (1991).

[92] A. H. M. Smets, W. M. M. Kessels, and M. C. M. van de Sanden, Appl. Phys. Lett. **82**, 1547 (2003).

[93] D. Ritter and K. Weiser, Opt. Commun. **57**, 336 (1986).

[94] J. Kočka, M. Vaněček, and A. Tříska, "Energy and density of gap states in a-Si:H," in *Amorphous Silicon and Related Materials*, Advanced Series on Amorphous Semiconductors (World Scientific, 1989) pp. 297–327.

[95] M. Zeman, "Advanced amorphous silicon solar cell technologies," in *Thin Film Solar Cells*, edited by J. Poortmans and V. Arkhipov (Wiley-Blackwell, 2006) Chap. Advanced Amorphous Silicon Solar Cell Technologies, pp. 173–236.

[96] S. K. O'Leary, J. Mater. Sci.: Mater. Electron. **15**, 401 (2004).

[97] B. Yu and L. Qian, Nanoscale Res. Lett. **8**, 137 (2013).

[98] L. Zhang, K. Chen, L. Wang, W. Li, J. Xu, X. Huang, and K. Chen, J. Phys.: Condens. Matter **14**, 10083 (2002).

[99] M. Luppi and S. Ossicini, Phys. Rev. B **71**, 035340 (2005).

[100] G. Ledoux, O. Guillois, D. Porterat, C. Reynaud, F. Huisken, B. Kohn, and V. Paillard, Phys. Rev. B **62**, 15942 (2000).

[101] L. V. Mercaldo, E. M. Esposito, P. D. Veneri, G. Fameli, S. Mirabella, and G. Nicotra, Appl. Phys. Lett. **97**, 153112 (2010).

[102] F. Urbach, Phys. Rev. **92**, 1324 (1953).

[103] Y. Li, P. Liang, Z. Hu, S. Guo, H. Cai, F. Huang, J. Sun, N. Xu, and J. Wu, Applied Surface Science **320**, 804 (2014).

[104] A. Coyopol, M. Cardona, T. D. Becerril, L. Licea-Jimenez, and A. M. Sánchez, J. Lumin. **176**, 40 (2016).

[105] K. Seino, F. Bechstedt, and P. Kroll, Nanotechnology **20**, 135702 (2009).

[106] B. G. Lee, D. Hiller, J.-W. Luo, O. E. Semonin, M. C. Beard, M. Zacharias, and P. Stradins, Adv. Funct. Mater. **22**, 3223 (2012).

[107] M. van Sebille, R. A. Vasudevan, R. J. Lancee, R. A. C. M. M. van Swaaij, and M. Zeman, J. Phys. D: Appl. Phys. **48**, 325302 (2015).

[108] C. Walder, M. Kellermann, E. Wendler, J. Rensberg, K. von Maydell, and C. Agert, EPJ Photovolt. **6**, 65302 (2015).

[109] W. R. Magro, D. M. Ceperley, C. Pierleoni, and B. Bernu, Phys. Rev. Lett. **76**, 1240 (1996).

[110] I. E. Gabis, Semiconductors **31**, 110 (1997).

[111] R. H. Doremus, J. Phys. Chem. **80**, 1773 (1976).

[112] Z. Li, S. J. Fonash, E. H. Poindexter, M. Harmatz, F. Rong, and W. R. Buchwald, J. Non-Cryst. Solids **126**, 173 (1990).

[113] V. A. Radzig, V. N. Bagratashvili, S. I. Tsypina, P. V. Chernov, and A. O. Rybaltovskii, J. Phys. Chem. **99**, 6640 (1995).

[114] H. C. Neitzert, N. Layadi, P. R. i Cabarrocas, R. Vanderhaghen, and M. Kunst, J. Appl. Phys. **78**, 1438 (1995).

[115] A. G. Revesz, J. Electrochem. Soc. **126**, 122 (1979).

[116] R. C. Newman, Vacuum **42**, 379 (1991).

[117] T. Nakayama and F. C. Collins, J. Electrochem. Soc. **113**, 706 (1966).

[118] H. A. Schaeffer, J. Non-Cryst. Solids **38-39**, 545 (1980).

Summary

Direct conversion of light into electricity is one of the most promising approaches to provide renewable energy on a large scale. Solar-cells are devices that use the photovoltaic effect to convert sunlight into electricity. Single-junction solar-cells all suffer from spectral mismatch, reducing their cell's efficiency. Photons with lower energy than the absorber material's band gap will be transmitted and photons with higher energy than the band gap will lose the excess energy through thermalization processes as heat. One solution to prevent excessive thermalization is to use multiple absorber materials with varying band gaps. This can be achieved using silicon nanocrystals embedded in a dielectric matrix made of silicon and its compounds with oxygen, nitrogen and carbon. The different band gaps needed for efficient spectral matching can be accomplished by utilizing the size-dependent quantum confinement in nanometer-sized crystals.

Using films containing alternating layers of stoichiometric and silicon-rich silicon alloys allows for the control over the nanocrystal size, limited to the silicon-rich layer thickness. Although no clear consensus exists concerning the exact charge carrier transport mechanisms, the total charge transport is expected to be highly dependent on the nanocrystal spacing and the choice of dielectric material. The nanocrystal density in the silicon-rich layers can be controlled by tuning the composition of these layers during deposition. A low silicon content leads to relatively few isolated nanocrystals, and increasing the excess silicon content will eventually lead to clustering of nanocrystals. When the nanocrystal density is too low, the probability of a nearest-neighbor nanocrystal within the transport-distance is too low. In contrast, when the excess silicon content is too high, nanocrystals are so closely spaced that they start clustering, which reduces the quantum confinement in these crystals. This means there is an optimal composition to achieve a limited nanocrystals spacing, while limiting clustering. In **chapter 3** we demonstrate an analytical method to optimize the stoichiometry and thickness of multilayer silicon oxide films in order to achieve the highest density of non-touching and closely spaced silicon nanocrystals after annealing. The probability of a nanocrystal nearest-neighbor distance within a limited range is calculated using the stoichiometry of the as-deposited film and the crystallinity of the annealed film as input parameters. Multiplying this probability with the nanocrystal density results in the density of non-touching and closely spaced silicon nanocrystals.

Limited by the nanometer-scale dimensions of nanocrystals, transmission electron microscopy (TEM) is the only direct measurement tool capable of capturing the size and shape of embedded nanocrystals. However, a quick method to measure nanocrystals in TEM images with minimal user input to minimize user bias has been lacking. In **chapter 4** we propose a method with minimal bias caused by user input to quickly detect and measure the nanocrystal size distribution from

transmission electron microscopy images using a combination of Laplacian of Gaussian filters and non-maximum suppression. We demonstrate the proposed method on bright-field TEM images of an a-SiC:H sample containing embedded silicon nanocrystals with varying magnifications and we compare the accuracy and speed with size distributions obtained by manual measurements, a thresholding method and PEBBLES. Finally, we analytically consider the error induced by slicing nanocrystals during TEM sample preparation on the measured nanocrystal size distribution and formulate an equation to correct for this effect.

To the best of our knowledge, a method to obtain the nanocrystal absorption properties and their density of states from absorption spectra has not been developed yet. In **chapter 5** we present a non-destructive measurement and simple analysis method for obtaining the absorption coefficient of silicon nanocrystals embedded in an amorphous matrix. This method enables us to pinpoint the contribution of silicon nanocrystals to the absorption spectrum of nanocrystal containing films. The density of states (DOS) of the amorphous matrix is modeled using the standard model for amorphous silicon while the nanocrystals are modeled using one Gaussian distribution for the occupied states and one for the unoccupied states. For laser annealed a-$Si_{0.66}O_{0.34}$:H films, our analysis shows a reduction of the nanocrystal band gap from approximately 2.34 to 2.08 eV indicating larger mean nanocrystal size for increasing annealing laser fluences, accompanied by a reduction in nanocrystal DOS distribution width from 0.28 to 0.26 eV, indicating a narrower size distribution.

Embedded silicon nanocrystals can be made by annealing silicon-rich silicon alloy films. Since hydrogen effusion occurs at lower temperatures than phase separation and crystallization, this cannot be avoided, leading to an increased defect density. Reincorporation of hydrogen into the material is considered to be an effective method to reduce the defect density. One option is to combine annealing and hydrogen passivation in a single processing step, by annealing in a H_2 containing atmosphere. In **chapter 6** we report the effect of hydrogen on the crystallization process of silicon nanocrystals embedded in a silicon oxide matrix. We show that hydrogen gas during annealing leads to a lower sub-band gap absorption, indicating passivation of defects created during annealing. Samples annealed in pure nitrogen show expected trends according to crystallization theory. Samples annealed in forming gas, however, deviate from this trend. Their crystallinity decreases for increased annealing time. Furthermore, we observe a decrease in the mean nanocrystal size and the size distribution broadens, indicating that hydrogen causes a size reduction of the silicon nanocrystals.

Samenvatting

Directe omzetting van licht in elektriciteit is een van de meest veelbelovende benaderingen voor duurzame energie op grote schaal. Zonnecellen zijn apparaten die het fotovoltaïsch effect gebruiken om zonlicht om te zetten in elektriciteit. Enkele-junction zonnecellen hebben allemaal last van spectrale mismatch, wat de efficiëntie van de cel verlaagd. Fotonen met een lagere energie dan de band gap van het absorber materiaal worden doorgelaten en fotonen met een hogere energie dan de band gap zullen de overtollige energie verliezen als warmte door thermalisatie processen. Een oplossing om overmatige thermalisatie te voorkomen is om meerdere absorber materialen met variërende band gaps te gebruiken. Dit kan worden bereikt met silicium nanokristallen ingebed in een diëlektrische matrix van silicium en de legeringen daarvan met zuurstof, stikstof en koolstof. De andere band gaps nodig voor een efficiënte spectrale match kan worden bewerkstelligd door gebruikmaking van de grootte-afhankelijke kwantumopsluiting in nanoschaal kristallen.

Middels films met afwisselende lagen van stoichiometrische en silicium-rijke siliciumlegeringen is het mogelijk om controle te hebben over de nanokristalgrootte, welke beperkt is tot de silicium-rijke laagdikte. Hoewel er geen duidelijke consensus is omtrent de exacte mechanismen van ladingsdragertransport, wordt de totale lading transport verwacht sterk afhankelijk te zijn van de nanokristalafstand en de keuze van het diëlektrisch materiaal. De nanokristaldichtheid in de silicium-rijke lagen kan worden geregeld door het regelen van de samenstelling van deze lagen tijdens de depositie. Een laag gehalte aan silicium leidt tot relatief weinig geïsoleerde nanokristallen, en het verhogen van het overtollige siliciumgehalte zal uiteindelijk leiden tot clustering van nanokristallen. Wanneer de nanokristaldichtheid te laag is, is de kans op een naaste-buur nanokristal binnen de transport-afstand te laag. Wanneer daarentegen de overmaat silicium te hoog is, zijn nanokristallen zo dicht bij elkaar dat ze beginnen te clusteren, wat kwantumopsluiting in deze kristallen vermindert. Dit betekent dat er een optimale samenstelling is om een beperkte afstand tussen nanokristal te bereiken waarbij clusteren beperkt wordt. In **hoofdstuk 3** tonen we een analytische methode om de stoichiometrie en de dikte van de meerlagige siliciumoxidefilms te optimaliseren om de hoogste dichtheid van silicium nanokristallen na verhitting te bereiken die dicht bij elkaar gelegen zijn maar elkaar niet aanraken. De kans op een nanokristal met een naaste-burenafstand binnen een beperkt bereik worden berekend volgens de stoichiometrie van de gedeponeerde film en de kristalliniteit van de verhitte film als ingangsparameters. Door deze kans te vermenigvuldigen met de waarschijnlijkheid nanokristaldichtheid resulteert in de dichtheid van nanokristallen die elkaar niet aanraken en dicht genoeg bij elkaar liggen.

Beperkt door de nanometerschaal afmetingen van nanokristallen is transmissie-elektronenmicroscopie (TEM) is de enige directe meettechniek geschikt voor het

vastleggen van de grootte en vorm van ingebedde nanokristallen. Echter, een snelle methode om nanokristallen in TEM beelden te meten met minimale input van de gebruiker om vooringenomenheid van de gebruiker tot een minimum te beperken ontbreekt. In **hoofdstuk 4** stellen we een methode voor met minimale vertekening veroorzaakt door de input van de gebruiker om snel de nanokristalgrootteverdeling van transmissie-elektronenmicroscopie beelden te detecteren en te meten van met behulp van een combinatie van Laplacian of Gaussian filters en niet-maximale suppressie. We tonen de voorgestelde methode op bright-field TEM beelden van een a-SiC:H monster met ingebedde silicium nanokristallen met verschillende vergrotingen en vergelijken we de nauwkeurigheid en de snelheid met de grootte distributies verkregen door handmatige metingen, een drempelwaarde methode en PEBBLES. Tot slot overwegen we analytisch de fout veroorzaakt door het snijden van nanokristallen tijdens de voorbereiding van het TEM monster op de gemeten nanokristalgrootteverdeling en formuleren we een vergelijking om te corrigeren voor dit effect.

Zover wij weten is een methode voor het verkrijgen van de absorptie-eigenschappen van de nanokristallen en de toestandsdichtheid uit absorptiespectra nog niet ontwikkeld. In **hoofdstuk 5** presenteren we een niet-destructieve meting en eenvoudige analysemethode voor het verkrijgen van de absorptiecoëfficiënt van silicium nanokristallen ingebed in een amorfe matrix. Deze methode stelt ons in staat om de bijdrage van silicium nanokristallen aan het absorptiespectrum van films met nanokristallen te identificeren. De toestandsdichtheid van de amorfe matrix wordt gemodelleerd met behulp van het standaardmodel voor amorf silicium en de nanokristallen worden gemodelleerd via een Gaussische verdeling van de bezette toestanden en één voor de onbezette toestanden. Voor laserverhitte a-$Si_{0.66}O_{0.34}$:H films toont onze analyse een verlaging van de nanokristal band gap van ongeveer 2.34 tot 2.08 eV, wat een vergroting van de gemiddelde nanokristalgrootte aangeeft voor verhoogde laserfluxdichtheden, gepaard met een versmalling van de nanokristal toestandsdichtheiddistributie van 0.28 tot 0.26 eV, hetgeen een smallere grootteverdeling suggereert.

Ingebedde silicium nanokristallen kunnen worden gemaakt door het verhitten van siliciumrijke films van silicium legeringen. Omdat waterstof effusie optreedt bij lagere temperaturen dan fasescheiding en kristallisatie, kan dit niet worden vermeden, wat leidt tot een verhoogde defectdichtheid. Heropname van waterstof in het materiaal wordt als een doeltreffende methode beschouwd om de defectdichtheid te verminderen. Een optie is om verhitting en waterstofpassivering combineren in een enkele bewerkingsstap door verhitting in een H_2 atmosfeer. In **hoofdstuk 6** melden we het effect van waterstof op het kristallisatieproces van silicium nanokristallen ingebed in een siliciumoxide matrix. We tonen aan dat waterstofgas tijdens verhitting leidt tot een lagere sub-band gap absorptie, wat aangeeft dat passivering van defecten die gecreëerd worden tijdens verhitting optreedt. Monsters die verhit zijn in zuivere stikstof tonen verwachte trends volgens kristallisatietheorie. Monsters verhit in forming gas, echter wijken af van deze trend. Hun kristalliniteit daalt voor langere verhittingstijden. Verder

zien we een toename van de gemiddelde nanokristalgrootte en een verbreding van de grootteverdeling, wat aangeeft dat waterstof een krimp van de silicium nanokristallen veroorzaakt.

Publications

1. H. Ali, L. Xie, **M. van Sebille**, A. Fusi, R. A. C. M. M. van Swaaij, M. Zeman, and K. Leifer, *TEM analysis of multilayered nanostructures formed in the rapid thermal annealed silicon rich silicon oxide film*, European Microscopy Congress 2016: Proceedings, 965–966 (2017).

2. **M. van Sebille**, J. Allebrandi, J. Quik, R. A. C. M. M. van Swaaij, F. D. Tichelaar and M. Zeman, *Optimizing silicon oxide embedded silicon nanocrystal inter-particle distances*, Nanoscale Research Letters **11**, 355 (2016).

3. **M. van Sebille**, A. Fusi, L. Xie, H. Ali, R. A. C. M. M. van Swaaij, K. Leifer, M. Zeman, *Shrinking of silicon nanocrystals embedded in amorphous silicon oxide matrix during rapid thermal annealing in forming gas atmosphere*, Nanotechnology **27**, 365601 (2016)

4. Y. V. Aulin, **M. van Sebille**, M. Moes, F. C. Grozema, *Photochemical upconversion in metal-based octaethyl porphyrin-diphenylanthracene systems*, RSC Advances **5**, 107896–107903 (2015)

5. **M. van Sebille**, L. J. P. van der Maaten, L. Xie, K. Jarolimek, R. Santbergen, R. A. C. M. M. van Swaaij, K. Leifer, M. Zeman, *Nanocrystal size distribution analysis from transmission electron microscopy images*, Nanoscale **7**, 20593–20606 (2015)

6. **M. van Sebille**, R. A. Vasudevan, R. J. Lancee, R. A. C. M. M. van Swaaij, M. Zeman, *Optical characterization and density of states determination of silicon nanocrystals embedded in amorphous silicon based matrix*, Journal of Physics D: Applied Physics **48**, 325302 (2015)

7. D. Deligiannis, S. Alivizatos, A. Ingenito, D. Zhang, **M. van Sebille**, R. A. C. M. M. van Swaaij, M. Zeman, *Wet-chemical Treatment for Improved Surface Passivation of Textured Silicon Heterojunction Solar Cells*, Energy Procedia **55**, 197–202 (2014)

8. P. Babal, H. Lopez, L. Xie, B. van Veen, **M. van Sebille**, H. Tan, M. Zeman, A. H. M. Smets, *Nanostructure Analysis of P-Doped Nanocrystalline Silicon Oxide*, 28th European Photovoltaic Solar Energy Conference and Exhibition 2580–2587 (2013)

Acknowledgments

Doing a PhD project is a challenging undertaking and I could not have done it without the help and support of many people. I would like to start by thanking my daily supervisor dr. René van Swaaij. Thank you for all you support during this project, from weekly discussions to reading and correcting my work. I greatly appreciate your open-door policy and that you always tried to find time to discuss the newest results with me and our MSc students. Also, I would like to thank professor Miro Zeman for giving me the chance to work in the PVMD group.

I would also like to acknowledge the help and support of Mark Workum. You started with this project and after one year decided to pursue a different career, but not before you gave me a very effective crash-course in everything I needed to know about silicon nanocrystals, instructed me on all relevant deposition and characterization setups and introduced me to very useful contacts. You kick started my project and I am deeply grateful. This leads me next to thank Karol Jarolimek. When I started you were half-way in you post-doc on embedded silicon nanocrystals in silicon carbide and we had numerous valuable discussions and worked together on several projects. I learned a lot from you.

I also want to express my gratitude to prof. dr. Laurens Siebbeles from TU Delft, prof. dr. Jaime Gómez Rivas from TU Eindhoven, dr. Elizabeth von Hauff from VU Amsterdam, prof. dr. Klaus Leifer from Uppsala University and prof. dr. Arthur Weeber from TU Delft for reading my thesis, providing feedback and traveling to Delft to be part of my doctoral committee.

Working in the PVMD group as been a lot of fun and I would like to thank all PVMD members, including Fai Tong, Paula Perez Rodriguez, dr. Andrea Ingenito, dr. Ravi Vasudevan, Dimitrios Deligiannis, dr. Hairen Tan, dr. Rudi Santbergen, Robin Vismara, Gianluca Limodio, Nasim Rezaei, dr. Guangtao Yang, dr. Jimmy Melskens, dr. Do Yun Kim, dr. Olindo Isabella, prof. dr. Arthur Weeber, prof. dr. Arno Smets and dr. Klaus Jäger. Klaus was also very nice by allowing me to use his LaTeX template. I would like to give a special thanks to Ravi, Robin, Johan and Fai Tong for the weekly lunchtime discussions about the newest Game of Thrones episode, which provided me with more insight and the deep understanding that the show is diverging from the books.

I also wish to express my deep gratitude for the technicians Martijn Tijssen, Stefaan Heirman and Remko Koornneef, without whom none of the reported experiments would have been possible. Thank you for all your efforts to keep the equipment up and running as much as possible, being so quick to repair broken equipment and being open to adjustments to these sensitive setups.

I would also like to thank Ilona van der Wenden, Sharmila Rattansingh, Ellen Schwenke-Karlas and Laura Bruns for their help with the administrative aspects that are needed when doing a PhD project.

During my PhD project I have also had the honor of supervising MSc students Adele Fusi, Jort Allebrandi and Jim Quik during their thesis projects. This has been a great experience for me and helped me considerably in my project.

Part of the experiments described in this thesis were carried out at Else Kooy laboratory and the Kavli Nanolab and I would also like to thank the technicians Johan van der Cingel, Patricia Kooyman, Hozanna Miro, Charles de Boer and Marc Zuiddam for instructions and help with their equipment. I would also like to thank Tiny Verhoeven from the Eindhoven University of Technology for his assistance with XPS measurements.

I would also like to thank my parents Anna and Thomas for always supporting and believing in me. Erik, Joris, Marieke and Judith, thank you for your help and support.

During the last four years I have done more than only work and one of my favorite activities to unwind at the end of the monthly has been the LVVDMB and game-days, for which I would like to thank Peter de Jong, Lucas van Willenswaard, Steven van Bennekom, Johan Blanker (again), Krijn Wijnands, Bastiaan van Gaalen, Matthijs Betlem, Sander Janssen, Maurice van Loon, Remco Kemperman and Jorrit Hoevenagel.

Last but not least I would like to thank my wife Marieke and my sons Mees and Max for all their love, support and care.

Curriculum Vitae

Martijn van Sebille was born in Ridderkerk, The Netherlands in 1986. He obtained his BSc in Civil Engineering from the Delft University of Technology in 2011. After a transfer minor at the faculty of Mechanical, Maritime and Materials Engineering he started his MSc degree in Sustainable Energy Technology at the faculty of Applied Sciences at the Delft University of Technology. He graduated in 2012 at the department of Chemical Engineering with a thesis on photochemical upconversion of near-IR to visible light for better solar cells.

After receiving his MSc degree he started research on silicon nanocrystals embedded in silicon alloys for more efficient solar energy conversion in the Photovoltaic Materials and Devices group at the faculty of Electrical Engineering, Mathematics and Computer Science at the Delft University of Technology.